



MICRO-SCALE FLAPPING WINGS  
FOR THE  
ADVANCEMENT OF FLYING MEMS

THESIS

Nicholas R. Coleman, Captain, USAF

AFIT/GE/ENG/09-09

DEPARTMENT OF THE AIR FORCE  
AIR UNIVERSITY

***AIR FORCE INSTITUTE OF TECHNOLOGY***

Wright-Patterson Air Force Base, Ohio

APPROVED FOR PUBLIC RELEASE; DISTRIBUTION UNLIMITED.

The views expressed in this thesis are those of the author and do not reflect the official policy or position of the United States Air Force, Department of Defense, or the United States Government.

MICRO-SCALE FLAPPING WINGS  
FOR THE  
ADVANCEMENT OF FLYING MEMS

THESIS

Presented to the Faculty  
Department of Electrical and Computer Engineering  
Graduate School of Engineering and Management  
Air Force Institute of Technology  
Air University  
Air Education and Training Command  
In Partial Fulfillment of the Requirements for the  
Degree of Master of Science in Electrical Engineering

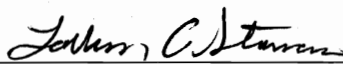
Nicholas R. Coleman, B.S.E.E.  
Captain, USAF

March 2009

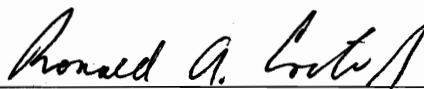
MICRO-SCALE FLAPPING WINGS  
FOR THE  
ADVANCEMENT OF FLYING MEMS

Nicholas R. Coleman, B.S.E.E.  
Captain, USAF

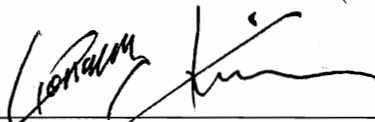
Approved:

  
Maj LaVern A. Starman (Chairman)

9 Mar 09  
date

  
Lt Col Ronald A. Coutu Jr. (Member)

9 Mar 09  
date

  
Dr. Yong C. Kim (Member)

18 FEB 2009  
date

*Abstract*

This research effort presents conceptual micro scale air vehicles whose total dimensions are less than one millimeter. The initial effort was to advance the understanding of micro aerial vehicles at sub-millimeter dimensions by fabricating and testing micro scale flapping wings. Fabrication was accomplished using a surface micromachining process called PolyMUMPs<sup>TM</sup>. Both rigid mechanical structures and biomimetic devices were designed and fabricated as part of this effort. The rigid mechanical structures focused on out of plane deflections with solid connections and assembling a multiple hinge wing structure through the aid of residual stress. These devices were actuated by double hot arm thermal actuators. The biomimetic structures derived from three different insect wings to include; the dragonfly, house fly, and butterfly were selected based off of an attribute that each insect possesses in nature. The dragonfly was chosen for its high maneuverability and hovering capabilities. The house fly wing was chosen because of its durability and the butterfly wing was chosen because of its flexibility. The fabricated wings utilize a thermal bimorph structure consisting of polysilicon and gold which allows device actuation through joule heating. The released micro wings had an initial upward deflection due to residual stress between the gold and polysilicon material layers. Joule heating, from an applied bias, forces the wing to deflect downward due to the coefficient of thermal expansion mismatch between the material layers. Each fabricated bio-wing structure was tested for deflection range as well as operating frequency. From the experimental testing of the micro scale flapping bio-wings, aerodynamic values were calculated to include; aspect ratio, reduced frequency in a hover, Reynolds number of a hovering device, drag force, and gravitational force. The research verified insect based wings on the micro scale are capable of producing the desired flapping motion.

## *Acknowledgements*

First and foremost, I owe a large debt of gratitude to my wife for her support during my time here at AFIT. I want to thank her for often having a warm meal on the table after a long day at school. I thank her for her constant support of my career goals and her sacrifices as I work hard to accomplish the missions of the Air Force. These sacrifices are a constant reminder of her love.

I also want to thank my parents and my mother-in-law. I thank my parents for being my first teachers and the pride they take in my accomplishments of life. I am grateful to my mother-in-law for the bodily nourishment while my mind took a break from the daily rigors of AFIT. I also thank her for allowing my wife and I to store stuff at her house.

Special thanks to my advisor Maj LaVern Starman for his guidance throughout my thesis work. Thanks also to Lt Col Ronald Coutu for advise on experimental improvements along the way. Thanks to both individuals for pushing me to present and publish my work, this will result in multiple publications and several opportunities to brief my research. I would also like to thank my sponsor Mr. Roger Smith from the Air Force Research Laboratory for making this endeavor possible. Thanks also to the many members of the Research Lab that have helped with fabrication processes that cannot be accomplished at the AFIT facilities.

I am especially grateful to Adam, Tod, Luke, Dan, Mo, and James. From solving seemingly impossible homework problems together, to countless hours in the lab, these guys have been great friends and wing men. I would also like to thank these guys and Mimi for their various ideas on improving my thesis work. I'd like to send an extra thank you out to Tod for letting me use his laptop to create movies of my flapping devices as the AFIT computers were ill equipped to handle the task. Thanks everyone for making this a rewarding experience.

Nicholas R. Coleman

## *Table of Contents*

	Page
Abstract . . . . .	iv
Acknowledgements . . . . .	v
Table of Contents . . . . .	vi
List of Figures . . . . .	ix
List of Tables . . . . .	xii
List of Abbreviations . . . . .	xiii
 I. Introduction . . . . .	 1
1.1 Background . . . . .	2
1.2 Objectives . . . . .	2
1.3 Focus . . . . .	2
1.4 Methodology . . . . .	3
1.5 Limitations . . . . .	3
1.6 Organization . . . . .	3
 II. Literature Review . . . . .	 5
2.1 Chapter Overview . . . . .	5
2.2 A Brief History . . . . .	5
2.3 Miniature Mechanical Flyers . . . . .	6
2.3.1 Fixed Wing . . . . .	7
2.3.2 Rotary Wing . . . . .	10
2.3.3 Flapping Wing . . . . .	14
2.4 Flight in Nature . . . . .	19
2.5 Potential Power Sources . . . . .	21
2.5.1 Solar Cells . . . . .	22
2.6 Chapter Summary . . . . .	25
 III. Theory . . . . .	 26
3.1 Chapter Overview . . . . .	26
3.2 Aerodynamics . . . . .	26
3.2.1 Conventional Aerodynamics . . . . .	26
3.2.2 Aerodynamics at Low Reynolds Numbers . . . . .	30
3.3 Actuators . . . . .	33

	Page
3.3.1 Thermal Actuators . . . . .	33
3.3.2 Hybrid Actuator . . . . .	36
3.3.3 Electrostatic Actuator . . . . .	38
3.4 Chapter Summary . . . . .	39
IV. Fabrication and Design . . . . .	41
4.1 Chapter Overview . . . . .	41
4.2 Fabrication . . . . .	41
4.2.1 PolyMUMPs <sup>TM</sup> . . . . .	41
4.2.2 Post Processing . . . . .	43
4.3 Design . . . . .	45
4.3.1 Biology Inspired Designs . . . . .	45
4.3.2 Thermal Actuator Wings . . . . .	48
4.4 Chapter Summary . . . . .	52
V. Modeling and Simulation . . . . .	54
5.1 Chapter Overview . . . . .	54
5.2 CoventorWare® . . . . .	54
5.3 Modeled Designs . . . . .	54
5.4 Run 83 Simulated Results . . . . .	55
5.4.1 Dragonfly . . . . .	56
5.4.2 Fly . . . . .	57
5.4.3 Butterfly . . . . .	60
5.5 Run 84 Simulated Results . . . . .	61
5.5.1 Dragonfly Wings . . . . .	62
5.5.2 Fly Wings . . . . .	65
5.5.3 Butterfly Wings . . . . .	66
5.6 Chapter Summary . . . . .	68
VI. Experimental and Analytical Results . . . . .	69
6.1 Chapter Overview . . . . .	69
6.2 Assembly Wings . . . . .	69
6.3 Connected Wings . . . . .	69
6.4 Bio-Wings . . . . .	70
6.4.1 Dragonfly Experimental Results . . . . .	72
6.4.2 House Fly Experimental Results . . . . .	79
6.4.3 Butterfly Experimental Results . . . . .	82
6.5 Analytical Results . . . . .	88
6.6 Chapter Summary . . . . .	93



	Page
VII. Conclusions . . . . .	94
7.1 Chapter Overview . . . . .	94
7.2 Conclusions . . . . .	94
7.3 Novel Contributions . . . . .	96
7.4 Recommendations for Future Work . . . . .	97
7.5 Chapter Summary . . . . .	98
Appendix A. L-edit Design Layouts . . . . .	99
Appendix B. Process Followers . . . . .	106
B.1 Release . . . . .	106
B.2 Backside Etching . . . . .	107
Appendix C. Analytical Calculations . . . . .	109
C.1 Aspect Ratio . . . . .	109
C.2 Reduced Frequency (Hovering) . . . . .	110
C.3 Reynolds Number (Hovering) . . . . .	112
C.4 Gravitational Force . . . . .	115
C.5 Drag Force . . . . .	117
Bibliography . . . . .	119

## *List of Figures*

Figure		Page
2.1.	Propeller Driven Fixed Wing Mechanical Flyers . . . . .	8
2.2.	Gliding Fixed Wing Mechanical Flyer. . . . .	9
2.3.	Fixed/Flapping Wing Flyer. . . . .	9
2.4.	Picoflyer and Mesicopter . . . . .	11
2.5.	Rotary Magnetic Wings . . . . .	12
2.6.	Glauvitz Rotary Wing Design. . . . .	12
2.7.	Chabak Wing Designs . . . . .	13
2.8.	Terrestrial Entomopter . . . . .	15
2.9.	Microbat Designs . . . . .	16
2.10.	Mechanical Fly . . . . .	16
2.11.	Mircomechanical Flying Insect . . . . .	17
2.12.	Silicon Flying Chip . . . . .	18
2.13.	Power Generation Burner . . . . .	21
2.14.	Simple Solar Cell . . . . .	23
2.15.	4-Junction Solar Cell. . . . .	24
3.1.	Aerodynamic Forces . . . . .	27
3.2.	Airfoil . . . . .	28
3.3.	Reynolds Number vs. Weight . . . . .	29
3.4.	Quasi-Steady vs. Unsteady State . . . . .	31
3.5.	Characteristic Length vs. Reynolds Number . . . . .	32
3.6.	Actuators: Force vs. Displacement . . . . .	34
3.7.	Actuators: Frequency vs. Displacement . . . . .	35
3.8.	Thermal Actuators . . . . .	36
3.9.	Bent Beam Actuator . . . . .	36
3.10.	Thermal Bimorph . . . . .	38

Figure		Page
3.11.	Comb Drive . . . . .	40
4.1.	PolyMUMPs <sup>TM</sup> Layers . . . . .	43
4.2.	DRIE Patterned Chip . . . . .	44
4.3.	Dragonfly Wing Design . . . . .	46
4.4.	House Fly Wing Design . . . . .	47
4.5.	Butterfly Design . . . . .	48
4.6.	Actuation Schemes . . . . .	49
4.7.	Assembly Wings . . . . .	51
4.8.	Assembly Aids . . . . .	52
4.9.	Connected Wings . . . . .	53
5.1.	Modeled Dragonfly Forewing . . . . .	55
5.2.	Leading and Trailing Edge Dragonfly Simulation . . . . .	56
5.3.	Center Actuated Dragonfly Designs and Simulations . . . . .	58
5.4.	Fly Simulations and Wing Design . . . . .	59
5.5.	Butterfly Simulations and Wing Design . . . . .	61
5.6.	Extended Current Path Dragonfly Wing Actuation Schemes . .	63
5.7.	Extended Current Path Dragonfly Wing Simulations . . . . .	63
5.8.	Dragonfly Wing Simulations on Full Vein Wings . . . . .	64
5.9.	Extended Current Path Fly Simulations . . . . .	66
5.10.	Extended Current Path Butterfly Simulation . . . . .	67
6.1.	Assembly Wing Key Components . . . . .	70
6.2.	Experimental Connected Wings . . . . .	71
6.3.	Ground Line Failure . . . . .	72
6.4.	Experimental and Conceptual Wing Deflection . . . . .	73
6.5.	Large Dragonfly Forewing with Entire Vein Structure . . . . .	75
6.6.	Pre and Post Bias Effect on Wing Structures . . . . .	77
6.7.	Test Measurements on Butterfly Wings . . . . .	83
6.8.	Deflection Measurement of Large Butterfly Wing . . . . .	84

Figure		Page
6.9.	Butterfly Wing in Contact with Substrate . . . . .	85
6.10.	Wire Bonded Test Device . . . . .	87
A.1.	MUMPs® run 82 . . . . .	99
A.2.	MUMPs® run 83 . . . . .	101
A.3.	MUMPs® run 84 . . . . .	102
A.4.	Back Side Mask for Run 83 . . . . .	104
A.5.	Back Side Mask for Run 84 . . . . .	105

## *List of Tables*

Table		Page
2.1.	Summary of mechanical fixed wing devices. . . . .	10
2.2.	Summary of rotary wing devices. . . . .	14
2.3.	Summary of flapping wing devices. . . . .	18
3.1.	Actuator Comparison Table . . . . .	36
3.2.	Bimorph Material Properties . . . . .	37
3.3.	Thermal Actuator Comparison Table . . . . .	38
5.1.	Comparison of Simulated Dragonfly Wings . . . . .	65
5.2.	Comparison of Simulated Fly Wings . . . . .	67
5.3.	Comparison of Simulated Butterfly Wings . . . . .	68
6.1.	Summary of the Dragonfly Experimental Results . . . . .	79
6.2.	Summary of the House Fly Experimental Results . . . . .	82
6.3.	Deflection Measurements on the Two Butterfly Wing Halves . .	86
6.4.	Summary of the Butterfly Experimental Results . . . . .	87
6.5.	Analytical Results for MUMPs <sup>®</sup> run 83 . . . . .	89
6.6.	Analytical Results for MUMPs <sup>®</sup> run 84 . . . . .	90
6.7.	Weight and Drag Force Values . . . . .	91
6.8.	Require Frequency for Lift Off . . . . .	92
A.1.	MUMPs <sup>®</sup> run 82 . . . . .	100
A.2.	MUMPs <sup>®</sup> run 83 . . . . .	100
A.3.	MUMPs <sup>®</sup> run 84 . . . . .	103
B.1.	Release Process Follower with CO <sub>2</sub> Dryer . . . . .	106
B.2.	Release Process Follower for Hot Plate Release . . . . .	107
B.3.	Backside Alignment Process Follower . . . . .	108
C.1.	Wing and Actuator Line Weight Values . . . . .	116

## *List of Abbreviations*

Abbreviation		Page
UAVs	Unmanned Aerial Vehicles . . . . .	1
MEMS	Micro-Electro Mechanical Systems . . . . .	1
NEMS	Nano-Electro Mechanical Systems . . . . .	1
AFIT	Air Force Institute of Technology . . . . .	2
PolyMUMPs	Polysilicon Multi-User MEMS Processes . . . . .	3
DARPA	Defense Advanced Research Projects Agency . . . . .	5
MAV	Micro-Aerial Vehicle . . . . .	5
NAV	Nano-Aerial Vehicle . . . . .	5
SBIR	Small Business Innovation Research . . . . .	6
PCB	Programmable Control Board . . . . .	8
RCM	Reciprocating Chemical Muscle . . . . .	14
MFI	Micromechanical Flying Insect . . . . .	16
MFC	Micro Flying Chip . . . . .	17
TCE	Thermal Coefficient of Expansion . . . . .	17
LEV	Leading Edge Vortex . . . . .	19
MJSC	Multi-Junction Solar Cell . . . . .	22
LPCVD	Low Pressure Chemical Vapor Deposition . . . . .	41
RIE	Reactive Ion Etching . . . . .	41
PSG	Phosphosilicate Glass . . . . .	41
HF	Hydrofluoric Acid . . . . .	42
DRIE	Deep Reactive Ion Etching . . . . .	43
PECVD	Plasma Enhanced Chemical Vapor Deposition . . . . .	43
SEM	Scanning Electron Microscope . . . . .	50
AC	Alternating Current . . . . .	51
DC	Direct Current . . . . .	69

Abbreviation		Page
IFM	Interferometer Microscope . . . . .	70
DCASS	Dayton-Cincinnati Aerospace Sciences Symposium . . . .	97
AIAA	American Institute of Aeronautics and Astronautics . . . .	97

# MICRO-SCALE FLAPPING WINGS

## FOR THE

## ADVANCEMENT OF FLYING MEMS

### **I. Introduction**

There are currently many different kinds of unmanned aerial vehicles (UAVs). They range in size from approximately a third of a football field down to devices that fit comfortably into the palm of a hand. These UAVs are enjoyed by hobbyist, played with by children, and used by the military for a multitude of functions. The military has a particular interest in miniature flying devices which could serve a role in surveillance and reconnaissance.

Imagine the ability to do reconnaissance inside of buildings and other restricted spaces using a device that is less than one millimeter in size. Realization of a device at this level would allow infiltration of denied or extremely dangerous areas with minimal risk to humans. Likewise, a device this small would be nearly undetectable to the enemy. It is a daunting feat in terms of engineering challenges but success would produce great capability.

Optimally, the device can operate indoors and outdoors 24 hours a day. The ability to achieve this level of robustness introduces power and range limitations. Another engineering concern for such small devices is how to control the device.

Micro-electro mechanical systems (MEMS) technology makes it possible to create micrometer sized features and sub-millimeter sized devices. MEMS devices are common place in many device applications such as air bags and projection televisions. Advancements in the semiconductor industry have allowed these device features to go down to tens of nanometers in size or nano-electro mechanical systems (NEMS).

Unfortunately, even these advancements have not been enough for a sub-millimeter device to sustain flight in a controlled environment let alone under austere atmospheric



conditions. Although no flying devices have been created at this scale yet, many flying devices smaller than a hand have shown success. Combining these successes with empirical and theoretical results for sub-centimeter flying designs are all valuable tools in the realization of a flying MEMS device.

### **1.1 Background**

The goal to develop MEMS flying robots has been ongoing at the Air Force Institute of Technology (AFIT) since 2005 under the funding support of the Air Force Research Laboratory's Munitions Directorate. Daniel Denninghoff, the first to approach this challenge, focused on flapping structures through laser activation. Nathan Glauvitz focused his designs toward rotary wing applications. Kelson Chabak followed up on Glauvitz's work to advance the understanding and improvement of rotary wing designs. Each of these individuals successfully fabricated designs that illustrated proof of concept for a flying MEMS device. However, none of the devices were capable of flight.

### **1.2 Objectives**

MEMS flying devices are still a largely unexplored area of research. Therefore, designs are limited mainly by the creativity of the engineer. The objectives of this research are:

- Design and fabricate MEMS flapping devices of mechanical and biologically inspired by nature
- Model and simulate flapping MEMS devices to be fabricated and tested
- Experimentally demonstrate the capability of fabricated flapping MEMS wings under an external power source

### **1.3 Focus**

The focus of this research is to develop flapping wings capable of generating lift. The motivation for flapping wings comes from the successful demonstration

of flapping motion in Denninghoff's MEMS designs and nature's multitude of tiny insects achieving successful flight every day. Building on successful elements of past MEMS fabrication and introducing additional design improvements allows for the advancement of flapping wing designs in this thesis.

#### **1.4 Methodology**

The finite element modeling tool, CoventorWare®, will be used to model and simulate wing designs prior to fabrication in order to improve upon the designs. Designs will be laid out using the computer aided design software L-edit and fabricated using Polysilicon Multi-User MEMS Processes (PolyMUMPs). Post processing will occur on some of the fabricated designs using standard MEMS fabrication techniques. This will eliminate some limitations of the fabricated devices. Fabricated designs will be tested under externally applied power and compared against the simulated results while also demonstrating the actuation scheme.

#### **1.5 Limitations**

The PolyMUMPs<sup>TM</sup> process used by AFIT for fabrication is limited by design rules and the number of layers which ultimately limits the types of designs possible. The MUMPs® process also takes several months for fabrication. Therefore, only three fabrication runs are feasible after the submission of the first fabrication run due to the 18 month graduate program time constraints. The experimental results were restricted to a tethered device rather than an autonomous device due to power and control issues that accompany wireless devices.

#### **1.6 Organization**

This thesis is organized chronologically from this point forward. Chapter two focuses on flying robots that already exist and lessons learned from flying insects. In chapter three, the theory behind flying devices are discussed. Chapter four canvasses design and fabrication. Modeling and analysis of the flapping wing devices are covered

in chapter five. Chapter six entails the experimental and analytical results of the devices. The last chapter provides conclusions with recommendations for future work in the micro flying arena.

## II. Literature Review

### 2.1 Chapter Overview

The purpose of this chapter is to provide an overview of flyers which will help in the development of a MEMS flyer. Since there are hardly any current flyers smaller than one millimeter, a MEMS scale device, the review will look at flyers up to the Defense Advanced Research Projects Agency's (DARPA) defined Micro-Aerial Vehicle (MAV). DARPA defines the MAV as having a maximum wing span of 15 cm and weighing up to 100 grams [1]. DARPA also has a Nano-Aerial Vehicle (NAV) classification which includes devices with a wing span of 7.5 cm or smaller weighing 10 grams or less [2]. Two main categories of flyers are reviewed in this chapter: mechanical, which consist of rotary, fixed wing, and flapping devices and natural, which focuses primarily on insects. This chapter concludes with potential ways to power a MEMS scale flying device.

### 2.2 A Brief History

The beginning of the microelectronics field arguably started with the development of the first transistor back in 1947. Then in 1959, Nobel Prize winner Richard Feynman would challenge the world to develop microsystems ranging from biological systems to computer data storage [3]. Over the next 20 years, some developments would be made in the microelectronics field which would advance the field toward micro scale systems. However, in the early 1980's, an extensive review of silicon as a viable material for miniature mechanical devices was undertaken. The results of that review showed that silicon possessed excellent mechanical properties, could be used in batch fabrication, and was inexpensive compared to alternatives [4]. This breakthrough would lead to significant advances in microelectronics in the following years.

In the 1980's, microsystems technology had taking off. Advancements in radiant, mechanical, thermal, magnetic, and chemical silicon sensors was in full swing by the late 1980's [5]. With the advancement of silicon sensors, micro robotics was also

advancing. Then, in 1987, a workshop called IEEE Micro Robots and Teleoperators Workshop met. As a result of this meeting, a report of the *Workshop on Microelectromechanical Systems Research* was published [6]. This landmarks the beginning of regular workshop meetings and the emergence of MEMS into its own distinct engineering field.

The late 1980's and early 1990's saw a significant increase in MEMS research. With the advancement of photolithography, MEMS devices such as the comb drive, cantilever beam, micro mirror, and thermal actuator were realized as building blocks for other systems. In 1992, Suzuki *et al* produced the first 3-D robotic structure using paper folding techniques and MEMS fabrication [7]. This breakthrough inspired other research in biomimetics. Two years later, Fukuda *et al* designed a swimming robot [8]. The required motion for swimming is very similar to that of a flapping device and later that same year a flying MEMS design made its debut [9]. Now that a flying design had been created, DARPA recognized the need to further pursue this technology. After a feasibility study was performed by the RAND Corporation in 1993, DARPA setup a MAV workshop in 1995. This workshop culminated in 1996 with MAV research funds in a Small Business Innovation Research (SBIR) program [10].

At this point in time, it is important to distinguish between the “micro” aerial vehicle discussed so far and what it means to truly be a micro aerial vehicle. To truly be a micro vehicle, the largest dimension must not exceed one millimeter. Therefore, to distinguish between the two classifications of vehicles, any vehicle that has dimensions greater than one millimeter will be refereed to as a miniature vehicle and those with maximum dimensions less than a millimeter will be micro vehicles.

### ***2.3 Miniature Mechanical Flyers***

The miniature flyers of interest for this paper range from approximately 15 cm down to less than a single centimeter. Within that range, flight methods vary between fixed, rotary, and flapping wing for mechanical structures. For natural flyers,

flight methods include flapping wing and the combination of fixed/flapping. The next sections will take a closer look at some of these flyers.

*2.3.1 Fixed Wing.* Fixed wing aircraft generate lift by forward motion through air. This can generally be accomplished either by a propeller system or a propulsion system such as an engine. Gliders are also fixed wing aircraft but require some form of launch (often towed behind an aircraft and then released at a desirable altitude) to get them started. The next few paragraphs look at some of the MAV devices that fit into the fixed wing category.

One of the first successful miniature fixed wing mechanical flyers was the Black Widow shown in Figure 2.1 (a) which first debuted in August of 2000. The body of the airframe is constructed of expanded polystyrene foam coated with fiberglass and the rudder is balsa wood hinged with Kevlar<sup>®</sup> cloth. The Black Widow is 15.2 cm in diameter and is driven by a motorized propeller and controlled by two onboard microprocessors. Also, onboard is a color video camera with direct down link capability. This device is a fully autonomous flyer powered by a lithium battery that provides 30 minutes of flight time. It weighs 80 grams and can fly 1.8 kilometers at speeds up to 35 mph [10, 11].

Another fixed but flexible winged flying structure shown in Figure 2.1 (b) comes from the University of Florida. This device is constructed of carbon fiber chords, cloth pre-impregnated with epoxy resin, and latex rubber sheets. It has a span of 12.7 cm. Like the Black Widow, this membrane wing based MAV is also driven by a motorized propeller. A surveillance and reconnaissance camera is also one of the main features of this design. This flyer is also powered by a lithium battery but it only gets a flight time of approximating 15 minutes. The flexible flyer weighs a total of 52 grams and is capable of flying at 25 mph [12, 13].

Robert Wood *et al* developed a different type of fixed wing MAV. Unlike the Black Widow and the flexible flyer, the MicroGlider is not propelled but rather relies on its ability to glide. It is constructed of ultra high modulus composite materials.

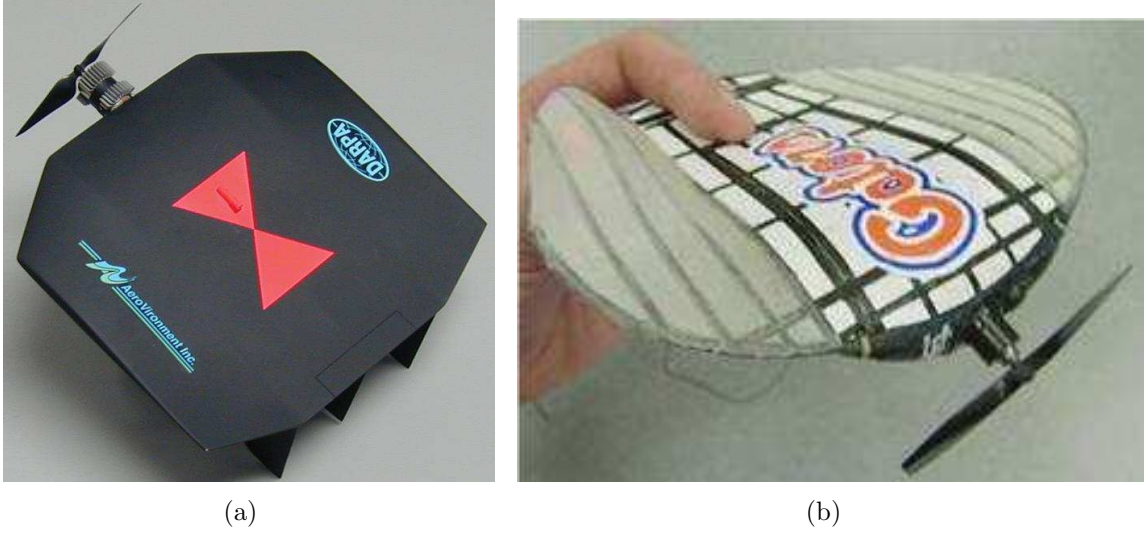


Figure 2.1: (a) The Black Widow which is capable of 30 minutes of continuous flight [10, 11]. (b) The fixed wing flyer from the University of Florida. Its wing structure is flexible which helps to minimize effects of wind on the structure [12].

The MicroGlider, shown in Figure 2.2, weighing only 2.2 grams has a wing span of 10 centimeters and is controlled by actuators on the tail. A lithium polymer battery provides enough power for 10 minute flight durations. The flyer is equipped with an imagery Programmable Control Board (PCB) which allows flight toward an illuminated target [14].

One device that fits both the fixed and flapping wing category is the bio-morphic flyer shown in Figure 2.3. The biplane wing design, which is the flapping wings portion of the design, is driven by a crankshaft and electric motor. These two components are contained by the fixed wing portion of the device. Both the fixed and flapping wings were constructed of laminate materials yielding a 15 cm wing span. Testing the 7 gram device in a wind tunnel showed that it achieves lift between 4-7 mph at a flapping frequency of approximately 40 Hz [15].

Each of the fixed wing devices reviewed were able to achieve lift. Only the bio-morphic flyer did not achieve untethered flight. Each of the devices had their own unique capabilities also. A summary of the mechanical fixed wing MAV devices is provided in Table 2.1. The next section focuses on mechanical rotary devices.

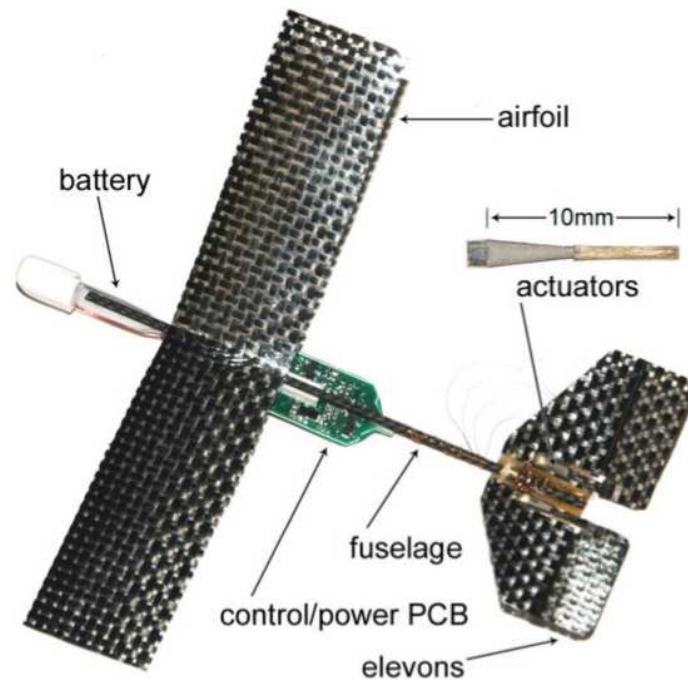


Figure 2.2: The MicroGlider is equipped for autonomous flight in the direction of an illuminated light source [14].

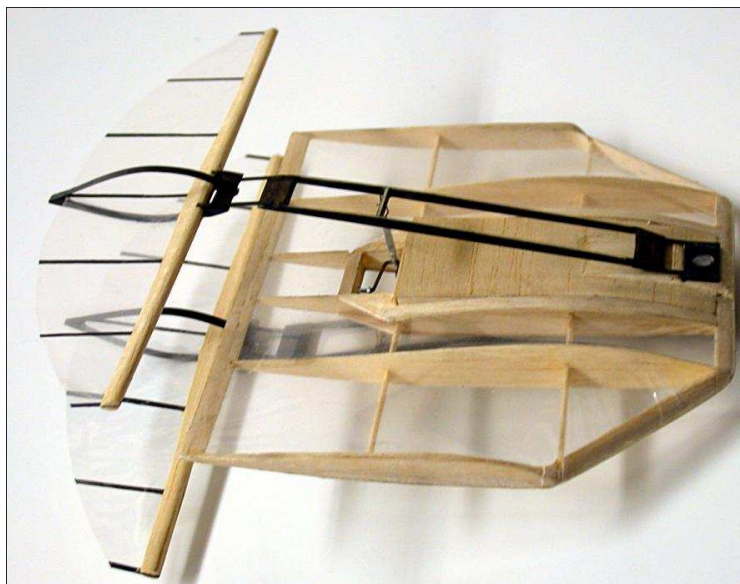


Figure 2.3: The bio-morphic flyer takes advantage of both fixed and flapping wing flight. It is able to achieve lift at 4-7 mph but adding a battery made it too heavy to achieve untethered flight [15].



Table 2.1: This table summarizes the different characteristics of the mechanical fixed wing devices reviewed in this paper.

Fixed Wing Devices							
Device	Wing Span	Materials	Speed	Weight	Flight Time	Other	Flys
Black Widow	15.2 cm	polystyrene foam, fiberglass, balsa-wood, Kevlar <sup>®</sup>	35 mph	80 g	30 mins	battery power, color video camera	Yes
Flex Wing	12.7 cm	carbon fiber, resin cloth, rubber sheets	25 mph	52 g	15 mins	battery power, color video camera	Yes
MicroGlider	10 cm	composite materials	?	2.2 g	10 mins	battery power, imagery PCB	Yes
bio-morphic	15 cm	laminate, wood	4-7 mph	7 g	0 sec	tethered, lift off	No

*2.3.2 Rotary Wing.* Rotary wing aircraft generate lift by revolving the wings, called rotors, around a mast. Since the lift force is the rotors and not forward motion, rotary aircraft have the ability to hover. This provides for a capability unavailable to the fixed wing aircraft discussed previously. Some examples of rotary MAVs are discussed in the following paragraphs.

The Picoflyer had its first successful flight on 7 August 2005. It is constructed of carbon, Aramid fabric, foam tape, brass bearings, and plastic gears. It has two contra rotating, four bladed rotors that are 6 centimeters in diameter. The Picoflyer is battery powered and has a flight time of one minute. The Picoflyer weighs 3.3 grams and is shown in Figure 2.4 (a) [16].

Another rotary wing device is the Mesicopter shown in Figure 2.4 (b). The Mesicopter rotors are constructed of polymer materials. The total width of the design is approximately 4 cm with each of the 4 rotors having a 1.5 cm diameter. The design was developed to run under battery power estimated to provide 14 minutes of flight

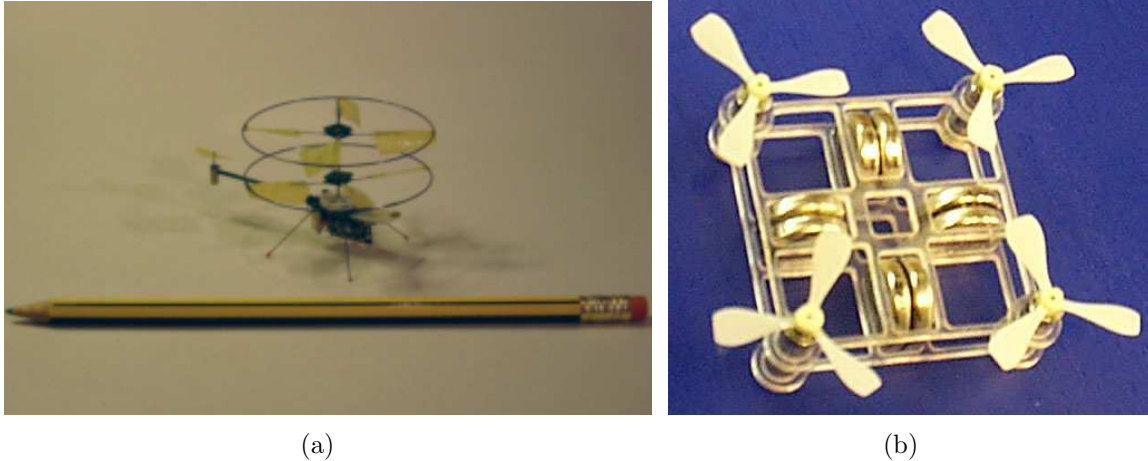


Figure 2.4: (a) This is the Picoflyer, the smallest radio controlled helicopter ever presented (2005) [16]. (b) The Mesicopter is a four rotor device designed to fly on battery power. It has a total diameter of approximately four centimeters [17].

time and an estimated maximum flight speed of 3.4 mph. The design also plans to include an optical camera. The Mesicopter was tested under tethered power source and was capable of lift but hasn't been flown under battery power [17].

The ability to hover was realized by a device with soft magnetic rotational wings as shown in Figure 2.5. The single continuous blade with flaps was constructed of silicon dioxide, chromium, and nickel forming two wings. Each  $900\text{ }\mu\text{m}$  long wing was then electroplated with a nickel-iron alloy to give it magnetic properties. The total size of the device measures approximately 8 mm. This flying device requires an alternating magnetic field as opposed to a battery to power its flight. It was able to achieve 8 seconds of flight up a set of guides wires. However, this design does limit the device to a controlled magnetic field. Without the added weight of a battery, the device only weighed 3.5 milligrams [18–23].

A rotary design on the millimeter scale was the goal of Nathan Glauvitz from AFIT. Nathan's PolyMUMPs<sup>TM</sup> fabricated design is shown in Figure 2.6. Each wing had a  $900\text{ }\mu\text{m}$  wingspan and the device consisted of six wings. A scratch drive actuation method was used to rotate the wings. This method was capable of rotating

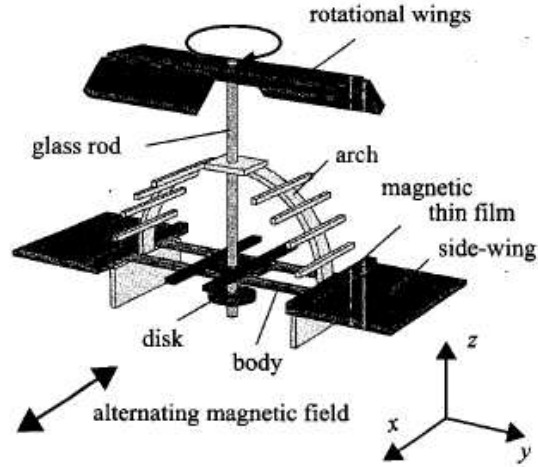


Figure 2.5: This is a schematic of the magnetic flyer's construction. This flight mechanism has flown up two established guides in an 8 second flight at 540 Hz [20].

the drive at 3 revolutions per minute. However, once the wings were attached to the drive it was not capable of moving the additional weight [24].

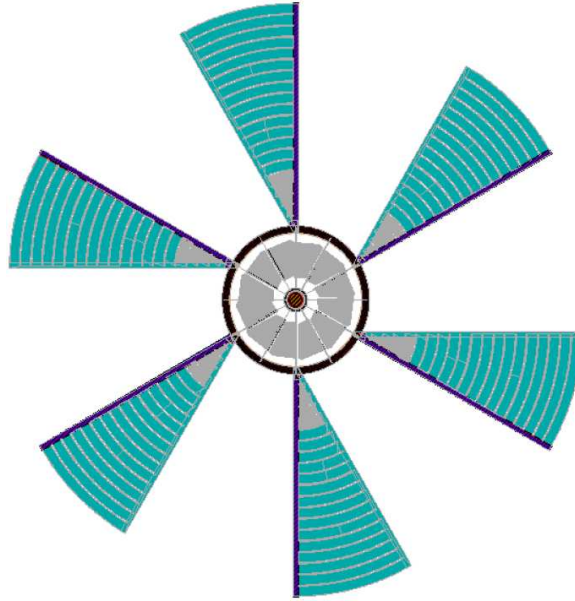


Figure 2.6: The driving force of this rotary wing design by Nathan Glauvitz is the scratch drive [24].

Kelson Chabak from AFIT also worked on a rotary wing device using PolyMUMPs<sup>TM</sup>. Kelson's designs modified Glauvitz's suggested wing designs and Tsuzuki already fab-

ricated wings. The modified Glauvitz wing design, named wing-G, was constructed of poly1, poly2, and gold and measured 1270 by 540  $\mu\text{m}$ . The wing-G system consisted of four rotors with four wings on each rotor. The wing-T, named for the modified Tsuzuki design, measured 1250 by 250  $\mu\text{m}$  and was also constructed of poly1, poly2, and gold. Each rotor consisted of 5 wings in this scheme. Both design schemes attached to a main gear driven by comb resonators and thermal actuators. The wing designs did rotate, but were hindered by the conformal nature of the PolyMUMPs<sup>TM</sup> process. This nature prohibited the device from achieving rotational speeds required to generate lift [25]. Figure 2.7 (a) and (b) show the wing-G and wing-T design layouts respectively.

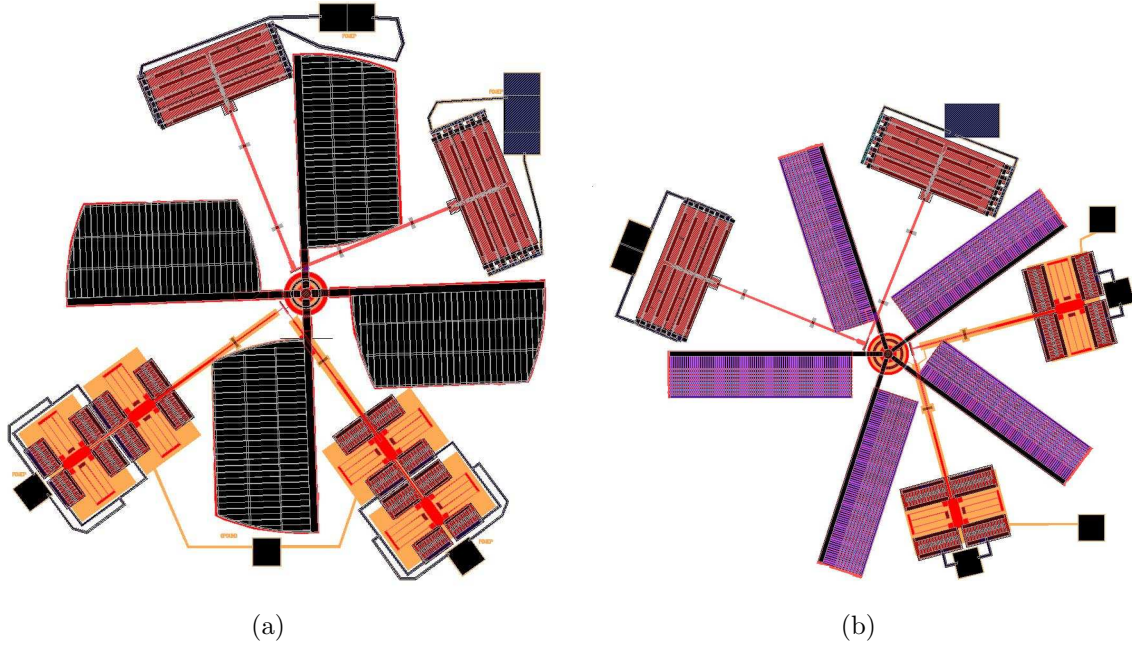


Figure 2.7: (a) The wing-G design is an improved version of the wing design by Glauvitz. (b) The wing-T design is an improved version of the Tsuzuki design [25].

Five different rotary devices were reviewed in this section. Some of these devices are capable of flight while others advanced the understanding of what is required to fly at the millimeter scale. A summary of the rotary wing devices reviewed is provided in Table 2.2. The next section focuses on biomimetic wing devices.

Table 2.2: This table summarizes the different characteristics of the mechanical rotary wing devices reviewed in this paper.

Rotary Wing Devices							
Device	Wing Span	Materials	Speed	Weight	Flight Time	Other	Flys
Picoflyer	6 cm	carbon, Aramid fabric, plastic	?	3.3 g	1 min	battery power	Yes
Mesicopter	4 cm	polymer materials	3.4 mph	?	14 mins	battery power, optical camera	Yes, tethered
Magnetic Wings	8 mm	SiO <sub>2</sub> , Cr, Ni	?	3.5 mg	8 sec	magnetic field	Yes, guided
Glauvitz Design	2.5 mm	PolyMUMPs <sup>TM</sup>	?	?	0 sec	tethered	No
Chabak Design	3 mm	PolyMUMPs <sup>TM</sup>	?	?	0 sec	tethered	No

*2.3.3 Flapping Wing.* Flapping wing devices fly by generating lift through oscillation or flapping of wings. These devices are often called entomopters, winged insect machines, or ornithopter, winged bird machines. The flapping wing benefits from both fixed and rotary wing domains by providing gliding and hovering capabilities. Several examples of flapping wing MAVs are discussed in the following paragraphs.

The first flapping wing device reviewed was the Terrestrial Entomopter shown in Figure 2.8. The Entomopter is constructed of the Reciprocating Chemical Muscle (RCM) actuator and stereolithographic wings. It has a wingspan of 15 cm, weighs 50 grams, and operates between 25-30 Hz. Flight control is achieved through the actuation of the x-wing design of the system. The RCM is powered by “various chemical fuels” and provides between 5 to 10 minutes of flight before refueling is required [26–28].

An ornithopter from Tamkang University was reviewed. It was constructed using titanium alloy, hollow stainless steel tubes, and acrylics. It had a wing span of 14 cm and can withstand wind speeds up to 17 mph. The total weight of the flapping

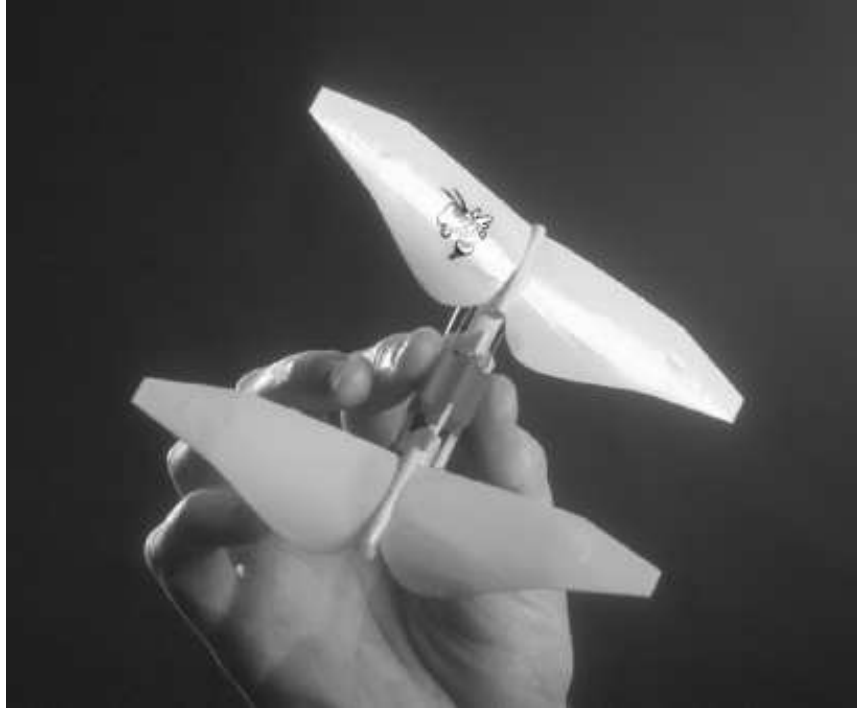
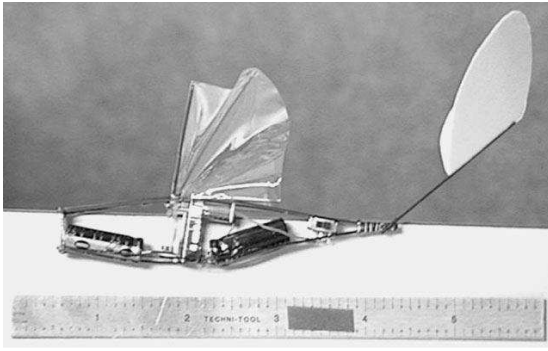


Figure 2.8: A flapping wing design by Michelson *et al* that is powered by fuel and controlled by flapping the wings in an alternating or x-wing configuration [26].

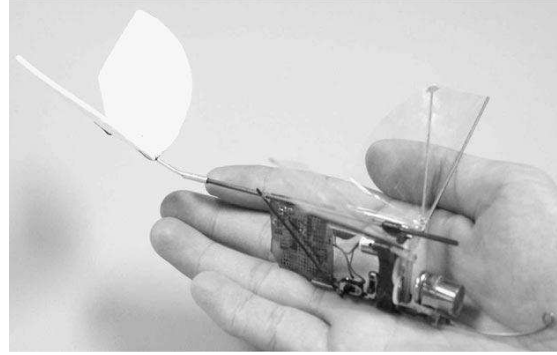
design with lithium batteries on board is 22 grams. Its design allows it to both flap and glide which was demonstrated in wind tunnel experiments [1].

Another flapping wing MAV is the Microbat. The structure is made of titanium alloy and parylene-C with a total span of 14 cm. The Microbat has two design forms, one powered by super capacitors and the other by rechargeable NiCd batteries. These designs weighed 6.5 grams and 10.5 grams, respectively. These power schemes allowed the device to fly for 9 and 18 seconds, respectively [29,30]. Figure 2.9 (a) shows the super capacitor design and Figure 2.9 (b) shows the battery powered design.

The tiny fly by Robert Wood *et al* shown in Figure 2.10 was another insect like mechanical device. The fly was built using carbon-fiber and thin film laminates. It has a wing span of 3 cm and weighs a total of only 60 milligrams. It currently is capable of flying under tethered power supply. Future plans include adding sensors, controls,



(a)



(b)

Figure 2.9: (a) The super capacitor design for the Microbat. (b) The battery powered design for the Microbat [29].

and battery power for controllable, untethered flight capabilities. Adding current battery technology to the device, gives an estimated 5-10 minute flight time [31].

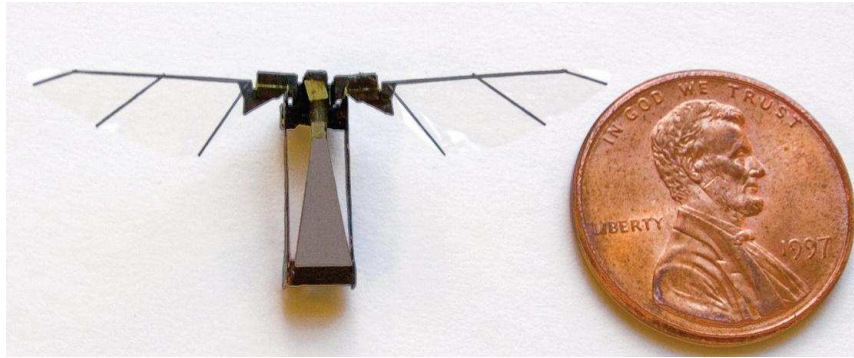
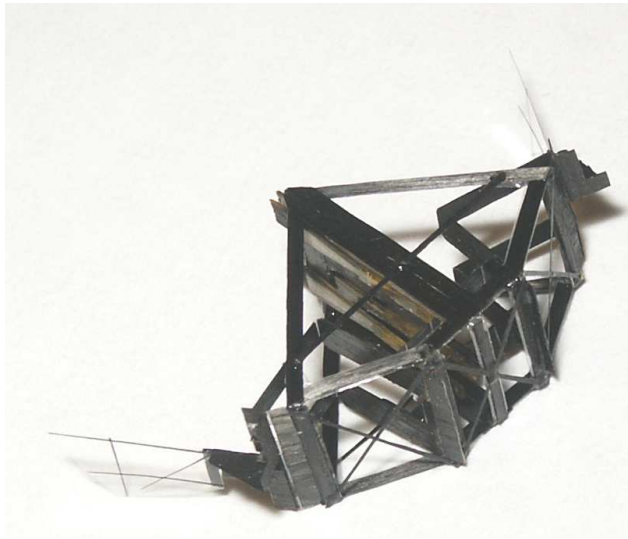


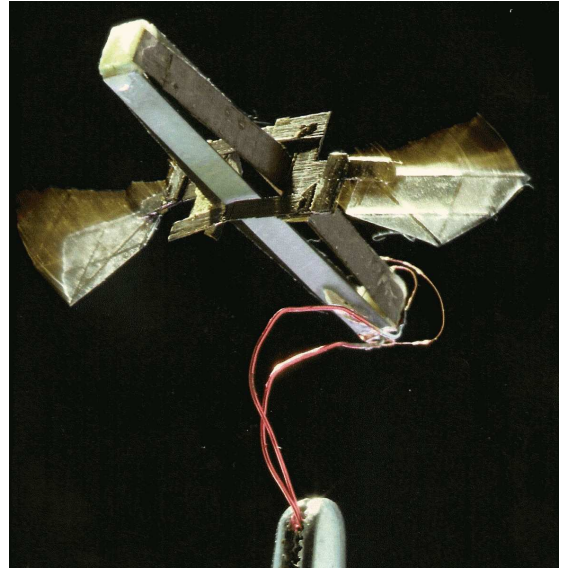
Figure 2.10: The mechanical fly shown here achieves flight using the same motions as the actual insect [31].

The Micromechanical Flying Insect (MFI) from Berkeley is another insect inspired design. Figure 2.11 (a) shows an image of the MFI in its earlier stages of design and Figure 2.11 (b) shows the design as of April 2008. It is constructed of a carbon fiber frame and laminate wings. Its wings are 10 mm each with the total span of the device measuring 2.5 cm. The wings are actuated by piezoelectric and the total weight of the device is 100 milligrams. The force generated by the wings, which flap 275 times per second, is capable of providing lift for the flapping wing device [32,33].





(a)



(b)

Figure 2.11: (a) This MFI (2003) is part of a continuous effort to develop a mechanical flying insect. The technology is progressing toward autonomous flight [32] (b) The 2008 version of the MFI in a tethered hover [33].

A micro flying chip (MFC) is another flapping device shown in Figure 2.12. This design draws its inspiration from the aphid, a soft bodied, pearl shaped insect. Five, 1 mm wings made of parylene C create the MFC which has a total wing span of less than three millimeters. The wings are thermally actuated causing them to curl up and cooling caused them to flatten back out. The ability to actuate this scheme up to 200 Hz was shown by Chan *et al*, which slightly exceeded the goal of 60-177 Hz (frequency of flapping in aphids) [34].

Former AFIT student, Daniel Denninghoff developed a series of laser actuated flapping wing schemes. These devices, constructed of the poly2 and gold layers from the PolyMUMPs<sup>TM</sup> process, range from 500 to 990  $\mu\text{m}$  in total wing span. A center target in the wing structure was heated with a 660 nm laser resulting in a downward deflection of the wings [35]. The wings initially deflected up because gold has a higher thermal coefficient of expansion (TCE) than poly2 creating residual stress in the released structures. Heating the device with the laser causes the wings to flatten



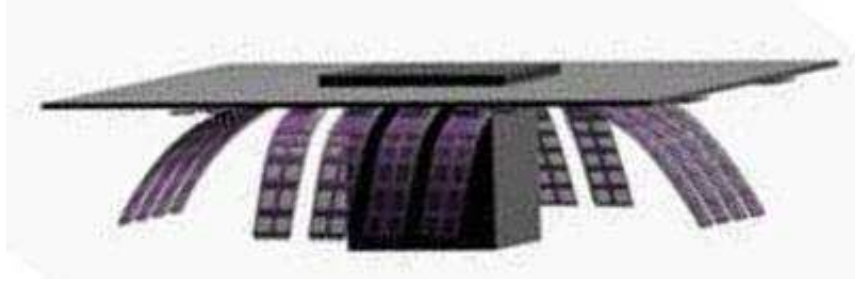


Figure 2.12: The MFC shows that the thermally actuated “wings” will “flap” in the frequency range of aphids. This graphic shows its conceptual flight capability [34].

back down. Though this scheme caused deflection in the wings, the wings didn’t flap fast enough to create lift. Table 2.3 provides a summary of the flapping wing designs.

Table 2.3: This table summarizes the flapping wing device’s characteristics. Note, the final table entry is a micro device rather than a miniature device.

Flapping Wing Devices							
Device	Wing Span	Materials	Speed	Weight	Flight Time	Other	Flys
Ento-mopter	15 cm	RCM, stereolithographic wings	?	50 g	5-10 min	fuel powered	Yes
Orni-thopter	14 cm	titanium, steel, acrylics	?	22 g	?	battery powered	Yes, wind tunnel
Microbat	14 cm	titanium alloy, parylene-C	?	6.5 g 10.5 g	9 sec 18 sec	super capacitor battery powered	Yes
Fly	3 cm	carbon fiber, film laminates	19 mph	60 mg	5-10 min	tethered	Yes, guided
MFI	2.5 cm	carbon fiber, laminate	?	100 mg	?	piezo-electric	Yes, lift off
MFC	3 mm	parylene-C	?	1 mg	?	tethered	No, flaps
Denninghoff	500-900 $\mu\text{m}$	PolyMUMPs <sup>TM</sup>	?	?	0 sec	micro device	No, flaps

## 2.4 *Flight in Nature*

How birds and insects fly has been a scientific marvel for many years. Their ability to maneuver and change directions quickly would cause traditional forms of aircraft to break apart. Though many have marveled at the abilities of this flight, the knowledge of flight by these small creatures is still not fully understood. This section looks at what is required for insects to fly and reviews various insect flight to provide a better understanding of how a micro mechanical device may perform in a similar regime.

Like any aircraft, for an insect to fly it must possess three things: lift, thrust, and control. Thrust in an aircraft is provided by an engine but in an insect it comes from asynchronous muscle structure. In general, lift is created by wings translating air downward causing upward force in the wing structures. In an aircraft, the air flow is created by the speed of the aircraft moving through the air but insects create the flow of air from their own flapping. It is therefore possible for insects to fly because inertial forces dominate viscous effects for lower ranges of Reynolds numbers (insects: 10-10,000). The Reynolds number is the ratio of inertial resistance to viscous resistance for flowing fluids. So, a leading edge vortex (LEV) is created from the flapping motion of insects to generate lift opposed to straight airflow. LEV is a fluid rotation at or near the surface of the wing. A more in-depth discussion of LEV is described in [36,37]. The final element required is control. A pilot/computer network provide this control on traditional aircraft and an insect uses its brain and other bodily sensors to control flight [36]. This addresses the basic requirements for flying while the following paragraphs will look at how some insects approach flight differently.

Dragonflies are one of the insects reviewed since they have the ability to hover and fly in almost any direction through individual control of their four wings. The frequency, amplitude, and angle of attack are all controlled parameters of the dragonfly flight while plunging or pitching its wings. A dragonfly flaps its wings up and down while many insects flap back and forth. The frequency of flapping in different

dragonfly species is in the range of 30-50 Hz. These wings operate at a Reynolds number of approximately 4300 [37].

House flies have the ability to fly in any direction much like the dragonfly but flaps its wings back and forth instead of up and down. During the course of flapping the wings back and forth, two rotational phases occur in which the wings flip. These wing flips are called pronation from upstroke-to-downstroke and supination for downstroke-to-upstroke [38]. Typically, the house fly moves its wings in synchronization either together or 180 degrees out of phase from each other depending on current flight pattern. The angle of attack ranges nearly a full 180 degrees over the course of a full wing stroke. The house fly has a substantially lower Reynolds number (136) than the dragonfly and a flapping frequency of approximately 200 Hz [39, 40].

The third type of insect reviewed were butterflies and moths. They move their wings in a synchronized motion like the house fly, but unlike the fly their wings are not rigid in nature. The moth and butterfly wings bend and twist while in motion. A typical butterfly or moth has a flapping frequency in the 10-25 Hz range and a Reynolds number of approximately 3900. Similar to the house fly's angle of attack, the moth undergoes 120 degrees of bending during its complete wing stroke [41]. A study by Daniel and Combes also shows that in moth wings, the inertial-elastic forces dominate over the fluid dynamic stresses in the previously mentioned flapping frequency range [42]. However, viscous effects are still important for flow structure and cannot be ignored [43].

Many of the mechanical flyers reviewed in the previous section were biomimetic designs because they mimic some aspect of nature's flyers. The devices can draw from the good effects but are not necessarily limited by the restrictions nature places on the insects or birds they draw their inspiration from. Though much inspiration can be drawn from nature, one area still greatly limiting these small flyers' capability is an operating power source. The next section focuses on some potential power sources for MEMS flying devices.

## 2.5 *Potential Power Sources*

One of the main challenges that designers of micro scale flying devices face is how to power such a small device without restricting it to a tethered power source. The most obvious choice would be a battery, but no current batteries are light enough to attach to flyers of this scale. Therefore, alternative energy options must be explored to power MEMS flyers. The focus of this section is to explore a few potential areas that may provide the power required to fly these devices untethered.

Thermoelectric power generation is one possibility for powering these devices. Heat energy is converted into electrical power through heat exchange and combustion in a “swiss roll” design from the University of Southern California as shown in Figure 2.13. There are no moving parts in this device which makes it very appealing. This device can theoretically produce about one watt of power and measures approximately 3.5 cubic millimeters in size [44]. This design is a potential power source for devices on the sub-centimeter scale but is too large for a true MEMS device.



Figure 2.13: Counterflow heat exchanger and combustor capable of producing approximately one watt of power [44].

Another area for powering MEMS devices is through the use of power scavenging techniques. One of the most promising areas in this category is the use of piezoelectric. Electrical power could be extracted from the piezoelectric elements and used to power

other parts of a micro flying device's system [44]. This is especially promising if the wings used to create flying devices produce both lift and power to the other systems of the device.

Autonomous power could also be supplied from a source outside of the device. Optothermal actuation or laser heating has been demonstrated using a 660 nm laser as a way to power a MEMS device [35]. Of course, the problem with this method is that the laser needs to maintain a line of site in order to provide power to the device. Likewise, any change in the incident angle of the laser striking the device would also cause a change in output power.

Fuel cells provide a potential replacement to battery power for small flying devices. Fuel cells convert chemical energy into electrical power through a catalytic process. Proton exchange membranes and direct methanol fuel cells are two types of fuel cells that convert methanol into the power needed to operate a device. Both cells have a problem with methanol cross-over though. Because of this problem, research on the creation of solid oxide fuel cells is currently ongoing [45]. Each of these types of fuel cells produce enough power output to potentially power small flying devices. However, the problem with fuel cells is that they require a place to store the fuel which is greatly limited on a MEMS flying robot.

*2.5.1 Solar Cells.* Solar cell or photovoltaic technology is a very promising technology when it comes to powering MEMS devices. Since 1954, when Bell Laboratories designed the first silicon solar cell, solar cells have been progressively increasing in efficiency. Single silicon solar cells would carry the majority of the development load for solar cells over the next 40 years, maximizing efficiency in the lower 30 percent range with the aid of concentrator systems. While simple solar cells were progressing, the first multi-junction solar cell (MJSC) was developed in 1976. Today, MJSCs have exceeded the maximum possible efficiencies of the single cell devices reaching efficiencies greater than 40 percent [46]. The efficiency of the solar cell is important because it determines how much power a cell will produce based on amount of incident light.

In order for solar cells to create power, the incident light onto the cell must be equal to or greater than the energy of the band gap material. Equation 2.1 shows this relationship where  $h$  is Planck's constant,  $v$  is frequency of light,  $c$  is speed of light, and  $\lambda$  is the wavelength of light in micrometers.

$$hv = \frac{hc}{\lambda} = \frac{1.24}{\lambda} \quad (2.1)$$

If the energy meets or exceeds the band gap energy, a photon is created and in turn an electron hole pair. Once contacts are added, the free electrons flow out of the cell through the contacts to power some external load and return to recombine with holes through a back contact [47]. A simple depiction of how a simple solar cell works is shown in Figure 2.14.

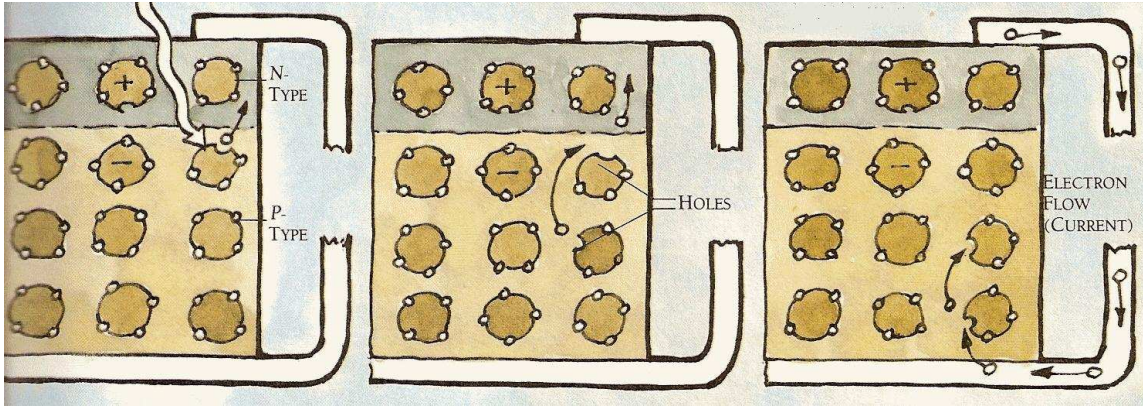


Figure 2.14: This graphic shows how a simple solar cell converts incident light into electrical power [47].

Energy exceeding or less than the band gap material in the simple solar cell will result in losses. For this reason, MJSCs were developed to prevent some of these losses. Each individual solar cell that comprises a MJSC focuses on capturing a particular part of the solar spectrum. The MJSC starts with the widest band gap material on top and proceeds to the material with the lowest band gap on the bottom. This configuration allows the top layer to act as an optical window for lower energy photons to pass through and be absorbed at one of the other sub-cells. The MJSC obtains

better efficiency by absorbing more photons than the single cell configurations [48–54]. Figure 2.15 shows a four junction solar cell that focuses on maximizing efficiency.

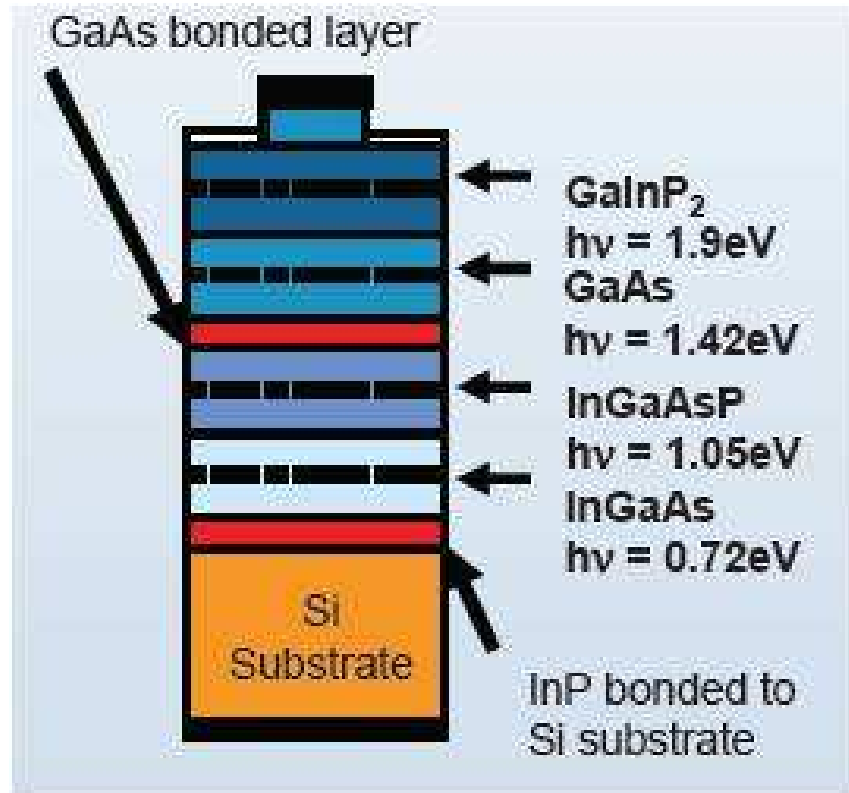


Figure 2.15: This is a four junction solar cell showing the highest band gap on top and lowest band gap on the bottom to maximize photon absorption [50].

Some solar cells have been developed at a small enough scale to be used in miniature and MEMS flyers. One such notable technology is organic solar cells. Though they are currently only about six percent efficient, they can be applied to small structures by spin coating [55]. Organic solar cells also offer a level of flexibility that more traditional forms of solar cells can't provide. One miniature robot by Hollar *et al* utilized an array of 90 solar cells in series to produce 100 micro-watts of power with each cell requiring only 150 square microns of space [56]. This demonstrates the possibility of using photovoltaic energy to power a MEMS flying device.

The ability to gather power from the sun makes the solar cell a viable power source for any autonomous robot. Having the capability to produce individual solar

cells at the micrometer scale makes it especially appealing to MEMS devices. The drawback to photovoltaic energy however is the fact that it draws its energy from the sun. This limits the operation of the device to daylight hours or requires an additional element on the device to store energy, which would preclude the advantage of the solar cell over a battery system to begin with.

## ***2.6 Chapter Summary***

In this chapter, a brief history of how the field of MEMS evolved and the initiative to develop miniature flying devices were discussed. Many miniature flyers utilizing fixed, rotary, and flapping schemes were reviewed. Insect flight behavior was also reviewed to provide a better understanding of how miniature flyers are capable of achieving flight. This chapter also looked at some different schemes that could potentially power these miniature flying devices. Photovoltaic power, particularly, was explored as an option to power a MEMS flying device.



## III. Theory

### 3.1 Chapter Overview

The purpose of this chapter is to delve into the theory behind small flying devices. This chapter specifically discusses aerodynamic theory and how it relates to MEMS devices. Part of this chapter also focuses on different actuation schemes for MEMS devices.

### 3.2 Aerodynamics

How an object moves through the medium in which it is submerged is referred to as aerodynamics. Common aircraft such as helicopters and airplanes are governed by conventional aerodynamics which means they operate at a Reynolds number greater than 10,000. As devices decrease in size, these aerodynamic relationships begin to break down. The following sections briefly look at fundamental aerodynamic theory and how Reynolds number research on insects may prove useful for MEMS characterization.

*3.2.1 Conventional Aerodynamics.* There are four forces that act on all aircraft: lift, weight, thrust, and drag. These can be further broken down into two pairs of opposing forces lift/weight and thrust/drag. When the lift force is greater than the force of the weight, the aircraft will rise into the air. The thrust force acts in the direction of flight and is the primary difference in aerodynamic characteristics between rotary and fixed winged aircraft [57]. This is why a fixed wing aircraft flies only forward while a rotary wing aircraft can fly in many directions. Figure 3.1 (a) and Figure 3.1 (b) depict the difference between the four forces as they act on fixed wing and rotary aircraft, respectively.

Lift and drag forces are expressed by Equation 3.1 and Equation 3.2 where  $C_L$ ,  $C_D$ ,  $\rho$ ,  $U_F$ , and  $S$  are the lift coefficient, drag coefficient, air density, flight speed/wing

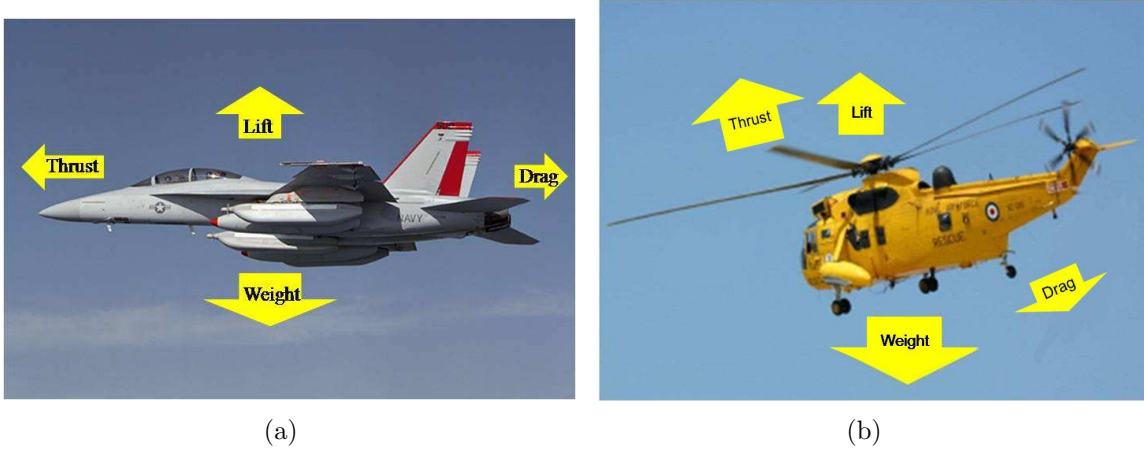


Figure 3.1: Aerodynamic forces acting on (a) fixed wing aircraft in parallel flight and (b) rotary wing aircraft in forward flight.

tip velocity, and surface area, respectively [25].

$$F_L = \frac{1}{2} C_L \rho (U_F)^2 S \quad (3.1)$$

$$F_D = \frac{1}{2} C_D \rho (U_F)^2 S \quad (3.2)$$

Both of these terms have a scaling factor of  $S^3$  which is slightly greater than the gravitational scaling factor of  $S^4$ . Based on the size of a MEMS flying device, both of these forces will be extremely small.

Lift force on a wing is obtained by air flow over an airfoil cross section. As air strikes the airfoil, it is divided over and under the wing. The airfoil is curved in a manner such that the air passing over the wing moves faster than the air flow beneath the wing creating a pressure differential. Since the air pressure is greater under the wing than above the wing, the wing is forced upward. This force is the lift force [57]. Figure 3.2 shows lift created by air flow over an airfoil.

The Reynolds number is a dimensionless number used to characterize flow behavior in a fluid medium. Equation 3.3 is used to calculate the Reynolds number of a flapping device in flight where  $c$  is chord length,  $f$  is the frequency,  $H$  is flapping

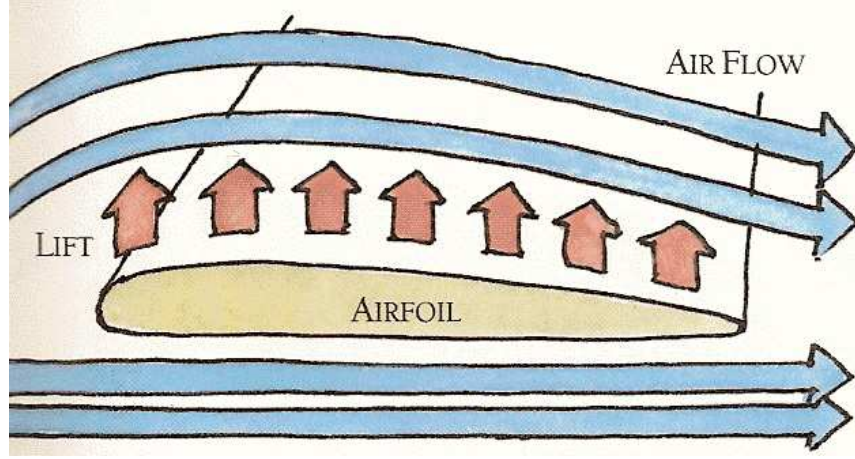


Figure 3.2: This graphic shows how air splitting over an airfoil causes a lift force on that airfoil [57].

amplitude, and  $\nu$  is the kinematic viscosity of the fluid [2].

$$Re = \frac{2\pi * Hfc}{\nu} \quad (3.3)$$

Equation 3.4 is used to calculate the Reynolds number for a hovering flapping device where  $\Phi$  is the wing beat amplitude in radians,  $f$  is flapping frequency,  $R$  is wingspan,  $\Lambda$  is the aspect ratio accounting for multiple wings, and  $\nu$  is the kinematic viscosity of the fluid [58].

$$Re = \frac{\Phi * fR^2}{\nu} \frac{4}{\Lambda} \quad (3.4)$$

The value of the Reynolds number is used to classify fluids as laminar or turbulent. Laminar flow occurs for Reynolds numbers up to approximately 100,000 after which point flow is considered turbulent. Viscous forces dominate laminar flow which is smooth and constant. Turbulent flow occurs when inertial forces begin to dominate the ratio, commonly resulting in a LEV. However, in the case of high Reynolds numbers, inertial forces cause the vortices to dissipate rendering them negligible for devices operating at high Reynolds numbers [25].

Most aircraft operate in the higher Reynolds number regime due to their size and speed. Figure 3.3 shows the flying device size and weight relationship to the

Reynolds number. Larger aircraft rely on inertial forces to sustain flight while MAVs and insects operate under laminar flow with drag being a dominate force. A circle was added outside the chart in Figure 3.3 to show how MEMS devices relate to the other flyers. The Reynolds number and gross weight of these MEMS devices are between  $10^{-3}$ - $10^{-2}$  and  $10^{-9}$ - $10^{-8}$ , respectively.

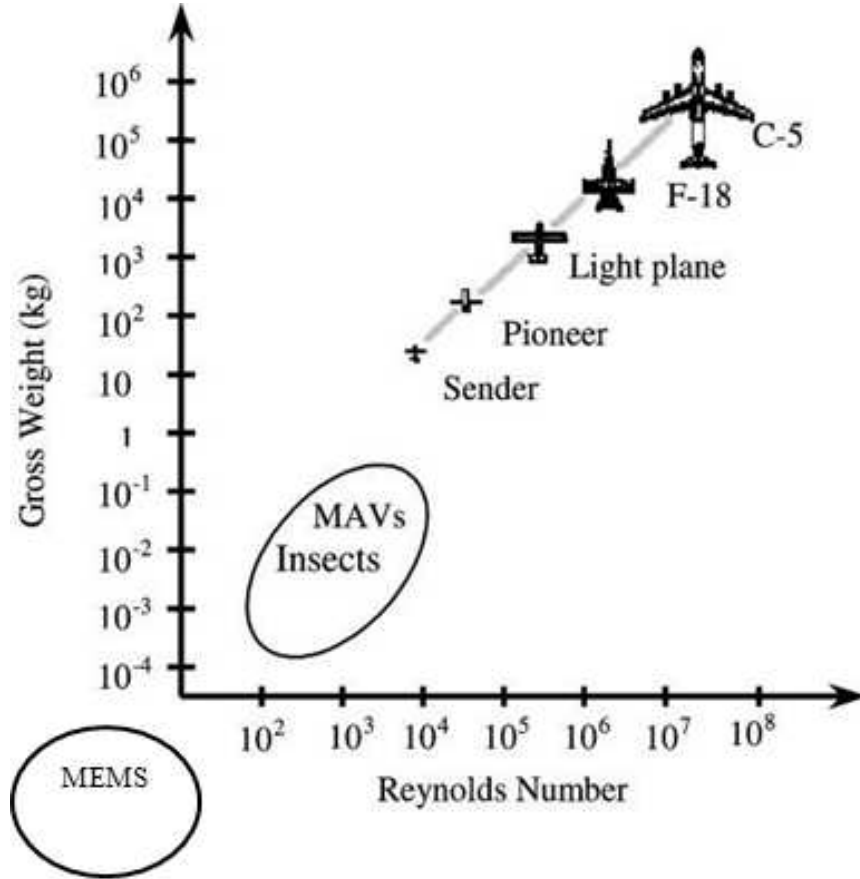


Figure 3.3: Comparison of different aircraft's weight plotted on a logarithmic scale against Reynolds number. This shows the range of different flyers and the affect weight plays on their Reynolds number [29].

Wing aspect ratio,  $\Lambda$ , is another factor that affects aerodynamics. Equation 3.5 defines the aspect ratio of wings [59].

$$\Lambda = \frac{(wingspan)^2}{area} \quad (3.5)$$

In general low aspect ratio wings have blunter tips which causes an induced drag. Long, thin wings that have a higher aspect ratio create less induced drag. This results in more force per area than low aspect ratio wings and a higher efficiency. However, these aerodynamic properties often break down under unsteady conditions such as flapping [59].

*3.2.2 Aerodynamics at Low Reynolds Numbers.* The effects of aerodynamics at low Reynolds numbers are still largely unexplored. Experimental models/empirical data on MAVs and insects help in forming hypotheses for what might happen with a MEMS flying device. However, moving from the size of MAVs and insects down to a MEMS size flyer results in a drastic change to the Reynolds number value.

Not all flight fits into either straight laminar or turbulent flow. Birds and many fixed wing aircraft use flapping motion during the course of flight which creates a quasi-steady flow due to minimal flapping speeds. In the case of an insect, who uses mainly flapping motion to achieve flight, unsteady state flow is created. The transition between these two states often occur when flapping speed exceeds flight speed. Reduced frequency,  $k$ , is the measure of unsteadiness of flow and is defined by Equation 3.6 for forward flight where  $f$  is frequency,  $c$  is chord length, and  $V$  is freestream velocity [2].

$$k = \frac{\pi * fc}{V} \quad (3.6)$$

The reduced frequency for a hovering device is defined by Equation 3.7 where  $\Phi$  is wing beat amplitude in radians and  $\Lambda$  is aspect ratio [58].

$$k = \frac{\pi}{\Phi * \Lambda} \quad (3.7)$$

Figure 3.4 shows that a MEMS size device, which is significantly smaller in terms of body mass than a MAV device, clearly falls into the unsteady state regime [30].

As mentioned earlier, wing aspect ratio behaves differently for the unsteady state flow associated with flapping devices. Combes and Daniel have studied the

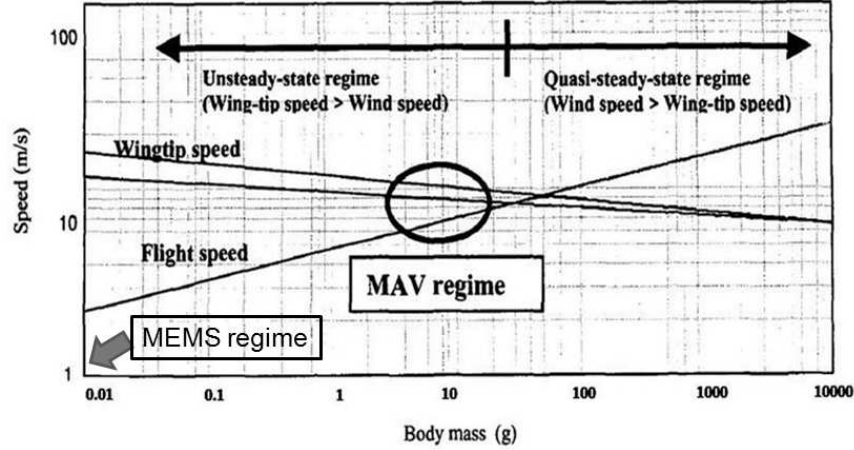


Figure 3.4: This graphic shows the difference between unsteady and quasi steady state regimes in small flying devices is caused by the ratio of wing tip speed to flight speed [30]. The speed and body mass for the MEMS devices in this thesis are both on the order of  $10^{-4}$  which is off the chart shown here.

effects on flapping wings that support slightly different aerodynamic properties than the steady state case. In general, high aspect ratio wings generate more thrust and are more efficient than lower aspect ratio wings. However, low aspect ratio wings that flap at higher frequencies can produce more thrust and operate at higher efficiency than some high aspect ratio wings. Additionally, wings with greater distributed area in the outer portion of the wing generate greater thrust but operate less efficient. More rigid wings also generate more thrust than flexible ones but once again are less efficient. The variation of chord length, which is the distance from the leading to the trailing edge of a wing, in low aspect ratio wings is responsible for the increase or decrease of efficiency [59].

Closely coupled to aspect ratio is the length of the flyer. Much like weight, the length of the flyer can affect the Reynolds number of the device. The smaller the characteristic length of the flyer, the lower the Reynolds number. Figure 3.5 shows the correlation between characteristic length and the Reynolds number for flyers smaller than insects up through the jumbo jet.

Insects are the topic of much research for improving flight in small flying devices because of their superior flying capabilities in the unsteady state regime. Theory

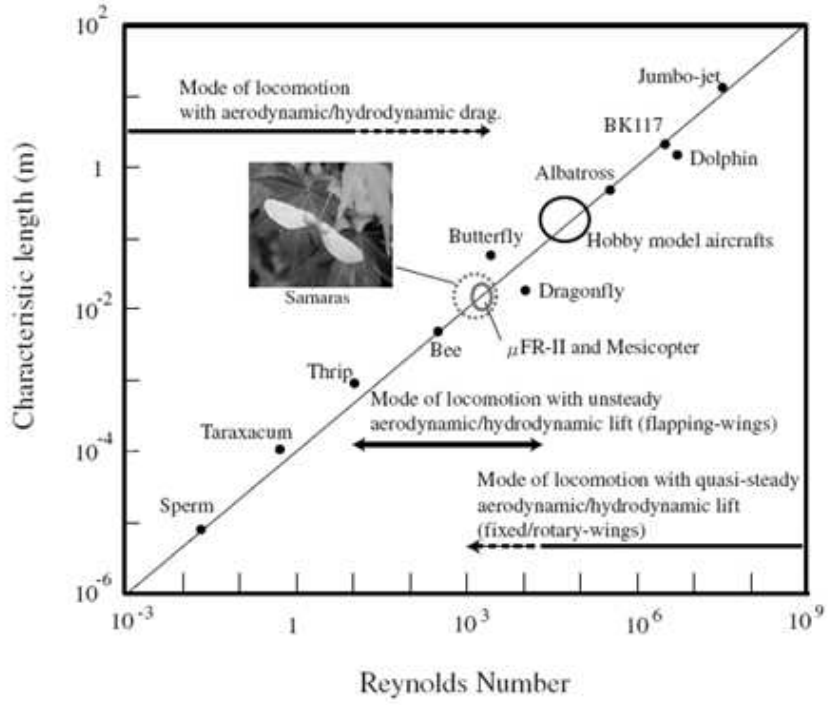


Figure 3.5: This graphic shows a comparison between the length of an object and its corresponding Reynolds number [25].

suggests that unsteady LEVs improve the lift capability of insects while attached flows cannot provide the very high lift coefficients that LEVs do. Studies on dragonfly flight have shown that the LEV is continuous across the entire wing span. In steady state flow, this LEV is shed nearly instantaneously along the wing's span. Therefore, the ability to control this LEV allows the insects to achieve increased lift by controlling angle of attack in flapping their wings [37].

One fundamental aerodynamic parameter that governs LEV dynamics is the Strouhal number. Equation 3.8 defines the Strouhal number where  $f$  is stroke frequency,  $a$  is wing amplitude, and  $U$  is forward velocity in the medium [37].

$$St = \frac{fa}{U} \quad (3.8)$$

The Strouhal number of insects is typically between 0.1 and 0.3. This number determines the maximum angle of attack in the wing as well as the intrinsic timescales

of flapping. Therefore, this serves as a forcing function for aerodynamics in LEV analysis [37].

### 3.3 Actuators

The wings of a device must create at least as much lift as the weight of the object in order for the device to achieve controlled lift off. In flapping wings, the frequency, force, and displacement of the wings can all help to accomplish this goal. This section will review different MEMS actuators used for achieving these three different aspects.

There are four general classifications for actuators in MEMS devices: electrostatic, piezoelectric, thermal, and magnetic. Each of these categories contains many devices used to create force and displacement output [60]. An electrostatic device and several thermal devices are reviewed in this paper. Devices from the other categories were not reviewed since they could not be fabricated using PolyMUMPs<sup>TM</sup>.

Figure 3.6 shows maximum displacement versus maximum force for different actuation schemes. The black circles represent actuators for MEMS scale devices. Of these actuation schemes, the comb drive, thermal actuators (solid expansion), and thermal bimorph are capable of being fabricated through the PolyMUMPs<sup>TM</sup> process used for device fabrication in this thesis [60].

Figure 3.7 shows maximum displacement versus maximum frequency for different actuation schemes. The black circles again represent actuators for MEMS scale devices. Solid expansion and thermal bimorph both have a narrow operating range compared to the comb drive actuator. It is clear from Figures 3.6 and 3.7 that trade-offs occur for each type of actuator. A comparison of these three actuators is shown in Table 3.1 [60].

*3.3.1 Thermal Actuators.* The solid expansion actuators reviewed in this paper all use thermal expansion as their actuation scheme. The single hot arm actuator and double hot arm actuator are shown in Figure 3.8 (a) and Figure 3.8 (b), respectfully. In the single hot arm, a voltage is applied at one anchor while the other



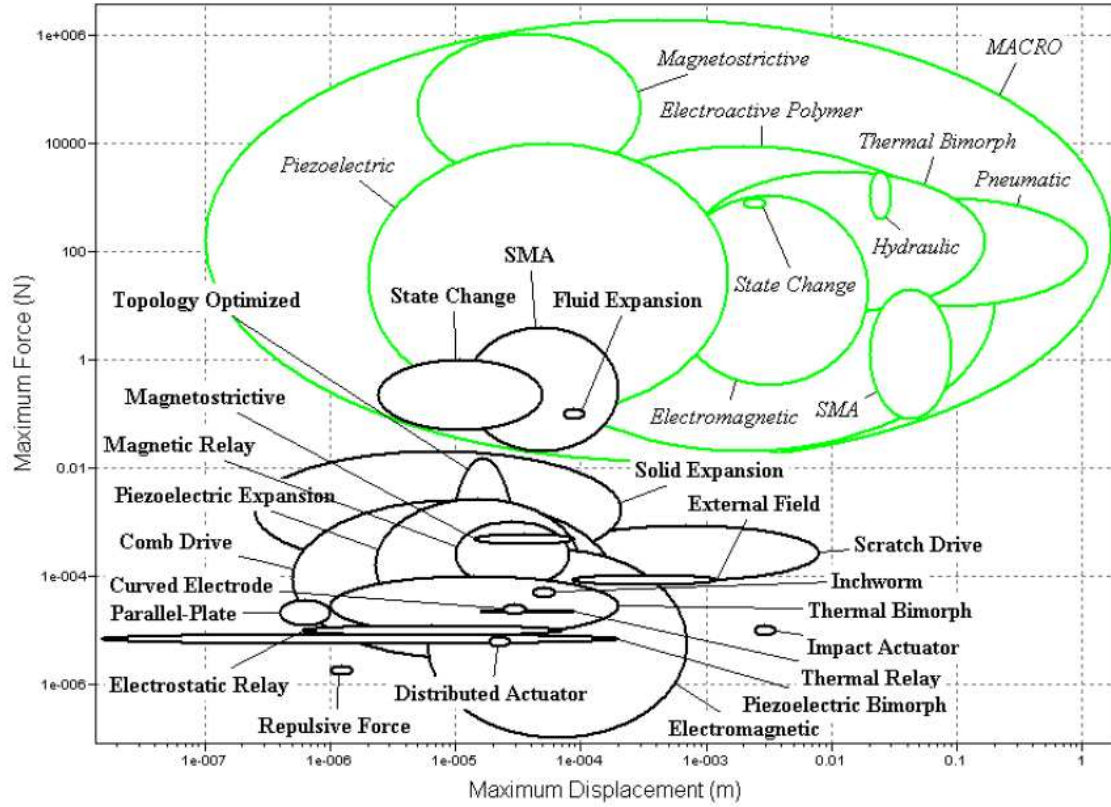


Figure 3.6: MEMS (black circles) and macro (green circles) scale actuators are compared in terms of maximum force and displacement [60].

anchor is electrically grounded. As current flows through the device, joule heating occurs. Since the cross sectional area of the hot arm is less than the area of the cold arm, the hot arm generates more heat. Therefore, the hot arm expands further than the cold arm resulting in a displacement in the direction of the cold arm. The frequency response in this scheme is limited by how quickly the hot arm cools between pulses. The double hot arm works in the same fashion as the single hot arm but is capable of a greater output force due to dual hot arm expansions. However, the displacement of the double hot arm is less than that of the single hot arm.

Another solid expansion actuator is the chevron or bent beam actuator. This device uses the same joule heating principles as the hot arm devices but produces an in-plane linear motion as opposed to the arching motion of the hot arm actuators. Voltage is applied to the terminals and heating causes thermal elongation of the beam

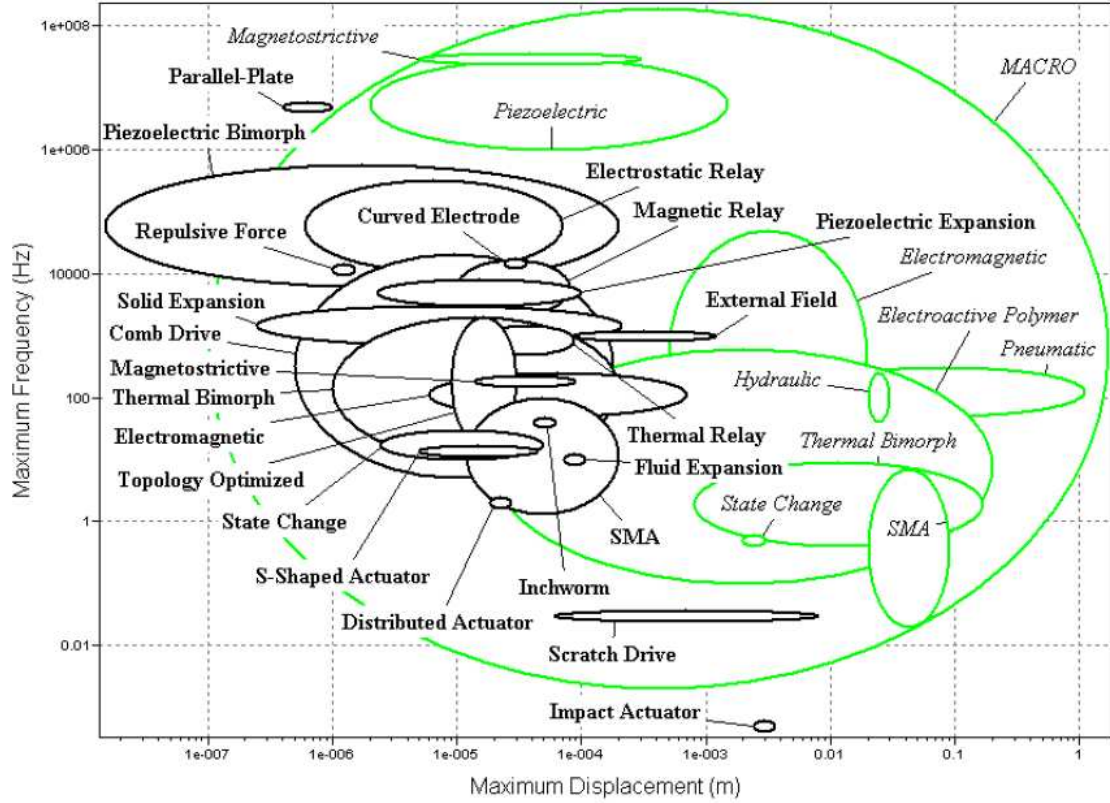


Figure 3.7: MEMS (black circles) and macro (green circles) scale actuators are compared in terms of maximum frequency and displacement [60].

in the desired direction. The pre-bent angle sets up the force component in the desired direction, reducing the probability of an out of plane deflection. Figure 3.9 shows the configuration of the bent beam actuator. Due to its single direction deflection, the chevron actuator produces more force than the hot arm actuators. However, it provides less deflection than the hot arm designs [61].

Combining solid expansion actuators allows for increased force. This is important when dealing with larger MEMS structures that require more force than the individual actuators can provide. Also, operating at the performance edge of a device significantly reduces the reliability of a system. Therefore, grouping these solid expansion devices together can improve performance in terms of force and reliability but reduces maximum deflection due to yoked attachment [61].

Table 3.1: This table compares the maximum force, displacement, and frequency of three actuators (all values approximated from Figures 3.6 and 3.7).

Actuator Comparison			
Actuator	Max Force (mN)	Max Displacement ( $\mu\text{m}$ )	Max Frequency (Hz)
comb drive	1	200	20000
thermal actuator	10	200	4000
thermal bimorph	0.1	200	2000

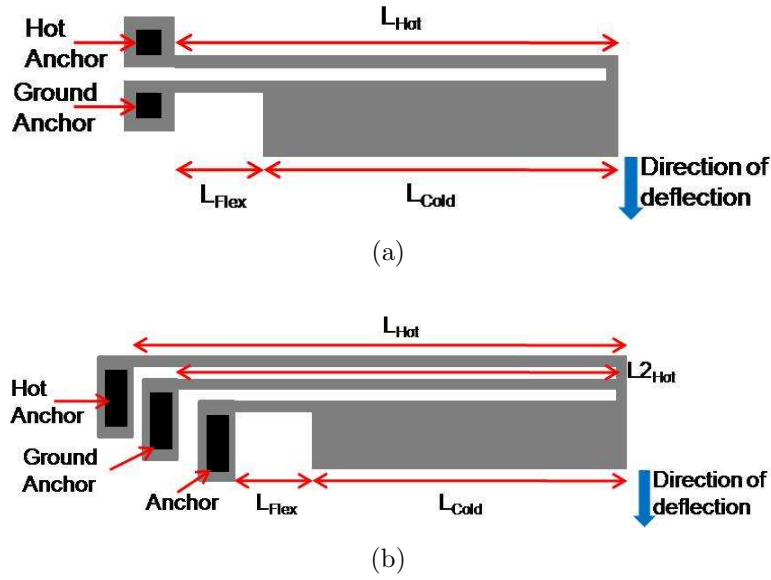


Figure 3.8: Thermal actuator diagrams for the (a) single hot arm and (b) double hot arm.

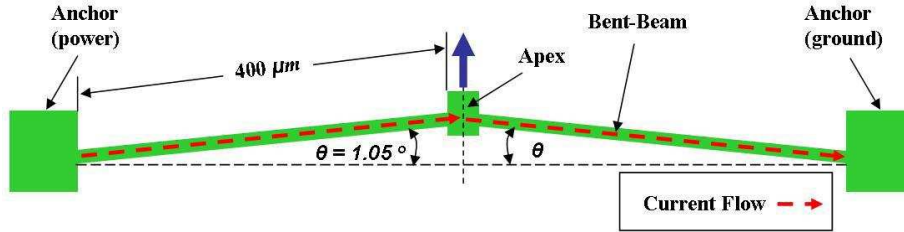


Figure 3.9: Layout of a single bent beam actuator pre-bent to force deflection in the direction of the apex [61].

**3.3.2 Hybrid Actuator.** Another type of actuator that uses both residual stress properties and thermal actuation is the thermal bimorph. A thermal bimorph

structure is comprised of materials with different TCE. Due to the different TCE, the materials react differently to joule heating. However, before discussing what happens under joule heating conditions, the residual stress properties should be considered for a common pairing of bimorph materials such as polysilicon and metal.

Residual stress is a result of thermal depositions and dopant gradients within the fabricated material layers. Table 3.2 shows common values related to residual stress for polysilicon and gold layers fabricated with the PolyMUMPs<sup>TM</sup> process. Residual stress values can also be calculated after a device is released using Equation 3.9 where  $y$  is deflection ( $\mu\text{m}$ ),  $t_p$  is thickness of the polysilicon layer ( $\mu\text{m}$ ),  $E'$  is the Biaxial Modulus,  $t_f$  is the thickness of the metal film ( $\mu\text{m}$ ), and  $x$  is the length of the structure ( $\mu\text{m}$ ).

$$\sigma_{res} = \frac{y * t_p^2 * E'}{3 * t_f * x^2} \quad (3.9)$$

Residual stress is classified as either compressive (C) or tensile (T) with compressive (-) indicating compaction and tensile (+) indicating expansion. The gold layer has a higher tensile stress than the polysilicon compressive stress which results in a natural upward deflection of the released bimorph structure. This out of plane deflection relieves the stress on the structure.

Table 3.2: Typical PolyMUMPs<sup>TM</sup> material properties [62].

<b>Thermal Bimorph Layer Properties</b>			
Variable	Poly1	Poly2	Gold
Young's Modulus (GPa)	131	162	78
Poisson's Ratio	0.22	0.22	0.44
TCE ( $\text{K}^{-1}$ )	2.3 E-6	2.3 E-6	14.3 E-6
Layer Thickness ( $\mu\text{m}$ )	2	1.5	0.5
Residual Stress (MPa)	5 C	7 C	13 T

This natural deflection caused by residual stress can be overcome by applying a voltage bias to the bimorph structure. As the structure experiences joule heating from the applied bias, the metal layer expands more than the polysilicon layer because of the differences in TCE values. Since the metal layer expands more than the polysilicon

layer, the structure deflects in the direction of the polysilicon layer. Figure 3.10 shows a side view of a thermal bimorph design.

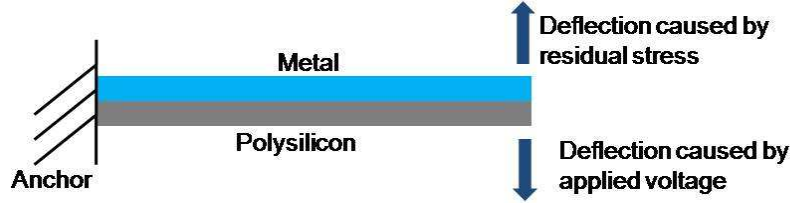


Figure 3.10: Thermal bimorph comprised of a polysilicon and metal layer. Once released, the structure deflects upward due to residual stress and downward under increasing applied voltage.

It is clear that there are tradeoffs when dealing with these different thermal actuator designs. Depending on the application, picking an actuator or group of actuators based on maximum force or deflection may be appropriate. A quick comparison of the four thermal devices reviewed is provided in Table 3.3.

Table 3.3: This table compares the required power, generated force, and displacement of four thermal actuators [61, 63].

Thermal Actuator Comparison			
Actuator	Power (mW)	Force ( $\mu\text{N}$ )	Displacement ( $\mu\text{m}$ )
Single Hot Arm	164	12.7	25.4
Double Hot Arm	98	26	19.6
Bent Beam	55.2	74.8	8.54
Bimorph	174	17	214

Each of these devices are possible for a flapping wing design. In addition to the considerations of force and displacement for actuation, the size of the devices should also be considered. The hot arm designs by themselves are smaller than the chevron design, but when combining the devices the chevron takes up less area than the hot arm designs. The thermal bimorph on the other hand can serve as both the actuator and the desired design structure.

**3.3.3 Electrostatic Actuator.** The comb drive resonator, an electrostatic actuator, is capable of a larger range of applications than the solid expansion actuators

due to its greater frequency domain (see Figure 3.7). Several of the resonators components are more easily controlled than the thermal actuators. For instance, scaling capacitance down in electrostatic MEMS devices works very well. The gap between comb fingers in the resonator are generally only a few microns apart which is on the order of the mean free path of air molecules. This allows the electric field to breakdown easily making it possible for the comb drive to handle high voltage applications [25].

Figure 3.11 shows the basic layout of a comb resonator. The comb fingers attached to the shuttle are mobile while the comb fingers attached to the drive and sense lines are fixed. The drive signal enters through the drive line and exits through the interconnected shuttle-truss component. The shuttle-truss component is connected through flexure springs which allow lateral movement from the resultant spring-mass-damper system. The inner comb fingers move in and out of the fixed comb fingers upon reaching resonance. Resonance occurs when the applied voltage signal matches the natural frequency of the spring-mass mechanical system.

Like the solid expansion devices, the comb drive can be combined in series to gain greater output forces. These devices can also be setup to work out of phase with one another to create circular motion if desired. In addition to the high voltage required to operate this device, comb drives take considerably more space when compared to the thermal actuators. Both of these hinder the ability to produce lift and scavenge for power due to increased weight and input power requirements, respectively.

### ***3.4 Chapter Summary***

This chapter reviewed many engineering aspects from conventional aerodynamics to MEMS actuation. Low Reynolds number flight characteristics were discussed to better understand the possibility of MEMS flight. The review of actuators showed thermal actuators are a good fit for flapping wing applications. In particular, the thermal bimorph integrates actuation and design into the same structure making it an excellent choice for flapping wings. Equations were presented for various aspects of MEMS flight that will be used to develop models and fabricate devices.

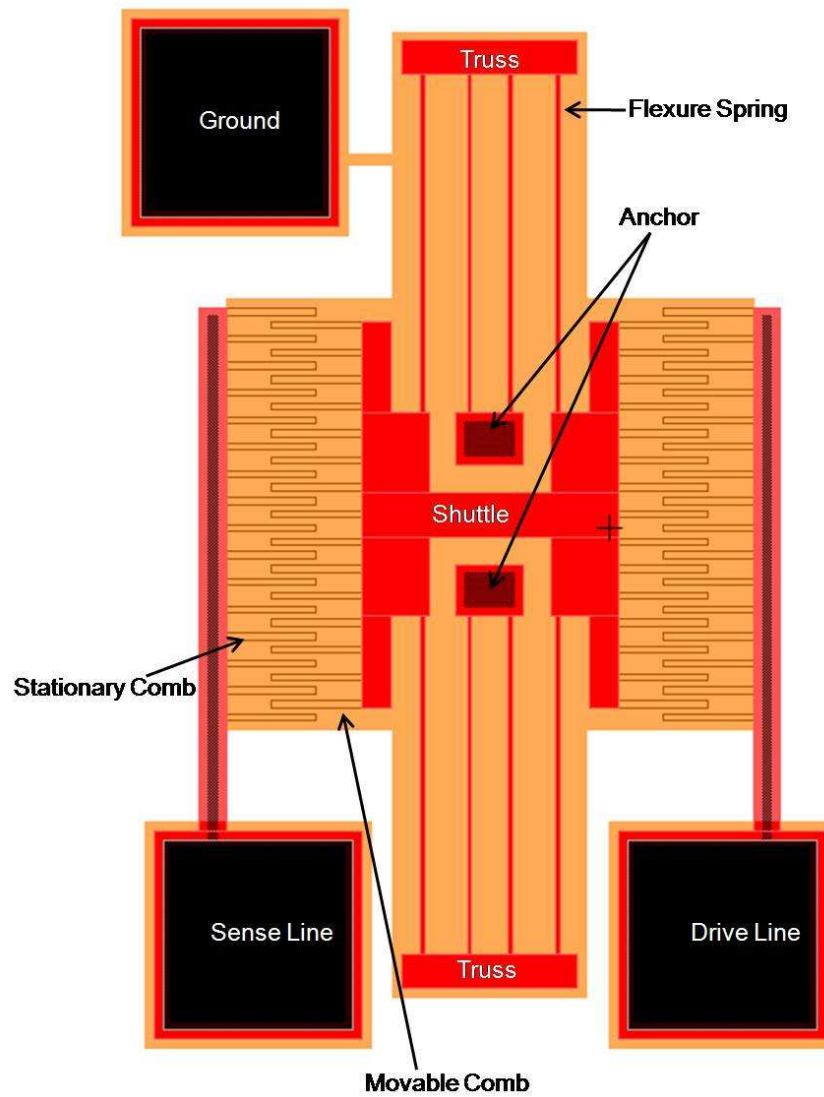


Figure 3.11: Image of a comb drive showing basic components and electrical configuration.

## IV. Fabrication and Design

### 4.1 Chapter Overview

This chapter discusses the process used to fabricate the MEMS designs of this thesis. Biology inspired and thermal actuator driven wing designs are presented in this chapter. Determination of the wing structures and their operating schemes are also described in the following sections.

### 4.2 Fabrication

Conceptual designs are fabricated using the PolyMUMPs<sup>TM</sup> process. This process is a surface micromachining process with three polysilicon layers and two sacrificial oxide layers. Surface micromachining is an additive process starting with a substrate and building layers on top of each previous layer. Each layer of thin film is deposited and patterned using photolithography; then the layer is etched to create the desired features. In PolyMUMPs<sup>TM</sup>, each polysilicon layer is followed by a sacrificial silicon dioxide layer. These sacrificial layers are removed after fabrication to release the second and third polysilicon layers. A key point to keep in mind when using this process is the fact that each layer is conformal to the previously deposited layer [62].

*4.2.1 PolyMUMPs<sup>TM</sup>.* The MUMPs<sup>®</sup> process begins with a <100> n-type silicon wafer that is heavily doped with phosphorus to reduce charge feed through to the substrate. A 600 nm silicon nitride layer is added for electrical isolation using low pressure chemical vapor deposition (LPCVD) [62]. The substrate and nitride layers are the same for each PolyMUMPs<sup>TM</sup> run with the additional layers being user defined.

A 500 nm layer of polysilicon (poly0) is deposited by LPCVD and patterned by photolithography to the user's specified design. After patterning the layer, it is etched via reactive ion etching (RIE). Next, a 2  $\mu\text{m}$  phosphosilicate glass (PSG) sacrificial layer (oxide1) is deposited by LPCVD and annealed at 1050°C. The user can design dimples into this structural layer to aid in stiction prevention or the unexpected



bonding in the MEMS device. These dimples are small protrusions (750 nm) which reduce surface area contact between the layers. If the first structural layer needs to attach to the poly0 layer, an anchor hole (anchor1) needs to be patterned before the next deposition [62].

Next, the first structural layer of polysilicon (poly1) is deposited by LPCVD at 2  $\mu\text{m}$  thick. This layer conforms to the previously deposited layers as does each subsequent layer. This layer is then patterned and capped with a 200 nm layer of PSG that undergoes annealing at 1050°C. This dopes the poly1 layer with phosphorus and reduces its resistivity [62].

The second oxide layer (oxide2), which is 750 nm, is deposited after the poly1 layer. Two mask options are available for the user on the oxide2 layer. A via etch connects the poly1 and poly2 structural layers providing an electrical and mechanical connection between the two layers. The anchor2 etch hole removes both oxide1 and oxide2 providing an anchor to the poly0 layer or the nitride depending on previously designed layers. The final structural layer of polysilicon (poly2) is then deposited and etched just like the poly1 layer, only this layer is 1.5  $\mu\text{m}$  thick [62].

The final deposition is a half micron of gold evaporated directly onto the poly2 layer. Evaporation prevents gold from adhering to the recessed side walls. Since gold doesn't adhere to the side walls, metal lift-off is performed to remove the additional unwanted gold. The remaining gold can serve as probing, bonding, electrical routing, and highly reflective mirror surfaces for the designed devices [62]. Figure 4.1 shows a comprehensive diagram integrating all design features of the MUMPs<sup>®</sup> process [62].

The last step of the PolyMUMPs<sup>™</sup> process is the release of the sacrificial layers. Two different release methods were used over the course of this thesis work, one using the Tousimus<sup>®</sup> critical point dryer and the other using a hot plate. Process followers for both methods are located in Appendix B, Section B.1. In general, both processes start by removing the photoresist with acetone. To release the poly1 and poly2 layers, the chip is submerged in 49 percent hydrofluoric acid (HF). The time required in the

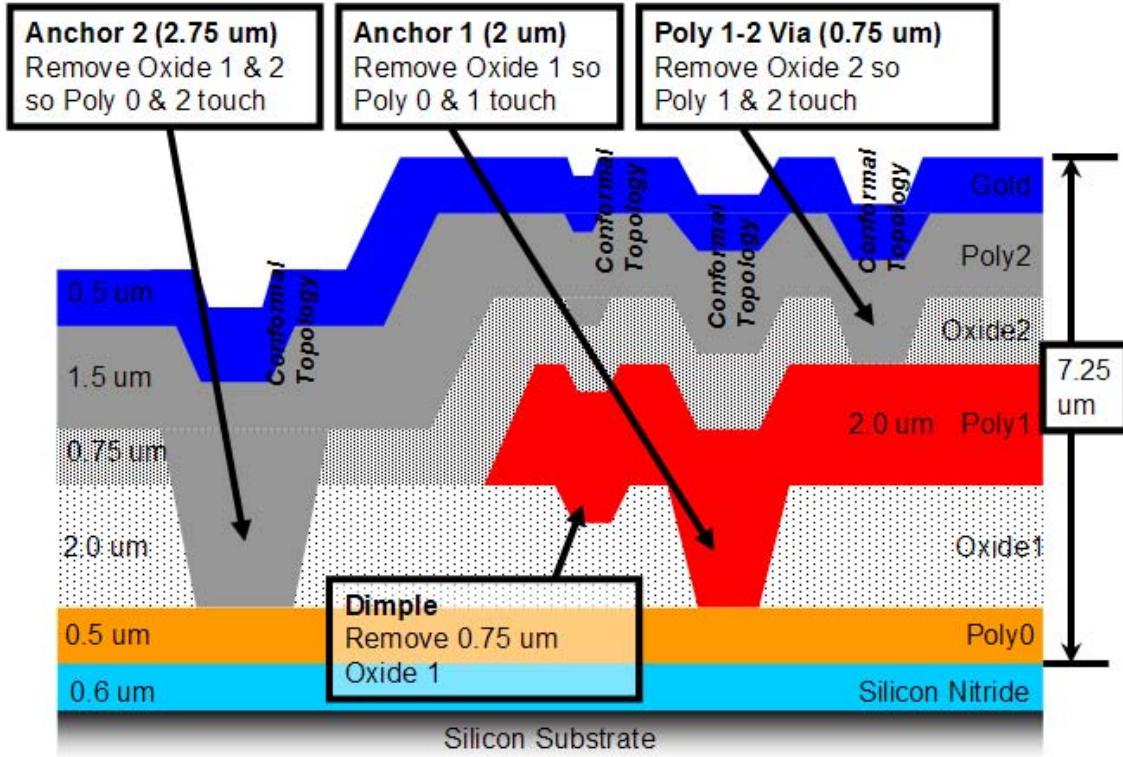


Figure 4.1: Comprehensive graphic showing the conformal nature of PolyMUMPs<sup>TM</sup> thin film layers with accompanying etches [25].

HF etchant is dependent on the size and features of the designs. To stop continual HF etching of the chip, it is submerged in methanol or isopropanol for 15 minutes prior to drying. This drying process helps minimize stiction of MEMS devices.

*4.2.2 Post Processing.* In order to fully develop some designs, post processing is necessary prior to release. In the case of this thesis work, a back side etch of the substrate and nitride layers is necessary to both decrease the device weight and allow the wings to reach their full deflection potential. The first step is to thin the 700  $\mu\text{m}$  substrate down to approximately 400  $\mu\text{m}$  via deep reactive ion etching (DRIE). A 2-3  $\mu\text{m}$  oxide layer is deposited on the chip back side by Plasma Enhanced Chemical Vapor Deposition (PECVD); this will serve as the mask for the back side etch. In order to pattern this oxide to match the designs, post fabrication masks were designed and developed by Photosciences<sup>©</sup> for MUMPs<sup>®</sup> runs 83 and 84 as seen in

Appendix A. A thick layer of Shipley's<sup>TM</sup> 1818 photoresist is applied to the back side of the wafer. This is patterned according to the developed masks using the back side overlay alignment feature of the EVG620 mask aligner. Once the chip is exposed and patterned, it is developed using 351 developer. This pattern is transferred into the oxide layer via RIE and serves as the final mask for the DRIE step. A DRIE is then performed to etch through the backside of the wafer to remove unwanted materials. The photoresist is then removed using acetone and the MEMS device is ready for release using the same release process mentioned in Section 4.2.1. A detailed description of the backside alignment process is described in Appendix B, Section B.2.

Figure 4.2 (a) and (b) show a fabricated MUMPs<sup>®</sup> run 83 chip and corresponding back side pattern prepared for DRIE, respectively. The horizontal flip of the pattern matches the design when the chip is turned upside down. The patterned boxes correspond to the different types of wings on the chip and represent locations that will have holes after the DRIE process. By creating these holes, the wings are allowed to continue deflecting as applied bias increases.

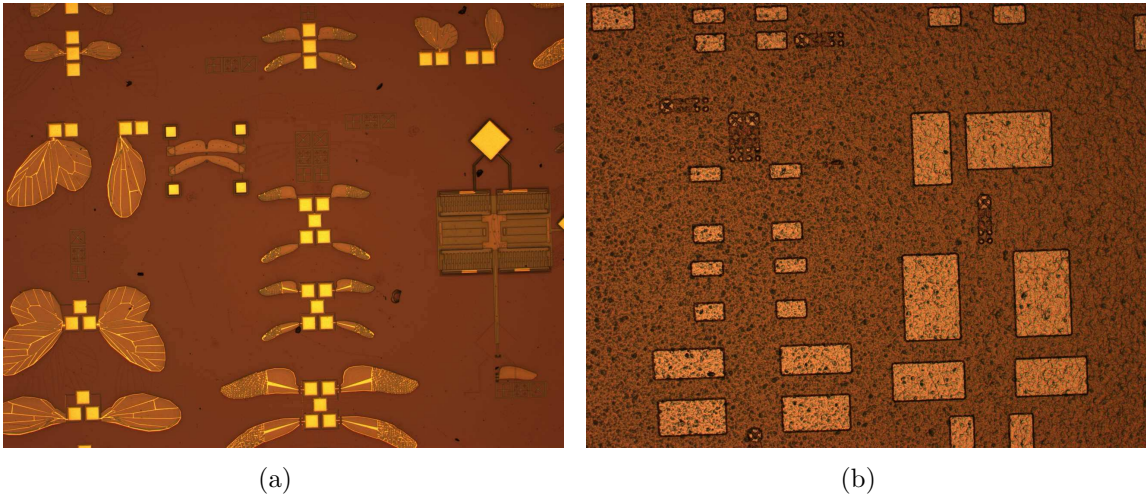


Figure 4.2: (a) Bio-wings on the front of the chip (b) Corresponding back side patterned DRIE mask

### 4.3 Design

This thesis focused on two categories of design; biology inspired wing designs and thermal actuator driven wings. The motivation behind the bio wing designs and the assembly of the thermal actuator designs are also examined closer. Bond pads used for device actuation were included as part of each wing design. This offered the flexibility to probe the pads individually or wire bond them out to the pins of a chip package. The following sections will look at each of the designs in more detail.

*4.3.1 Biology Inspired Designs.* Nature has countless numbers of different insect species capable of flight. The wing designs in this thesis focus on three of those insects: the dragonfly, the house fly, and the butterfly. Each of these three design structures were fabricated to actuate through the use of a thermal bimorph structure. The bio-wings were also scaled down from the actual insect size wings to meet the MEMS criteria of less than one millimeter in size. Each insect wing was scaled down differently to meet the criteria and will be discussed in its respective section.

General improvements were made for each of the three bio-wing designs from MUMPs® run 83 to run 84. One significant change was to anchor the actuator lines to the substrate to provided a better heat-sink capability for the device. This prevents the bias lines from burning up before reaching the desired actuation level. Another upgrade for run 84 was to force current further into the tip of the wings by altering the least resistance current path. The next few sections will look at each general bio-design in more detail.

*4.3.1.1 Dragonfly Wings.* The dragonfly has the ability to hover and fly in almost any direction through individual control of their four wings. Dragonflies also move their wings up and down instead of back and forth like many insects. With this information in mind, a set of four dragonfly wings were laid out in L-edit by tracing a graphic of an actual set of dragonfly wings. A set of dragonfly wings consist of four wings, a pair of forewings and a pair of back wings. The design layout

is a bimorph structure consisting of the poly2 and gold layers. Each wing has its own electrothermal actuation pad so the device can emulate the actual dragonfly by controlling each wing individually. Figure 4.3 shows the design of individually activated dragonfly wings that compose one complete wing system.

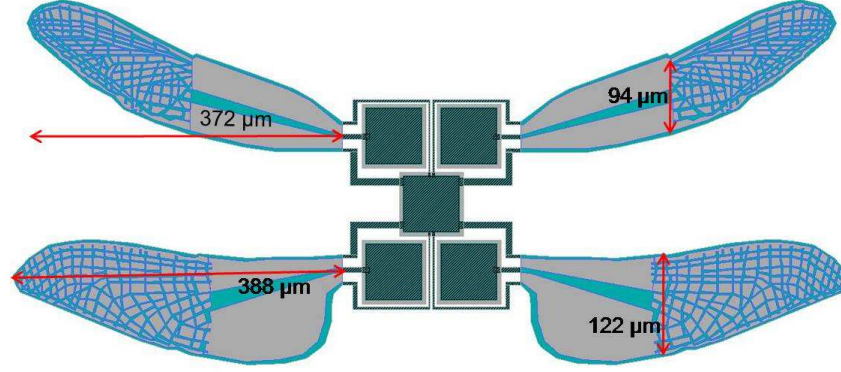


Figure 4.3: This center actuated wing design consists of four individually actuated wings that emulate the dragonfly insect.

Several test wing structures were designed for the dragonfly wings. Each of the test wings focused on actuating the wings from a different point, but each wing was still electro-thermally activated. One test scheme activated the wing through the leading edge and another through the trailing edge. An additional test wing was setup for center activation. The wings were tested under different actuation schemes to determine which scheme would provide the best deflection. Additionally, the wings were tested to see if they had any rotational translation during deflection because many insects use rotational translation during flapping to increase lift.

In addition to these different activation schemes, different size wings were also tested. The different size wings were designed to compare the amount of deflection potential based on wing size while all other factors remained unchanged. A smaller set of wings measuring approximately  $200\text{ }\mu\text{m}$  by  $45\text{ }\mu\text{m}$  for the forewing and  $195\text{ }\mu\text{m}$  by  $60\text{ }\mu\text{m}$  for the back wing's span and chord respectively were one size wing design. The larger set of wings measure  $372\text{ }\mu\text{m}$  by  $94\text{ }\mu\text{m}$  for the forewing and  $388\text{ }\mu\text{m}$  by  $122\text{ }\mu\text{m}$  for the back wing's span and chord, respectively. The designed dragonfly

wings were 165 and 330 times smaller than the real dragonfly wings for the large and small designed wings, respectively.

*4.3.1.2 House Fly Wings.* Though house flies move their wings back and forth to achieve flight, the basic shape of their wings holds potential for a MEMS design. In fact, the shape of the house fly wings make them very durable. A set of house fly wings were designed with this durability and basic goal of flapping in mind. Like the dragonfly wings, the house fly wings were laid out in L-edit by tracing an actual fly wing using the poly2 and gold layers. Again, each wing was designed to allow for individual actuation but also simultaneous operation. Figure 4.4 is the design layout for the house fly wing system.

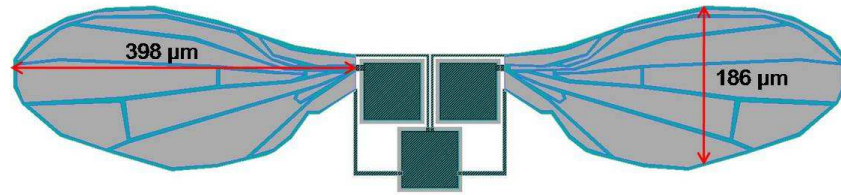


Figure 4.4: This graphic shows the bimorph wing design that emulates the common house fly.

Test wing structures with center actuation points were designed for the house fly wing separate from the full system. Two different size sets of wings were also developed for the same reasons as the different dragonfly size wings. The small set measured  $199\text{ }\mu\text{m}$  by  $93\text{ }\mu\text{m}$  and the large set measured  $398\text{ }\mu\text{m}$  by  $186\text{ }\mu\text{m}$ , span and chord lengths respectively. The large fly wing designs were 15 times smaller than the actual fly wing and the small wings were 30 times smaller. Therefore, the fly wing designs scaled much closer to the actual fly wings than the dragonfly wings did to their actual wings.

*4.3.1.3 Butterfly Wings.* Butterfly wings are more flexible in nature than either dragonfly wings or house fly wings. Butterflies also flap their wings slower than the previously mentioned insects. The different approach to flapping was the



reason for designing the butterfly wing. Although the wing design was constructed of poly2 and gold layers like the other two designs, the shape of the wing design allows for twisting as well as deflection when actuating. Again the wing design allows for individual wing activation, though the butterfly commonly flaps its wings in a synchronized manner. Figure 4.5 shows the L-edit layout of the butterfly wing design.

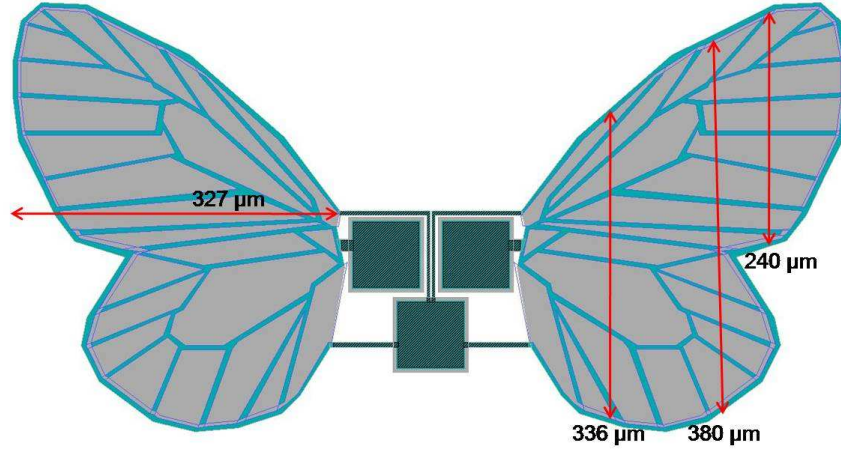


Figure 4.5: Bimorph wing design traced off of a graphic of actual butterfly wings.

In coordination with the butterfly wing design, test structures were designed for center actuation. Like the fly wing, two different size devices were designed to compare wing deflection vs wing size while holding all other factors the same. The small wing design measured  $163\text{ }\mu\text{m}$  for the span and an average of  $159\text{ }\mu\text{m}$  for the chord lengths measured at three different locations on the wing. The larger design measured  $327\text{ }\mu\text{m}$  for the span and  $319\text{ }\mu\text{m}$  for the average chord length measured at three different locations on the wing. The ratio of span to chord length is nearly unity for the butterfly wing. This makes the butterfly wing design distinctly different than the other two designs in which the span of the wing was at least twice that of the chord length. The designed wings were 184 and 92 times smaller than the actual butterfly wings for the small and large designed wings, respectively.

*4.3.2 Thermal Actuator Wings.* Mechanical designs were also created in order to see if they could outperform those inspired by nature. Two basic thermal

actuator schemes were designed for the activation of these mechanical wings. One design, groups ten double hot arm thermal actuators and links them together to provide actuation for the wing designs. It was possible to chain the actuators together by grounding the device through a breached nitride connection. This design was chosen to maximize the force while minimizing surface area for actuating the wings. In MUMPs® run 84, a second design of 8 chevron thermal actuators were chained together for even greater force output and less surface area consumption. Both devices were constructed of poly1-poly2 stacked layers to increase there strength. Figure 4.6 (a) shows the double hot arm actuation scheme and Figure 4.6 (b) shows the chevron actuation scheme.

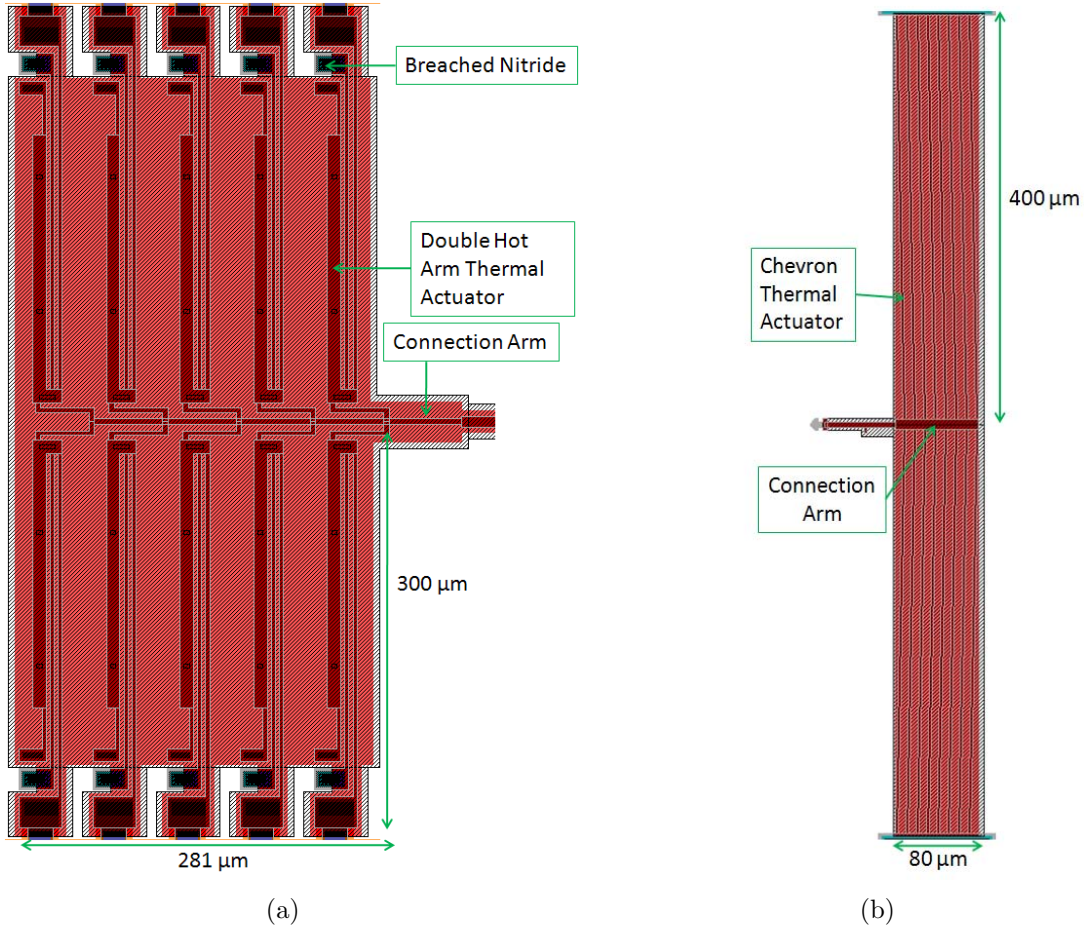


Figure 4.6: (a) 10 double hot arm actuators chained together for increased force (b) 8 chevron actuators chained together for greater force and potential deflection



*4.3.2.1 Assembly Wings.* The thermal actuators were again chained together with a stacked connection arm. The original design from MUMPs® run 82 had a rectangular cap at the end of the connection arm which was updated in run 84 to one with a point at the end. The pointed end allows for an easier connection into the latch of the wing. The same basic connector shape was used for each assembly wing design.

The basic wing shape was designed out of poly1 with hinges at the base to serve as the pivot point for the flapping wing. Brackets for the hinges were designed at each end of the wing to hold the wings pivot point at a fixed position. A rectangular hole near the base of the wing serves as the latch in which the connector point previously described interconnects. The small differences for these two assembly schemes other than size are etch holes, a poly0 layer, and dimples. The addition of these three features is necessary for wings that are not going to undergo the post processing back-side etch. If the device undergoes a backside etch, none of these three features are necessary. Figure 4.7 (a) shows the small size wing and Figure 4.7 (b) shows the larger wing.

Figure 4.8 shows a scanning electron microscope (SEM) image of added features that make the assembling of the wing structures easier. A tab connected to the hinge on one side and hovering over the cantilever beam on the other side was added to both sides of the design. The cantilever beams, constructed of poly2 and gold, naturally deflected upward after the structure was released due to their residual stress properties. Since the tab was connected on the hinge side but not the cantilever beam side, the hinge was forced to pivoted as the cantilever beams deflected. As the hinge pivoted, the end of the wing raised up off of the substrate allowing a probe to fit easier under the wing and complete the assemble of the connector arm with the latch.

MUMPs® run 84 added a pair of double hot arm actuators to make it easier to deflect the connection arm in the direction of the latch. The cantilever beams and

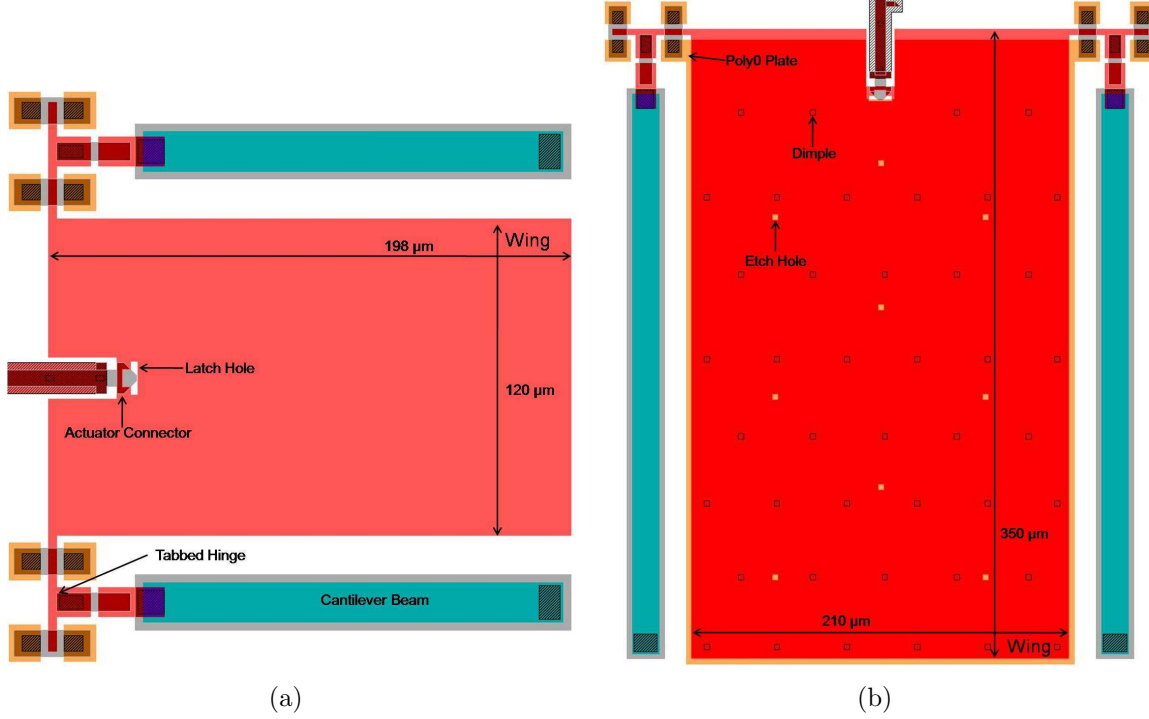


Figure 4.7: (a) Small wing with 198  $\mu\text{m}$  span and 120  $\mu\text{m}$  chord designed for a post processing back-side etch (b) Large wing with 350  $\mu\text{m}$  span and 210  $\mu\text{m}$  chord with a poly0 passivation layer, etch holes, and dimples to prevent stiction.

tab structures were also increased in size for this run. This means even greater initial deflection of the wing structure to aid in the assembly process.

**4.3.2.2 Connected Wings.** The basic premise of these wings is to create flapping motion with an out of plane deflection of the connecting arm. Activating the thermal actuators with an alternating current (AC) would cause the wing to rise and fall as the connector deflects out of plane. These wing designs are the same size as the small assembly wings.

One of the connected wing designs from MUMPs<sup>®</sup> run 82 had a single connection point. This single point connection was 21  $\mu\text{m}$  into the center of the wing from the base. This allowed for any generated motion to translate into greater deflection of the wing than if the connection were at the base. The design was further modified into two distinct designs in MUMPs<sup>®</sup> run 84. One change was to make the wing

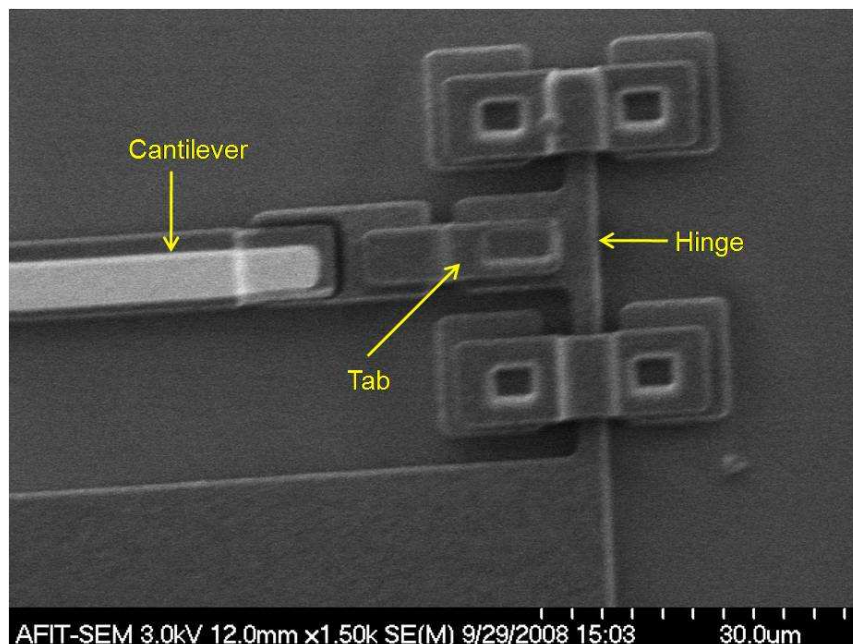


Figure 4.8: SEM graphic of components that aid in assembling the wing with its actuation scheme.

lighter by making it mostly out of poly2. Gold was also added to the wing to force a natural deflection. This deflection would ensure the connection point starts at an out of plane angle. The second improvement moved the connection further into the wing ( $42\text{ }\mu\text{m}$ ) for the same reason given previously and was incorporated into both updated designs. Single point connected wings from MUMPs<sup>®</sup> run 84 are shown in Figures 4.9 (a) and (b).

Another connected wing design from MUMPs<sup>®</sup> run 82 was a double connection wing. This double connector wing added a third hinge to the middle of the wing to ensure even force distribution from the pulling motion of the double connector. This design was no longer developed in future runs due to its inefficiency and to allow space for other more promising wing designs.

#### 4.4 Chapter Summary

This chapter discussed in detail how conceptual designs for this thesis were fabricated. A post processing technique was also discussed that would enhance the

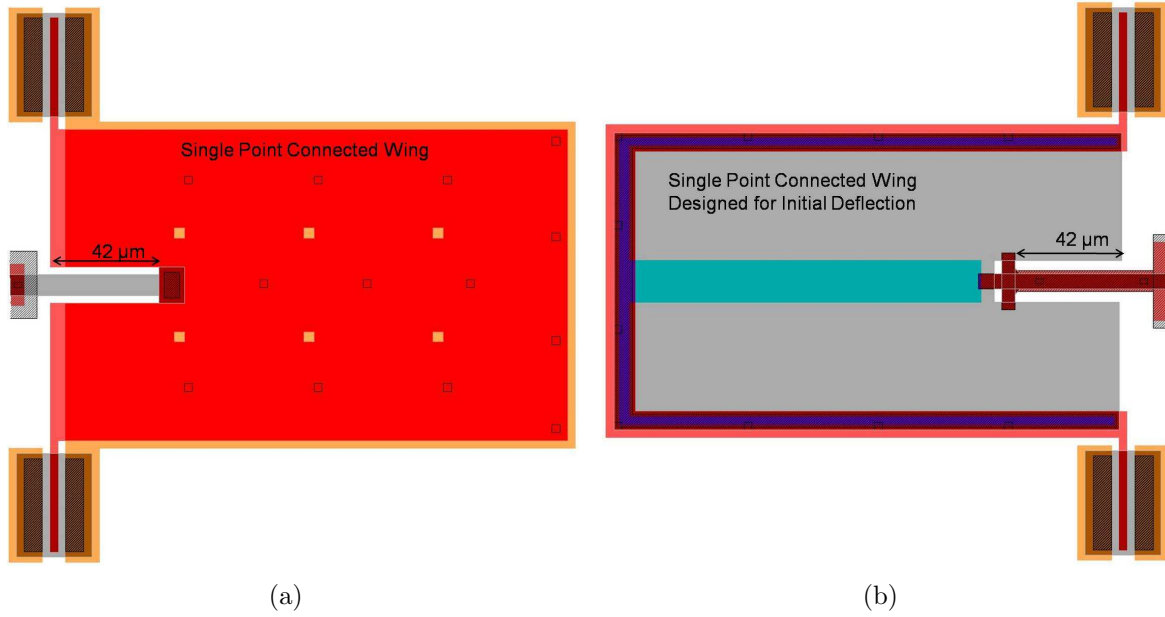


Figure 4.9: Single point connected wings (a) based off original run with connection pushed back to  $42\ \mu\text{m}$  and (b) lighter wing with added gold to cause natural deflection and forced out of plane connection point.

capability of the designs. Biologically inspired wings were designed as thermal bi-morph structures that would match their real life insect wing structures. Through iterative design techniques, these bio-wings had several design improvements to increase flapping performance. Other wings of a more mechanical nature were also designed. Thermal actuation schemes were discussed for both connected wing structures as well as wing structures requiring assembly. Methods to aid wing assembly were explored in this chapter as well. For a comprehensive review of all the wing and actuator designs, refer to the L-edit layouts in Appendix A. The next chapter will combine the designs of this chapter and the theory of Chapter 3 to model and simulate the wing behavior.

## V. Modeling and Simulation

### 5.1 Chapter Overview

This chapter presents the modeling and simulation results for many of the devices discussed in Chapter 4. Modeling was accomplished by importing the design layouts from L-edit into a finite element modeling software called CoventorWare®. Simulations on these models were conducted to predict the behavior of the designs prior to fabrication. Since little was known about how these dynamic shapes should preform, there was no analytical calculations to compare the simulated data to. The following sections take a closer look at the modeling software and simulated results for the different bio-wing designs.

### 5.2 CoventorWare®

CoventorWare® is an integrated suite of software tools for designing and simulating MEMS devices. The fabrication process and material properties database matching the user's designs (PolyMUMPs™ in this case) is the starting point of the modeling process. From here, the user can build a schematic of their MEMS device and simulate various aspects of its physical behavior. L-edit designs can also be imported into the layout editor which will convert the designs into a 3-D solid model. Before generating a mesh of the model, labels can be assigned to various features of the model to be used later during simulation. The model is then meshed and the user may choose from a suite of field solvers to simulate the physical behavior of their device [64].

### 5.3 Modeled Designs

Several designs from MUMPs® runs 83 and 84 were successfully modeled. An example of a meshed, center actuated, dragonfly forewing from run 83 is shown in Figure 5.1. The bio-wing designs were modeled using the parabolic tetrahedrons mesh setting in the 3-D modeler. The dragonfly, house fly, and butterfly wings were all modeled using an element size of six. Input and output points at the base of

the wing structures were labeled in the model for center, leading, and trailing edge activation schemes that correspond to the test structures from Chapter 4. The next section focuses on the simulated results.

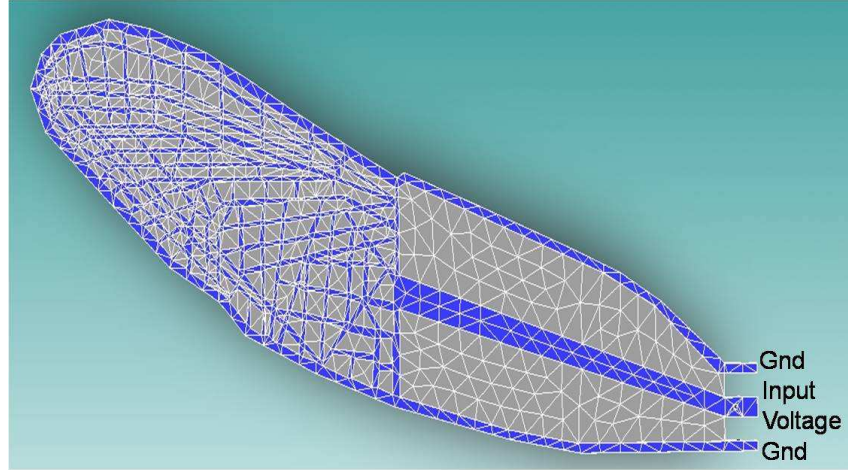


Figure 5.1: Graphic of a center actuated dragonfly forewing meshed and labeled for simulation.

#### 5.4 *Run 83 Simulated Results*

The first round of simulations occurred for the bio-wings of MUMPs® run 83. The 372 by 94  $\mu\text{m}$  dragonfly forewing and 388 by 122  $\mu\text{m}$  back wing designs were simulated for leading edge, center, and trailing edge activation. The 330 by 319  $\mu\text{m}$  butterfly and 398 by 186  $\mu\text{m}$  house fly wings were simulated with center activation only because the center actuated simulations of the dragonfly wings had much better deflection results than actuating either edge. Parametric studies were setup for each wing's activation scheme with the input voltage varying from 0-20 volts in 2.5 volt increments. The simulation parameters for the large dragonfly wings were redefined to 0.5-10 volts with 0.5 volt increments in order to get simulation results from CoventorWare®. The software failed to run any of the large dragonfly wing simulations starting at 0 volts and the maximum voltage was known to be less on the larger scale wings so that parameter was also reduced from the original value. Results from each wing assembly scheme are discussed individually in the following sections.

5.4.1 *Dragonfly.* Figure 5.2 (a) shows the design setup of the dragonfly forewing and Figure 5.2 (c) shows the design setup of the dragonfly back wing both with leading edge activation. Figure 5.2 (b) and Figure 5.2 (d) show the simulated results at 12.5 volts of applied bias for the fore and back wings respectively. Based on the simulated results, the temperature and stress in the devices would destroy the devices above the 12.5 volt bias. Therefore, the expected maximum deflection should occur between 10-12.5 volts resulting in 17-27  $\mu\text{m}$  of deflection in the forewing and 15-23  $\mu\text{m}$  of deflection in the back wing. For trailing edge activation, the input and ground points of Figure 5.2 (a) and Figure 5.2 (c) would be switched. The simulated results of the trailing edge activation scheme match those of the respective leading edge fore and hind wings.

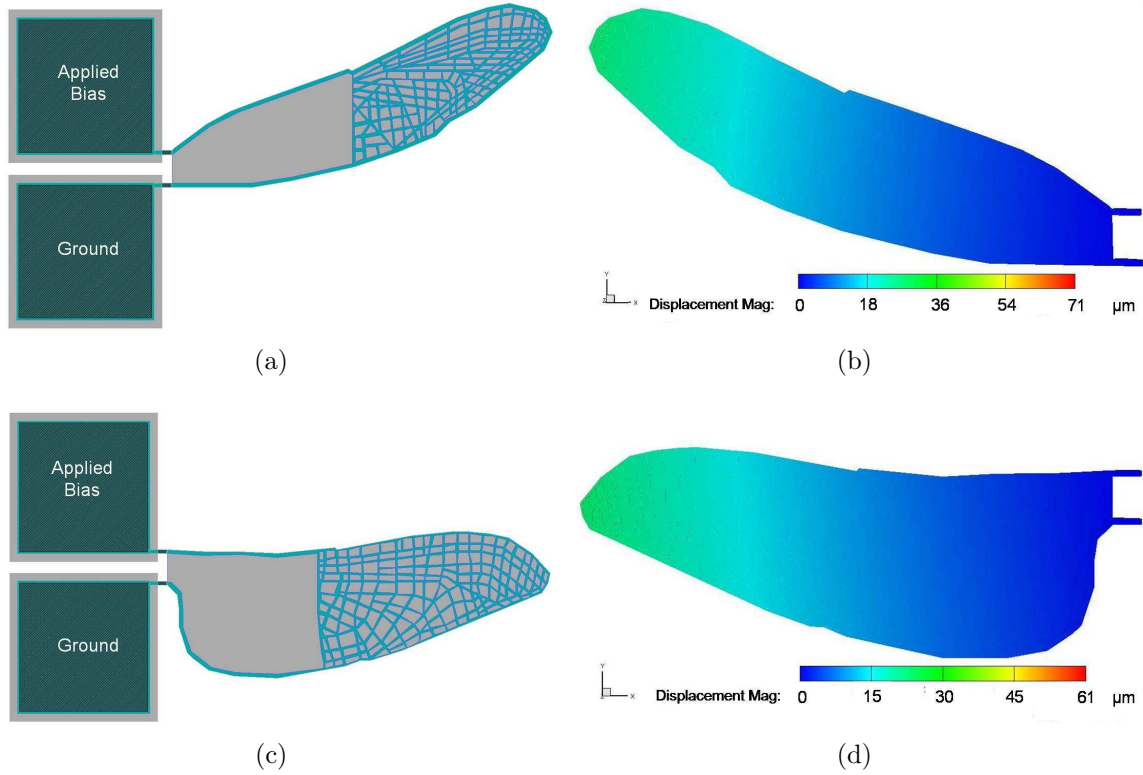


Figure 5.2: (a) Test structure design for 186 by 45  $\mu\text{m}$  leading edge simulation of dragonfly forewing (b) Simulated forewing deflection at 12.5 volts applied bias (c) Test structure design for 194 by 60  $\mu\text{m}$  leading edge simulation of dragonfly back wing (d) Simulated back wing deflection at 12.5 volts applied bias. Both simulations produced a maximum 27  $\mu\text{m}$  deflection.

Figure 5.3 (c) shows the design setup for the center actuated fore and back dragonfly wings. Due to temperature and stress limitations, the 186 by 45  $\mu\text{m}$  center actuated dragonfly fore and 194 by 60  $\mu\text{m}$  back wings failed above 12.5 volts bias. The expected maximum deflections of these device occurred between 10-12.5 volts resulting in 115-170  $\mu\text{m}$  and 121-180  $\mu\text{m}$  of deflection, respectively. Figure 5.3 (a) shows the simulated results for the 186 by 45  $\mu\text{m}$  center actuated forewing at 12.5 volts of applied bias. The corresponding 372 by 94  $\mu\text{m}$  forewing, which is twice the size of the small one, had limitations of stress and temperature occurring at 6.5-8 volts and 5.5-6.5 volts, respectively. Therefore, a maximum deflection range of 152-225  $\mu\text{m}$  corresponds to the lower limiting voltage range. Figure 5.3 (b) shows the simulated results of the 194 by 60  $\mu\text{m}$ , center actuated back wing at 12.5 volts. The corresponding 388 by 122  $\mu\text{m}$  back wing was also simulated for center activation with a resulting maximum deflection range of 131-203  $\mu\text{m}$ . This corresponds to a voltage limitation of 5.5-6.5 volts.

One result from these simulations is the fact that center actuation provides better deflection than either the leading or trailing edge activation. It was also determined that anchors had to be added near the base of the wing to prevent the entire actuation lines from deflecting. This change forces the wing to deflect without losing deflection to the actuation lines. The designs shown in this section were redesigned from their originals to reflect this necessity. The simulations also indicate a need to remove the substrate and nitride layers if the wings are going to reach their full deflection potential. Simulated data also suggests not only that these devices operate at low voltage, but that it is essential for their survival. This was because the gold expanded much quicker than the polysilicon. After a few volts of applied bias, the gold began to heat much quicker than attached polysilicon would allow it to expand leading to device damage or destruction.

*5.4.2 Fly.* Since the simulations for the dragonfly wings showed the greatest deflection potential under center activation, the fly wing designs were only simulated



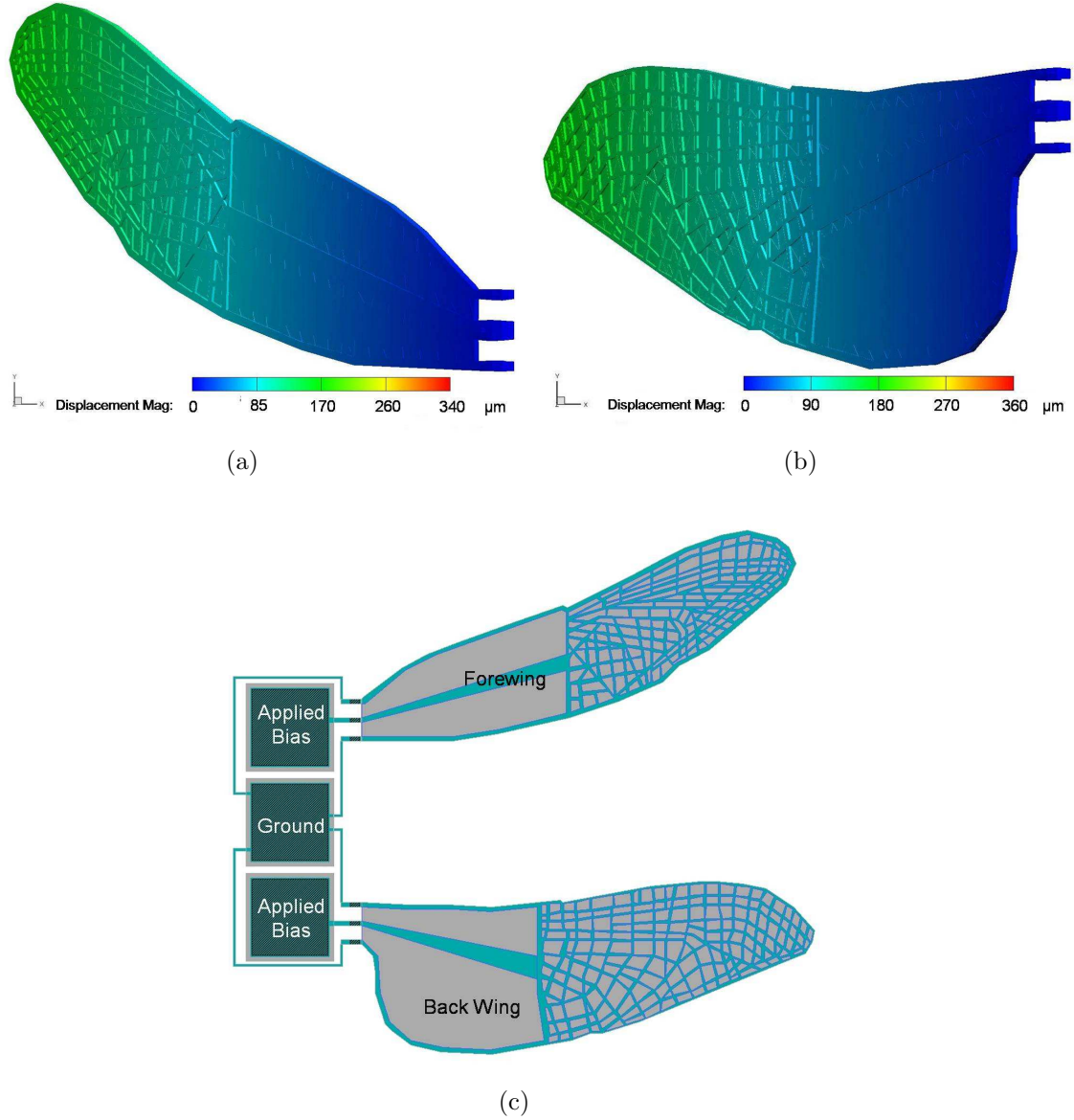


Figure 5.3: Simulations run at 12.5 volts of applied bias on (a) 186 by 45  $\mu\text{m}$ , center actuated dragonfly forewing and (b) 194 by 60  $\mu\text{m}$ , center actuated dragonfly back wing. These small forewing and back wing simulations yielded a maximum deflection of 170  $\mu\text{m}$  and 180  $\mu\text{m}$ , respectively. (c) Center actuated dragonfly wing designs.

for center activation as shown in Figure 5.4 (c). The simulation on the 398 by 186  $\mu\text{m}$  wing design only ran through 17.5 volts indicating catastrophic device failure at this voltage level. Figure 5.4 (a) shows this large fly wing at 7.5 volt applied bias. The wing became significantly effected above 7.5 volts in terms of handling any additional heat without failing. In order for the wing to operate as intended, the device should

operate in the maximum 5-7.5 volt range which corresponds to a 91-303  $\mu\text{m}$  deflection. Figure 5.4 (b) depicts the 199 by 93  $\mu\text{m}$  fly wing under 12.5 volts of applied bias. Limitations on this small wing force the device into a 10-12.5 operational voltage range which corresponds to a 63-94  $\mu\text{m}$  deflection.

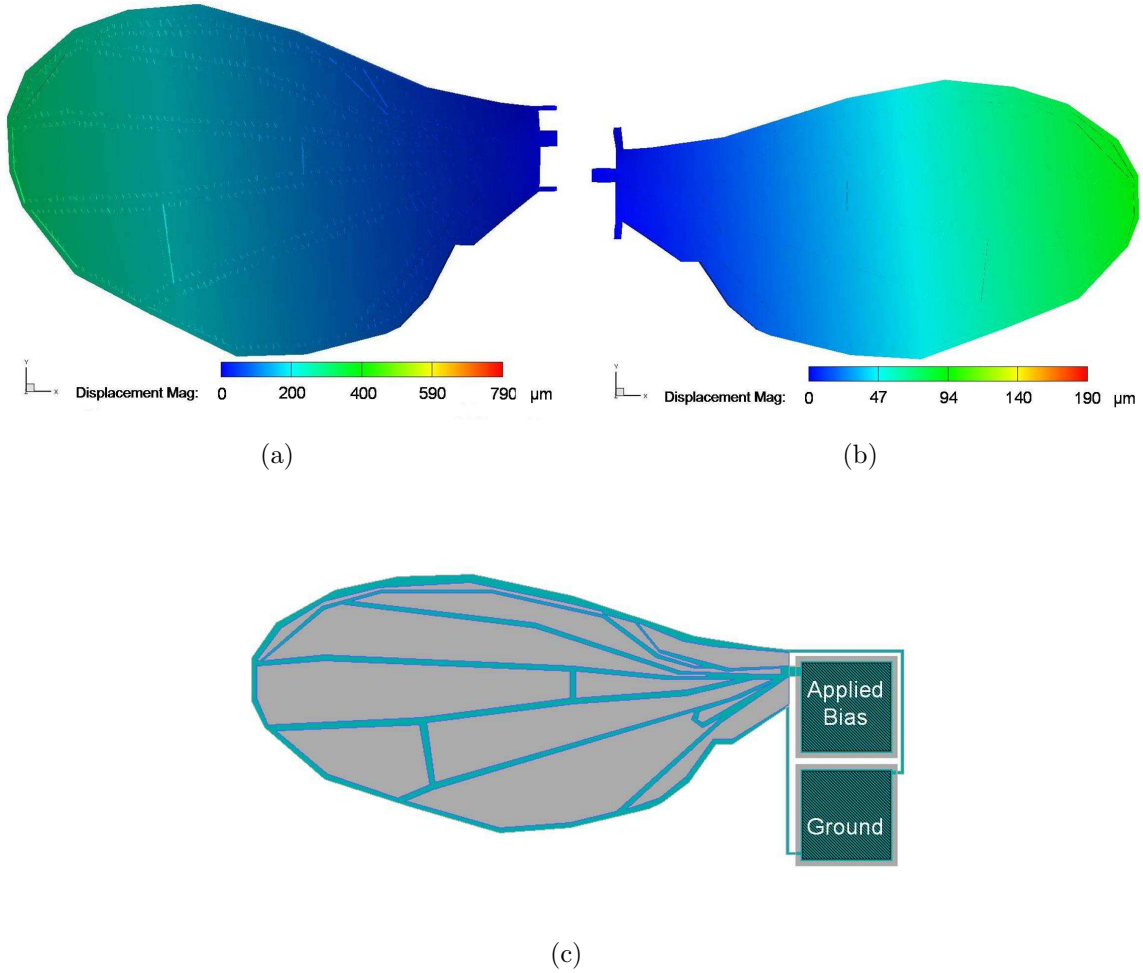


Figure 5.4: (a) Simulated 398 by 186  $\mu\text{m}$  fly wing under 7.5 volts of applied bias (b) 199 by 93  $\mu\text{m}$  fly wing simulated under 12.5 volts of applied bias. Simulated maximum deflection of 303  $\mu\text{m}$  for the large wing and 94  $\mu\text{m}$  for the small wing. (c) Test fly wing layout with labeled simulation activation scheme

The fly wing simulations produced mainly the same type of deflection as the dragonfly wing simulations. This resulted in the same design upgrades mentioned for the dragonfly wings. Note also that the large fly wing gets greater deflection results at

a lower voltage than the small wing. This is beneficial in terms of maximum deflection but limits the device in terms of stress it is capable of handling before device failure.

*5.4.3 Butterfly.* Like the fly wing, the butterfly wing was only tested under the center activation scheme seen in Figure 5.5 (c). Figure 5.5 (a) shows the resultant maximum 330 by 319  $\mu\text{m}$  butterfly wing deflection at 7.5 volts. This simulation showed total device failure after 12.5 volts and didn't run the remaining three increments of the parametric study. The stress of the structure was able to handle the 7.5-10 volt range, but the temperature limitations took over in the 5-7.5 volt range. Therefore, the maximum deflection observed for this large butterfly wing simulation fell between 93-282  $\mu\text{m}$ . Figure 5.5 (b) is the simulated deflection graphic of the 163 by 159  $\mu\text{m}$  butterfly wing at 10 volts. This small device also failed to run after the 12.5 volt increment. The limitations for this device fell in the 7.5-10 volt range for both the stress and temperature for a corresponding 105-162  $\mu\text{m}$  deflection. Temperature limitations indicated that any additional temperature would melt the gold of the device. Stress limitations indicated that any further deflection in the wing would cause the connections at the base to deform if not break.

The butterfly wing design was no exception in terms of adding required anchors to the design and removing the substrate. However, the simulated results of the butterfly wing show significant difference to the fly and dragonfly simulations. It is clear in Figure 5.5 (a) and Figure 5.5 (b) that the butterfly wing doesn't only deflect in the direction of the substrate when heated but also twists as indicated by the yellow coloration. This twisting occurred because the top half of the wing deflected more than the bottom half of the wing. Like the fly wings, the larger butterfly wings get better deflection than the smaller ones but cannot handle as much voltage as the smaller device. This is most likely due to increased heating in the additional gold of the larger structure.

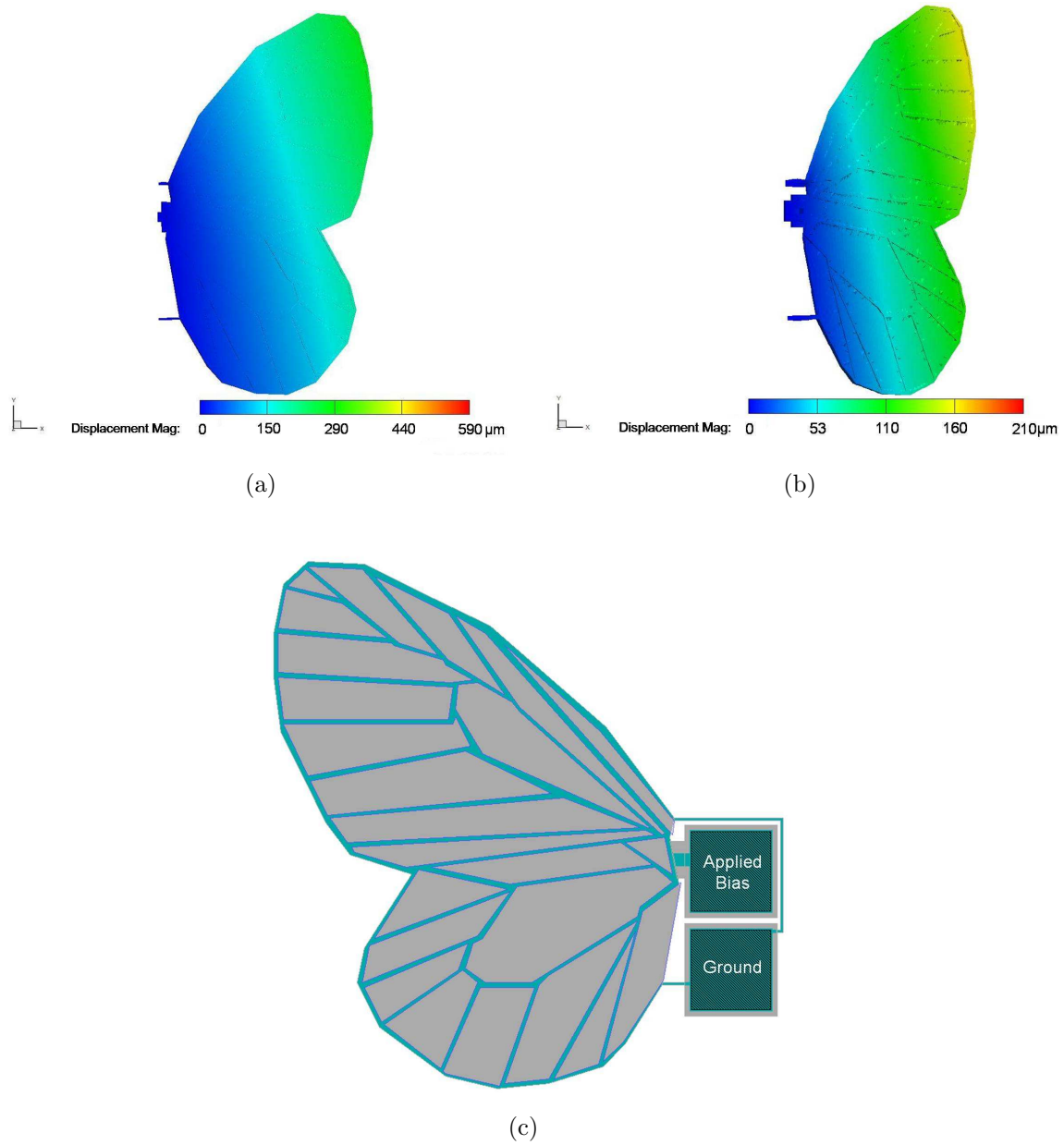


Figure 5.5: (a) Simulated results for the 330 by 319  $\mu\text{m}$  butterfly wing under 7.5 volts of applied bias corresponding to 282  $\mu\text{m}$  maximum deflection (b) Simulated results of the 163 by 159  $\mu\text{m}$  butterfly wing under 10 volts of bias corresponding to 162  $\mu\text{m}$  maximum deflection. (c) Test wing layout for the butterfly wing design

### 5.5 Run 84 Simulated Results

Experimental results lead to additional design changes from MUMPs<sup>®</sup> run 83. The entire actuation and ground lines were attached to the substrate to provide a

better heat sink for the lines. The available current paths on the wing structures were also altered to force the current further out into the tip of the wings. The basic shapes of the wings were preserved as well as the wing veins (gold layer). However, a new set of center actuated dragonfly wings with a complete vein structure were also introduced. Parametric studies were setup for each wing's activation scheme with input voltages varying from 0-14 volts in 2 volt increments. With the exception of the 398 by 186  $\mu\text{m}$  fly wing, the large wing simulation parameters were changed in order to get a successful simulation. The remaining large wing simulations of run 84 were run from 0.5-10 volts with incremental increases of 0.5 volts. Results from each wing assembly scheme are discussed individually in the following sections.

*5.5.1 Dragonfly Wings.* Figure 5.6 (a) shows both the fore and back dragonfly wing designs setup for center actuation with extended current path. Figure 5.6 (b) shows a new design for the dragonfly fore and back wings with labeled activation scheme. This wing design was added to include the entire vein structure of a dragonfly wing. Current flow was forced out into the tip of the wings by controlling the path of least resistance in both wing types. The large dragonfly wings were setup exactly like the smaller ones.

The first set of simulations were run on the wings shown in Figure 5.6 (a). Both the forewing device and the back wing device break down in the 8-10 volt range. The expected maximum deflection range of 125-199  $\mu\text{m}$  for the forewing device shown in Figure 5.7 (a) corresponds to the voltage range of 8-10 volts. Figure 5.7 (b) shows the simulated results of the back wing at 10 volts with a maximum deflection range of 52-77  $\mu\text{m}$ . The 372 by 94  $\mu\text{m}$  and 388 by 122  $\mu\text{m}$  dragonfly wings with extended current path yielded deflection ranges of 63-81  $\mu\text{m}$  and 74-90  $\mu\text{m}$  for the fore and back wings, respectively. These deflections were limited in the voltage range of 5.5-6.5 volts for both the fore and back wings.

Simulations were also run for the wing structures of Figure 5.6 (b). The simulated results for the entire 186 by 45  $\mu\text{m}$  forewing structure are shown in Figure 5.8 (a)

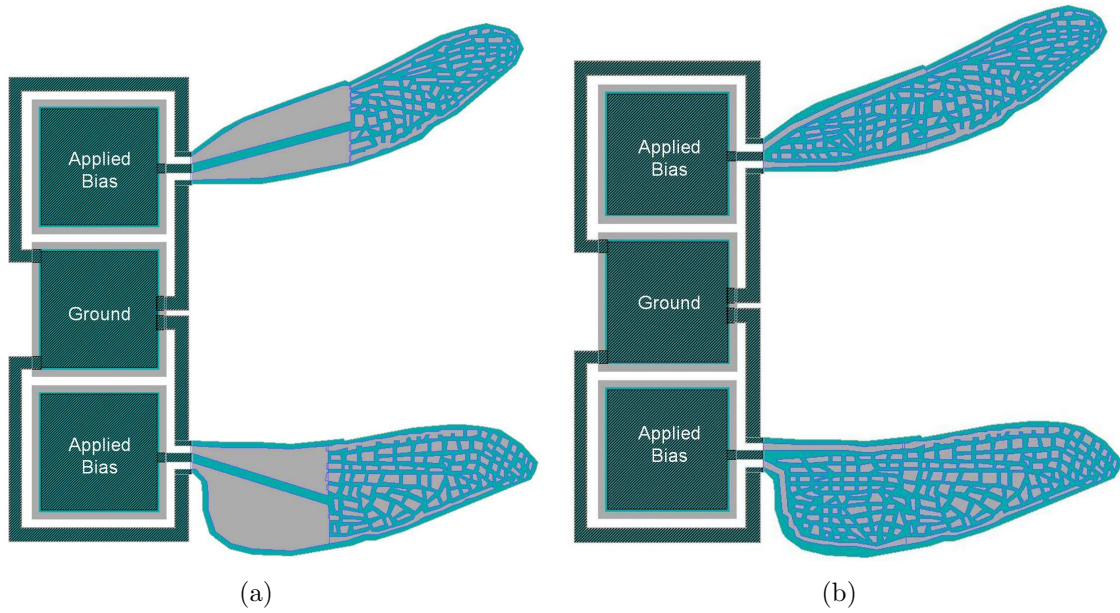


Figure 5.6: (a) Test structure layout for 186 by 45  $\mu\text{m}$ , center actuated fore and 194 by 60  $\mu\text{m}$  back dragonfly wings with extended current path, forcing current out into the tip of the wing. (b) Test structure layout for the same size dragonfly wings with entire vein structure and extended current path.

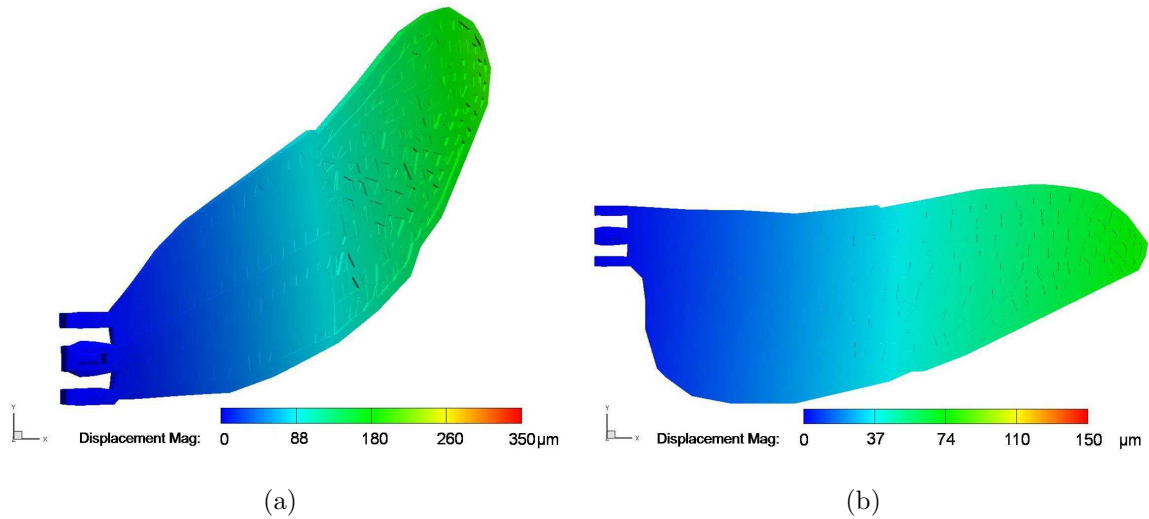


Figure 5.7: Simulations run at 10 volts of applied bias on (a) 186 by 45  $\mu\text{m}$  center actuated dragonfly forewing and (b) 194 by 60  $\mu\text{m}$  center actuated dragonfly back wing with extended current path. The maximum deflection for the forewing and back wing of these simulations are 199  $\mu\text{m}$  and 77  $\mu\text{m}$ , respectively.

and the simulated results for the entire 194 by 60  $\mu\text{m}$  back wing structure are shown in Figure 5.8 (b). Limitations of this small forewing device occurred in the 8-10 volt range for temperature and stress while the back wing was temperature limited by the 6-8 volt range. The resulting maximum deflection range of 111-178  $\mu\text{m}$  transpired for the full 186 by 45  $\mu\text{m}$  forewing structure and 65-109  $\mu\text{m}$  for the full 194 by 60  $\mu\text{m}$  back wing structure. The simulation for the large wings, which were twice the size of these small wings with the entire vein structure, failed completely for voltages greater than 8.5 volts. Voltage range limitations of the large wings occurred at 5-6.5 volts for the forewing and 5-6 volts for the back wing which proceeds the 8.5 volt catastrophic failure point where the simulation no longer ran. The catastrophic failure was most likely either the wings snapping due to stress or the gold melting off the wing due to excessive temperature. The corresponding deflection ranges were 90-99  $\mu\text{m}$  and 104-114  $\mu\text{m}$ , respectively.

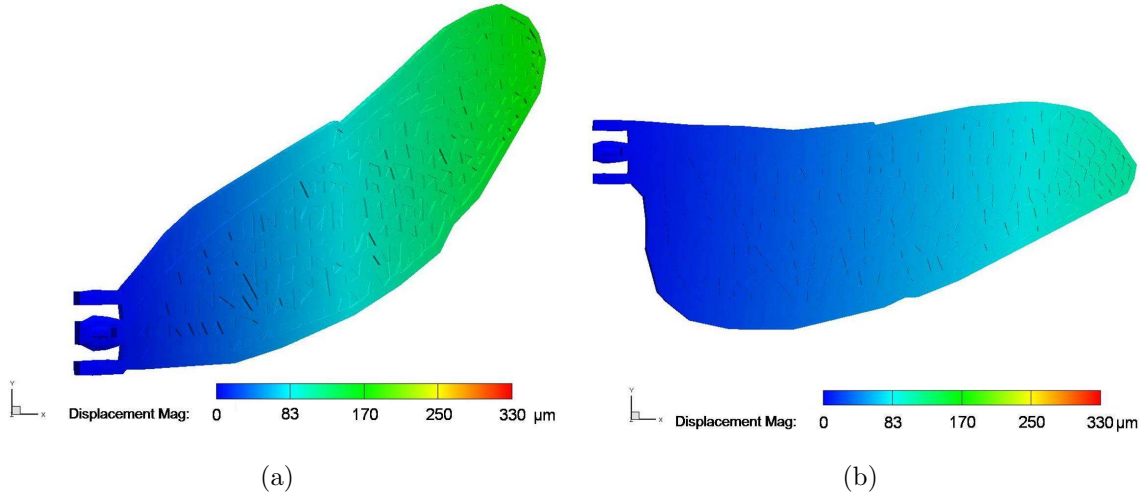


Figure 5.8: Simulations run at (a) 10 volts of applied bias on the center actuated forewing with complete vein structure corresponding to 178  $\mu\text{m}$  maximum deflection and (b) 8 volts of applied bias on the complete center actuated back wing with corresponding 109  $\mu\text{m}$  maximum deflection.

Table 5.1 compares all the simulated data for the dragonfly wings. In run 83, the small and large center activated wings had approximately the same deflection range; however, the large wings obtained the deflection with about half the voltage. The 186



by 45  $\mu\text{m}$  forewings of run 84 also had approximately the same deflection range as the forewings of run 83. The 372 by 94  $\mu\text{m}$  forewings of run 84 deflected significantly less than both the small wings of run 84 and the forewings of run 83. One explanation for this is greater heat dissipation in the wing due to the extended current path. The 194 by 60  $\mu\text{m}$  back wings of run 84 averaged only half the deflection of the same size, run 83 back wings, but deflection was more uniform across the entire wing as opposed to at the tip in run 83. The same phenomena held true when comparing the large back wings of the two runs. One thing that the simulated data concluded for all of the wing designs was that the nitride and substrate layers beneath the wings must be removed for the wings to reach their deflection potential.

Table 5.1: This table summarizes the different deflection ranges and the voltage ranges for which they occur.

<b>Comparison of Simulated Dragonfly Wings</b>			
<b>Wing Actuation Scheme</b>	<b>MUMPs<sup>®</sup> Run</b>	<b>Deflection Range (<math>\mu\text{m}</math>)</b>	<b>Voltage Range (V)</b>
Leading Edge Forewing	83	17-27	10-12.5
Trailing Edge Forewing	83	17-27	10-12.5
Leading Edge Back Wing	83	15-23	10-12.5
Trailing Edge Back Wing	83	15-23	10-12.5
Small Center Forewing	83	115-170	10-12.5
Small Center Back Wing	83	121-180	10-12.5
Large Center Forewing	83	152-225	5.5-6.5
Large Center Back Wing	83	131-203	5.5-6.5
Small Extended Center Forewing	84	125-199	8-10
Small Extended Center Back Wing	84	52-77	8-10
Large Extended Center Forewing	84	63-81	5.5-6.5
Large Extended Center Back Wing	84	74-90	5.5-6.5
Entire Small Vein Forewing	84	111-178	8-10
Entire Small Vein Back Wing	84	65-109	6-8
Entire Large Vein Forewing	84	90-99	5-6.5
Entire Large Vein Back Wing	84	104-114	5-6

*5.5.2 Fly Wings.* Figure 5.9 (a) shows the updated fly wing design with extended current path. The current path was extended to force current flow all the



way out into the tip of the wing. This will help to determine if an extended current path would increase the flapping performance of the fly wings.

The fly wing becomes significantly effected between 8-10 volts from a temperature standpoint and 10-12 volts in terms of stress. Therefore, the device should operate in the maximum 8-10 volt range which corresponds to a 40-59  $\mu\text{m}$  deflection. Figure 5.9 (b) shows the fly wing at 10 volts applied bias.

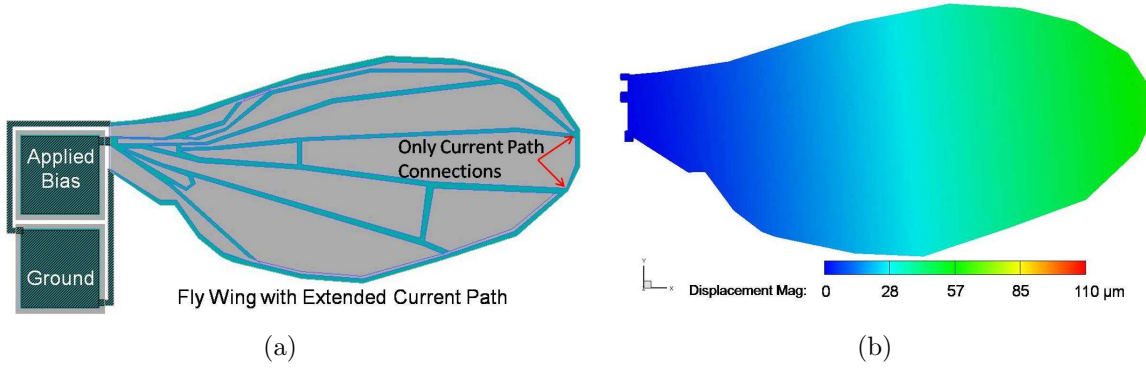


Figure 5.9: (a) Test fly wing with extended current path and labeled simulation activation scheme (b) Simulated 398 by 186  $\mu\text{m}$  fly wing with extended current path under 10 volts of applied bias yielding a maximum deflection of 59  $\mu\text{m}$ .

The 199 by 93  $\mu\text{m}$  fly wing with extended current path was accidentally omitted from the MUMPs® 84 run so no simulation was done for this small wing. Simulated data of run 84 compared to the run 83 simulations showed that the extended current path significantly reduces the expected deflection in the 398 by 186  $\mu\text{m}$  fly wing. In fact, the run 84 wing design actually deflected less than the same size wing of run 83. Since the current path was shorter in run 83, greater total deflection occurred in the wing. By forcing the current over the entire span of the wing in run 84, heat dissipated more uniformly which resulted in less total deflection. Table 5.2 compares the simulated data of the three different simulated fly wings.

*5.5.3 Butterfly Wings.* The 163 by 159  $\mu\text{m}$  butterfly wings with an extended current path were accidentally omitted from the MUMPs® 84 run but the equivalent large wing design (2 times the size of the smaller wing) of Figure 5.10 (a) was not.

Table 5.2: This table summarizes the different center actuated fly wing simulations.

Comparison of Simulated Fly Wings			
Wing Structures	MUMPs® Run	Deflection Range ( $\mu\text{m}$ )	Voltage Range (V)
Large Fly Wing	83	91-303	5-7.5
Small Fly Wing	83	63-94	10-12.5
Extended Path Large Fly Wing	84	40-59	8-10

A simulation was setup for the extended current path 330 by 319  $\mu\text{m}$  butterfly wing from 0.5-10 volts with voltage increments of 0.5 volts. Simulated results show temperature limitations in the 5-6 volt range and stress limitations in the 5.5-6.5 volt range. Therefore, the limiting voltage range was 5-6 volts which corresponded to a deflection range of 18-24  $\mu\text{m}$ . Figure 5.10 (b) shows the butterfly wing at 6 volts of applied bias.

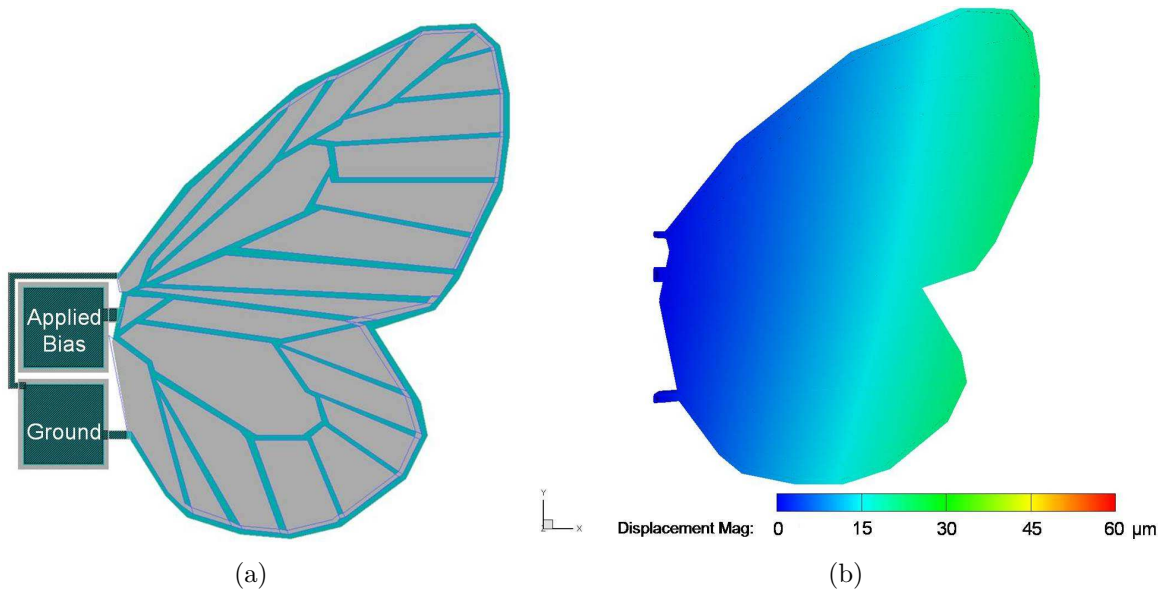


Figure 5.10: (a) Test butterfly wing with extended current path (b) Simulated 330 by 319  $\mu\text{m}$  butterfly wing with extended current path under 6 volts of applied bias yielding a maximum deflection of 24  $\mu\text{m}$ .

Table 5.3 compares the simulated data from the various butterfly simulations. The extended path butterfly wing of run 84 produced significantly less deflection than

either of the two designs from run 83. This was again attributed to more uniform heating in run 84 opposed to the greater heating near the base of the wing in the run 83 designs. Another noteworthy point about the 330 by 319  $\mu\text{m}$  extended path wing design was that the top and bottom half of the wing appear to deflect more evenly than the run 83 wings. This eliminated the twisting during flapping which was unique to the butterfly wings. The extended butterfly design lost both twist and deflection range rendering it an inferior design to those of run 83 according to the simulations.

Table 5.3: This table summarizes the different center actuated butterfly wing simulations.

<b>Comparison of Simulated Fly Wings</b>			
<b>Wing Structures</b>	<b>MUMPs<sup>®</sup> Run</b>	<b>Deflection Range (<math>\mu\text{m}</math>)</b>	<b>Voltage Range (V)</b>
Small Butterfly Wing	83	105-162	7.5-10
Large Butterfly Wing	83	93-282	5-7.5
Extended Large Butterfly Wing	84	18-24	5-6

## 5.6 Chapter Summary

This chapter discussed CoventorWare<sup>®</sup>, the modeling tool that allowed testing of the MEMS designs before fabrication. Many simulations were run, providing valuable insight into which wing designs had the greatest potential for advancing MEMS flapping capability. This iterative process of design, model, and simulation aided in the prevention of many design errors prior to fabrication. The next chapter will focus on taking these refined designs and testing them experimentally.

## VI. Experimental and Analytical Results

### 6.1 Chapter Overview

This chapter presents experimental results for the rectangular and bio-wing designs. This chapter delves into the assembly of the rectangular wings with their respective actuation schemes and discusses data on the deflections. Connected rectangular wings utilizing thermal actuation are also a topic of this chapter. The bio-wings were experimentally measured for deflection and compared to simulated results. Analytical analysis was performed to provide insight into aerodynamic properties of MEMS size devices.

### 6.2 Assembly Wings

Figure 6.1 shows the key components of the assembly wing structure. The designed assembly aids cause the wing to deflect up 8-12  $\mu\text{m}$ , allowing a probe to easily fit underneath the wing. A probe was used in trying to complete the wing assembly by lifting the wing until the connection arm of the actuators snapped into the latch of the wing. Experimentally, the wing assembly was unable to connect the actuators with the wing because the rectangular connector did not fit into the latch on the wing. Though the wing was not assembled, the experiment showed that the hinges and initial deflection of the wing due to the cantilevers both worked as designed. In addition to the assembly aids working well, the group of thermal actuators also worked as designed. Further work into the assembly wing designs was suspended due to the success of the bio-wings flapping.

### 6.3 Connected Wings

MUMPs<sup>®</sup> run 82 had two different connected wing designs, the double arm connection and the single arm connection. Both of the designs were linked to ten double hot arm actuators for activation. The double hot arm actuators were activated with an AC sine wave signal at a ten hertz frequency offset with a 10-12 volt direct current (DC). Under these conditions, the double connection arm broke at the points

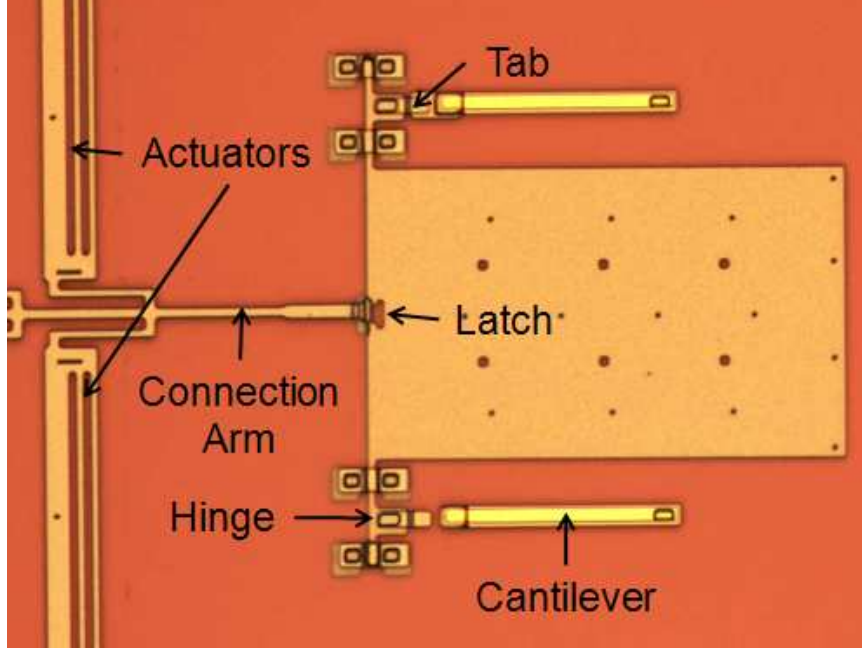


Figure 6.1: 198 by 120  $\mu\text{m}$  assembly wing with key components labeled.

were the connections turned toward the wing structure as shown in Figure 6.2 (a). The single arm connection had good structural strength but was unable to force the wing structure to deflect out of plane. However, one hinge point broke and the wing began to oscillate back and forth instead of up and down. The oscillating wing occurred within a 6.8-11.3 volt DC offset range, 10 hertz frequency, and 6.1-9.7 volts peak-to-peak AC signal range. Figure 6.2 (b) shows the single point connection wing at the broken hinge point.

#### 6.4 *Bio-Wings*

A multitude of different biology inspired wings were released and tested experimentally. The first tests run on the wings were done under straight DC bias and deflections were measured from the wing base to the wing tip using the Zygo® interferometer microscope (IFM). Larger sized wings were measured using either the 40  $\mu\text{m}$  or 100  $\mu\text{m}$  scan and the smaller wing designs were measured using either the 20  $\mu\text{m}$  or 40  $\mu\text{m}$  scan to capture the entire wing deflection. The voltage was increased in increments of 0.1 volts until each device failed or reached its deflection limit. The

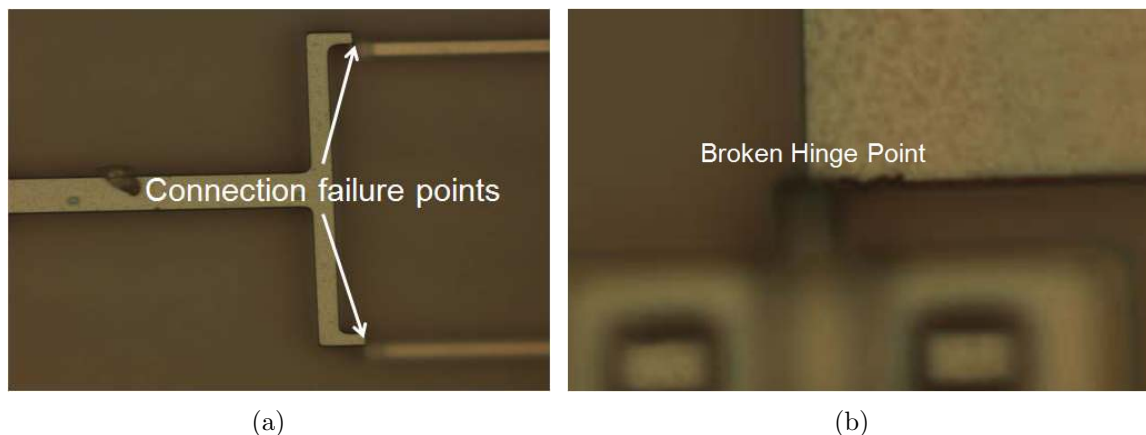


Figure 6.2: (a) Double connection wing with labeled location of connecting arms breaking point (b) Single arm connected wing in back and forth oscillation contrary to desired up and down motion of the wing due to the broken hinge point pictured.

initial deflections, caused by the residual stress, were measured without applying a voltage bias. Final deflection measurements were taken at the last voltage increment before device failure. Figure 6.3 shows the most common cause of device failure in run 83, ground lines burning out. Other device failures included reduced deflection under increasing bias and unstable wing movement under a constant DC bias. The most common limitation in the run 84 devices was contact with the substrate.

Each bio-wing design was also tested for optimal flapping frequency. The designs were placed under a microscope with an attached camera to view the wing as it flapped. Each wing was then connected to an AC voltage source with a 10 Hz sine wave. Voltages on the wings were increased in 0.25 volt increments until the wing began to move. Once the wing began moving, the frequency was altered in 10 Hz increments between 10-80 Hz until the largest amount of wing surface area appeared to flap. After the optimal frequency was determined, the next voltage increment was applied. This process continued until the test devices failed. A frequency value was recorded at each voltage increment and these values (10-27 data points) were averaged to provide one optimal flapping frequency for each wing design.

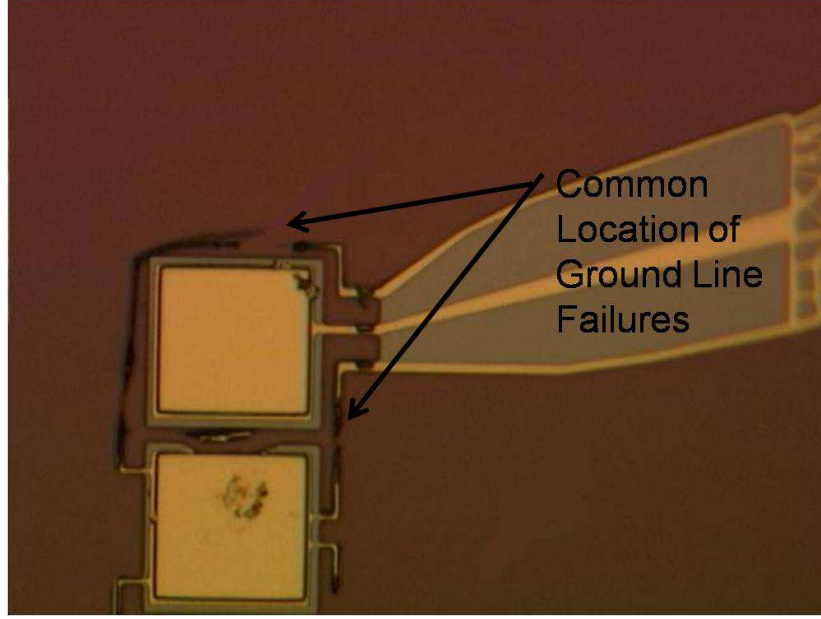


Figure 6.3: This graphic shows the common location for device failure in the majority of the bio-wing designs.

*6.4.1 Dragonfly Experimental Results.* The first measurements were performed on the  $186 \times 45 \mu\text{m}$  dragonfly forewings of run 83. Figure 6.4 (a) shows a top view of the small forewing's initial deflection measurements and Figure 6.4 (b) shows conceptually how the bio-wing structures behave in general as additional voltage is applied. Leading edge activation was capable of handling a greater voltage than the center activation scheme but less deflection was observed in the leading edge wing. The simulated results for the leading edge activation had a maximum voltage range of 10-12.5 volts and a maximum deflection range from  $17\text{-}27 \mu\text{m}$ . Simulated results for the center activation were 10-12.5 volts and  $115\text{-}170 \mu\text{m}$  for maximum voltage and deflection ranges respectfully. The experimental results showed only  $2.91 \mu\text{m}$  deflection for the leading edge at 4 volts and  $4.55 \mu\text{m}$  deflection for the center actuation at 1.5 volts. Therefore, both the leading edge and center activations fell short of their simulated maximum ranges. The voltage was unable to reach its maximum value due to ground line failures which in turn resulted in smaller deflections than the simulations. However, the simulated deflection of the center actuated wing at 2.5 volts (closest simulated value to the experimental data) was  $9.25 \mu\text{m}$ . This indicates the

device is functioning similar to the simulated data but may not produce deflections as large as the simulated data. In the case of the leading edge activation, the simulated deflection at 4 volts was expected to be  $5\text{ }\mu\text{m}$  which exceeds the experimental values at 4 volts by several microns. The average frequency for this small dragonfly forewing was 39.26 Hz.

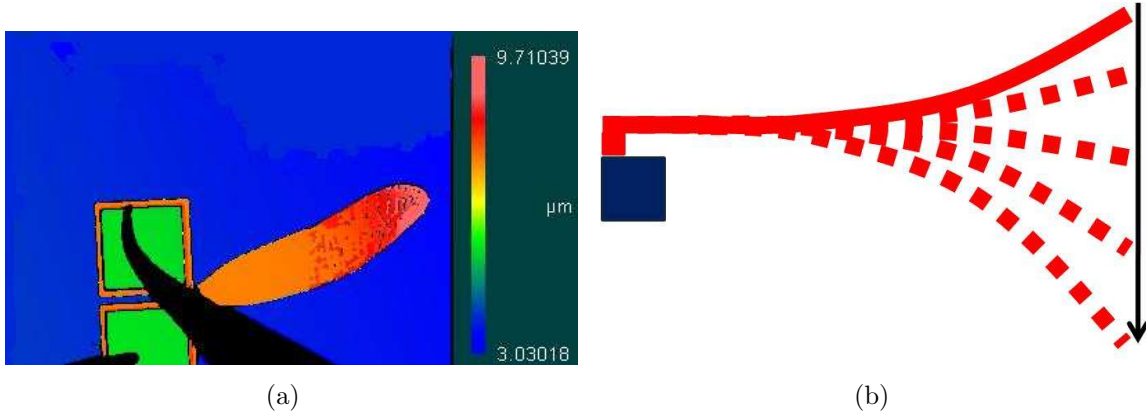


Figure 6.4: (a) Experimental plot results measured using the Zygo® interferometer which shows deflection across the entire wing (b) Conceptual profile of bio-wings with blue box representing the substrate, solid red line indicating initial deflection, dashed lines representing wing under increasing applied bias, and black arrow showing the deflection direction as the voltage increases.

Experimental data on the  $194\text{ by }60\text{ }\mu\text{m}$  back wings of run 83 was variable, dependent on the activation scheme designed for the wings. The maximum voltages and total deflections were again short of the simulated data for each activation scheme. For the leading and trailing edge activations, the maximum simulated voltage and deflection values were 10-12.5 volts and  $15\text{-}23\text{ }\mu\text{m}$ , respectfully. For the center activation scheme, 10-12.5 volts and  $121\text{-}180\text{ }\mu\text{m}$  were the maximum simulated ranges. The experimental results for the leading edge activation were  $2.905\text{ }\mu\text{m}$  of deflection at 1.5 volts and the center activation results were  $1.985\text{ }\mu\text{m}$  of deflection at 2.25 volts. In the leading edge simulation at 2.5 volts, the deflection was only  $1.282\text{ }\mu\text{m}$  which is less than the experimental results. Simulated data for the center actuated small back wing showed a  $9.629\text{ }\mu\text{m}$  deflection at 2.5 volts which was much greater than the experimental values. Though the experimental results continued to show deflection



toward the substrate with increasing voltage, the small back wing does not follow a similar trend to the simulated data seen in the small forewing. The flapping frequency of this small back wing averaged 30 Hz.

The 372 by 94  $\mu\text{m}$ , center actuated, dragonfly forewings of run 83 were tested next. These larger wings experienced both greater initial deflection as well as larger deflection range. The large forewing appears to get greater deflection at less voltage when compared to that of the smaller forewing. The maximum simulated deflection range for this set of wings was 152-225  $\mu\text{m}$  with a maximum voltage range of 5.5-6.5 volts. The experimental results for this wing showed 8.047  $\mu\text{m}$  of deflection at 1.25 volts. The simulation from 1-1.5 volts produced a simulated deflection of 6.262-11.660  $\mu\text{m}$ . Therefore, the experimental results are consistent with the simulated results. The average frequency for these large forewings was 39.17 Hz.

Experimental data was next collected for the 388 by 122  $\mu\text{m}$ , center actuated back dragonfly wings of run 83. In these large back wings, the initial deflections varied but the total deflection of each tested wing was within 1  $\mu\text{m}$  of each other. Likewise, the total voltage the wings were capable of handling was never more than 0.6 volts difference. As the applied voltage increased, the wings continued to deflect further which supports the theory that greater voltages will yield greater deflections in the wings. The maximum simulated voltage and deflection ranges for this set of wings was 5.5-6.5 volts and 131-203  $\mu\text{m}$ , respectively. The experimental deflection and voltage values were 2.987  $\mu\text{m}$  and 1.488 volts respectively. For the simulated results between 1-1.5 volts, the wings deflected 6.324-12.136  $\mu\text{m}$  which is greater than the experimental results. The average frequency of these large back wings was 31.67 Hz.

Figure 6.5 shows a 372 by 94  $\mu\text{m}$  forewing with the entire dragonfly vein structure represented. Both this large wing and a small wing, half the size of the larger one, were tested for this design scheme of run 84. Simulated results indicated a maximum deflection range of 111-178  $\mu\text{m}$  and 90-99  $\mu\text{m}$  for the small and large wings, respectively. The corresponding maximum voltage ranges were 8-10 and 5-6.5 volts

respectively. These simulated results are surprising because typically the larger wings are expected to have greater deflection. The experimental deflection for the 372 by 94  $\mu\text{m}$  wing was 28.955  $\mu\text{m}$  at 1.567 volts and the experimental deflection for the 186 by 45  $\mu\text{m}$  wing was 9.131  $\mu\text{m}$  at 1.6 volts. Therefore, the experimental results did show that the larger wings experience greater deflection than their smaller counterparts. Though the experimental data showed significantly less deflection than the simulated results, these wings were an improvement over those of run 83. The entire small vein forewing had almost three times greater deflection than the run 83 small forewing while the entire large vein forewing saw an improvement greater than four times that of the run 83 large forewing. Another important thing to note is that one of the tested devices actually reached its deflection limit by contacting the substrate. This supports removing the substrate and nitride layers beneath the wings so that the wings can reach full deflection potential.

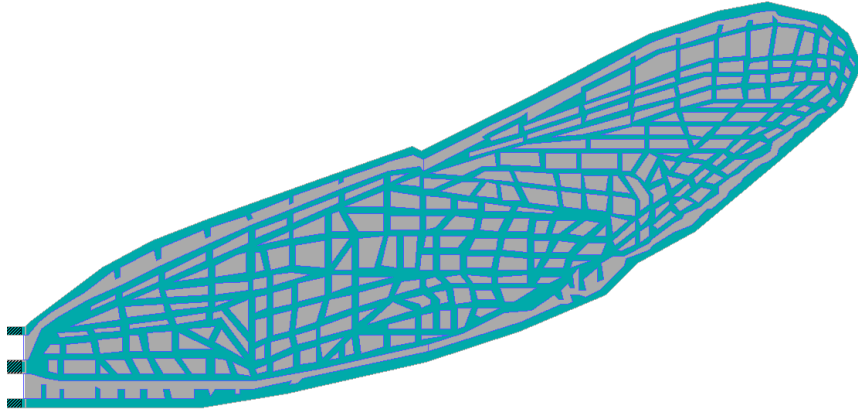


Figure 6.5: Extended current path with entire dragonfly vein structure present in the wing design.

Optimal operating frequency of this large forewing with entire vein structure was calculated by averaging 14 experimentally collected frequencies taken at incremental voltage levels on two different wings. One of these test wings did not begin to flap until part of the devices actuation lines overheated which was indicated by its discoloration. The resulting optimal operating frequency for the large entire vein forewing was 52.86 Hz. The smaller entire vein forewing was averaged from 13 col-

lected frequency values on two different wings. The optimal frequency for this small wing averaged out to be 40.77 Hz.

Device limitations in these new wings did not commonly come in the form of ground line burn out as in run 83. The most common limitation in run 84 was deflection into the substrate. This limitation can be alleviated by substrate and nitride layer removal. Another common failure was leveling off of deflection. This leveling off occurred when increasing bias no longer resulted in additional deflection. Two potential reasons could explain this leveling phenomena. One reason could be that the joule heating began to deform the wing in more than just the desired direction preventing any further deflection. Another reason could be that the polysilicon layer supporting the gold would no longer support further gold expansion due to its much slower rate of expansion. No immediate solution is known to prevent this problem from occurring.

Dragonfly back wings with entire vein structure were tested next. Simulations indicated that the 186 by 45  $\mu\text{m}$  and 372 by 94  $\mu\text{m}$  wings from this experiment should deflect 65-109  $\mu\text{m}$  and 104-114  $\mu\text{m}$  at maximum voltage ranges of 6-8 volts and 5-6 volts, respectively. Experimentally the smaller wing deflected 9.682  $\mu\text{m}$  at 1.533 volts and the larger wing deflected 20.139  $\mu\text{m}$  at 1.6 volts. Therefore, these devices failed to reach the voltage levels of the simulations and also the maximum deflection ranges. However, the device performance again exceeded that of the previous run designs in terms of deflection. The small wing with entire veins improved total deflection by nearly five times while the large wing with entire vein structure saw nearly seven times greater deflection than the large wing of run 83. This improved deflection occurred at maximum voltages that were nearly the same as those of the previously run dragonfly back wings. The experimental data again indicated contact with the substrate in the case of one tested wing meaning a backside etch was required beneath the wings to prevent limiting their deflection.

Two 186 by 45  $\mu\text{m}$  entire vein back wings were tested at voltages from 0.5-2 volts at 0.25 volt intervals yielding 14 experimental frequency values. These values were averaged to provide the optimal flapping frequency of the entire small vein back wing which was 32.86 Hz. The entire 372 by 94  $\mu\text{m}$  vein back wings were tested under the same conditions and produced an average flapping frequency of 48.57 Hz.

Another problem that the experiments brought to life was the plastic deformation of the wings. Once the final deflection measurements were taken, the bias voltage on the wings was removed. This resulted in an increase in the unbiased deflection of the wing and prevented the wing from deflecting as far when the bias was applied to the wing again. Much like a rubber band that has been stretched so far that it can never go back to its original shape, wings operated near or at their maximum voltage likewise lose elasticity in their gold layer. Figure 6.6 (a) shows a pre-bias wing's initial deflection and Figure 6.6 (b) shows the same wing after the experimental bias was removed. This plastic deformation may lead to a potential reliability issue when operating the wings near their maximum deflection voltage.

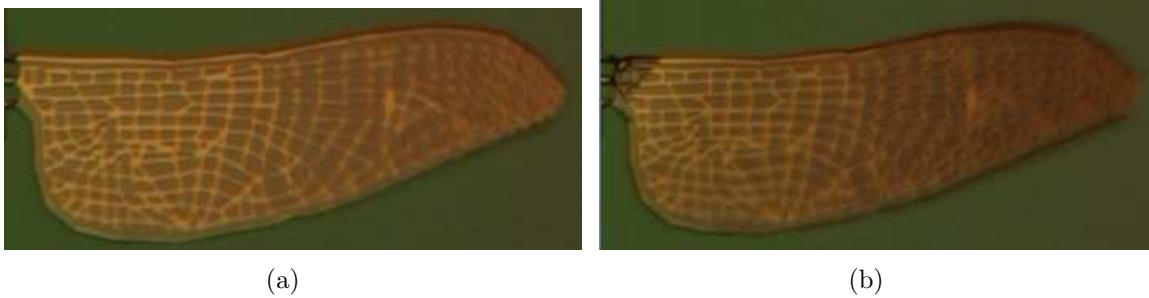


Figure 6.6: (a) Entire vein back wing before any applied bias, initial deflection of 32.753  $\mu\text{m}$ . (b) Same wing after experimental testing of two volts applied bias was removed. The no bias deflection of the wing after the experimental testing resulted in a 58  $\mu\text{m}$  deflection. The result of this deformation of the wing structure lead to reduced deflection range of the wing when voltage was again applied.

The next four dragonfly wing designs match those of run 83 except the ground lines have been anchored to the substrate and the current path was extended out into the tip of the wing. The 186 by 45  $\mu\text{m}$  fore and 194 by 60  $\mu\text{m}$  back wings had simulated deflection ranges of 125-199  $\mu\text{m}$  and 52-77  $\mu\text{m}$  respectively with a

corresponding maximum voltage range of 8-10 volts for both. Experimentally, the three tested forewings averaged  $7.543\ \mu\text{m}$  and 1.467 volts while the three tested back wings averaged  $7.489\ \mu\text{m}$  and 1.467 volts. All six of these small wings reached the deflection limit of the substrate, confirming the need to remove the substrate and nitride beneath the small extended path wings. In addition, each of these small extended path fore and back wings were on target to exceed or already exceeded the simulated deflection of  $9.074\ \mu\text{m}$  and  $4.969\ \mu\text{m}$  respectively at 2 volts of bias.

Simulated deflection ranges for the  $372\ \text{by}\ 94\ \mu\text{m}$  fore and  $388\ \text{by}\ 122\ \mu\text{m}$  back extended path wings were  $63\text{-}81\ \mu\text{m}$  and  $74\text{-}90\ \mu\text{m}$ , respectively. Both deflection ranges corresponded to a maximum voltage range of 5.5-6.5 volts. The actual large forewing deflected an average of  $19.858\ \mu\text{m}$  at 1.633 volts and the actual large back wing deflected an average of  $17.82\ \mu\text{m}$  at 1.6 volts. Clearly the results fall short of the maximum deflection ranges and only one of the six large wings tested had reached the substrate limit. However, the large extended path forewing deflects nearly three times more than the large forewing of run 83 and the large extended path back wing deflects almost six times more than the large back wing of run 83. This increase in deflection occurred at approximately 0.1 volts greater bias than the previous run's bias. Though the experimental data suggests that the simulations were overly ambitious, the data did show a progression of the flapping wing technology over that of the previous wing attempts.

Both the small extended path fore and back wings were experimentally tested to find their optimal flapping frequency. Those experiments yielded 13 and 14 frequency values, respectively. The average flapping frequency for the small extended path fore and back wings were 46.92 Hz and 42.86 Hz, respectively. The optimal frequency of the large extended path forewing, averaged over 14 experimentally collected frequencies from two wings, was 49.29 Hz. The optimal frequency for the large extended path back wing was 51.54 Hz and it was averaged from 13 collected data points from two different test wings. One of the test wings for each of the large extended path wings had to heat up to the point of discoloration before the wings began to flap.

Table 6.1 is a summary of each of the different types of dragonfly wings from runs 83 and 84. The table averages at least three and as many as eight data points for each individual dragonfly wing type tested. This averaging provided a single deflection and voltage value for each type of dragonfly wing. It is clear from the table that the larger wings get better initial deflection than their smaller counter parts and the same holds true for total deflection. The table also clearly shows that the run 84 dragonfly wings significantly out perform the same size wings of run 83.

Table 6.1: This table provides the type of dragonfly wing, MUMPs® Run, average initial deflection, average total deflection and average maximum voltage for each dragonfly wing.

<b>Summary of Experimental Results for the Dragonfly Wings</b>				
<b>Wing Type</b>	<b>Run</b>	<b>Average Initial Deflection (<math>\mu\text{m}</math>)</b>	<b>Average Total Deflection (<math>\mu\text{m}</math>)</b>	<b>Average Maximum Voltage</b>
Center Actuated Small Forewing	83	4.760	4.550	1.500
Leading Edge Small Forewing	83	2.625	2.910	4.000
Large Forewing	83	16.832	6.768	1.490
Center Actuated Small Back Wing	83	3.035	1.985	2.250
Leading Edge Small Back Wing	83	7.050	2.905	1.500
Large Back Wing	83	12.400	2.987	1.488
Entire Vein Small Forewing	84	9.523	9.131	1.600
Entire Vein Large Forewing	84	35.686	28.955	1.567
Entire Vein Small Back Wing	84	10.408	9.682	1.533
Entire Vein Large Back Wing	84	29.638	20.139	1.600
Extended Path Small Forewing	84	4.793	7.543	1.467
Extended Path Large Forewing	84	24.028	19.858	1.633
Extended Path Small Back Wing	84	4.739	7.489	1.467
Extended Path Large Back Wing	84	21.467	17.820	1.600

*6.4.2 House Fly Experimental Results.* The 199 by 93  $\mu\text{m}$ , center actuated house fly wing design of run 83 was able to handle higher voltage values of 5-6 volts before the ground lines burnt out. However, experimental results showed that this small house fly wing's deflection was much less than the other small dragonfly wings. These greater voltage values did not translate into larger deflection values because the

ground lines began flapping at around 2 volts. This resulting ground line deflection almost completely stopped the deflection in the wing structure itself (device failure). The simulated maximum ranges for the small house fly wings were 10-12.5 volts and 63-94  $\mu\text{m}$  deflection. As a result of ground line flapping in the three small wings tested, the average total deflection was only 0.716  $\mu\text{m}$ . If the ground lines had not started to deflect, the small house fly wing most likely would have been on the simulated target of 3.821  $\mu\text{m}$  for 2.5 volts of applied bias. The average flapping frequency for this wing was 40 Hz.

The next set of house fly wings tested were the 398 by 186  $\mu\text{m}$ , center actuated wings of run 83. Only one of the three large house fly wings experienced the same ground line deflection as the smaller house fly wings. The deflection in the other tested wings behaved as expected with increased voltage yielding greater deflection in the wings. The maximum simulated voltage range and deflection values were 5-7.5 volts and 91-303  $\mu\text{m}$ , respectively. Experimentally, the wings averaged 4.403  $\mu\text{m}$  of deflection with a maximum voltage of 1.406 volts. The measured deflections were on track to meet the simulated deflection value of 19.635  $\mu\text{m}$  at 2.5 volts. This demonstrates great promise for the house fly wing once the ground lines are anchored to the substrate in MUMPs® run 84. These wings flapped optimally at an average frequency of 29.23 Hz.

Two different types of 398 by 186  $\mu\text{m}$  house fly wing designs from run 84, one just like the run 83 large house fly wing with anchored ground lines and one with anchored ground lines and an extended current path, were tested under DC bias to measure deflection. Simulated results for the regular large house fly wing had a maximum deflection range of 91-303  $\mu\text{m}$  for a maximum voltage range of 5-7.5 volts. Experimental measurements were taken on three regular large house fly wings with the average resulting deflection being 15.493  $\mu\text{m}$  at an average maximum voltage of 2 volts. Just like in the case of the run 83 large house fly wing, these large house fly wings did not reach the full deflection or voltage potential. However, with the ground lines anchored, the maximum voltage increased by 0.6 volts yielding an

increase in deflection of over  $11\text{ }\mu\text{m}$ . The simulation on the extended path large house fly wing had a larger voltage range of 8-10 volts but a smaller deflection range of 40-59  $\mu\text{m}$ . For each experimentally tested extended path house fly wing, the maximum possible deflection corresponding to substrate contact was achieved for an average total deflection of  $16.091\text{ }\mu\text{m}$  at an average 1.867 volts maximum voltage. At 2 volts, the simulation indicated only a  $6.373\text{ }\mu\text{m}$  deflection; therefore, the actual deflection performance of the wings was nearly  $10\text{ }\mu\text{m}$  more than expected at approximately 0.1 volts less of the applied bias. In order to see if the actual device would continue to out perform the simulation, the substrate and nitride layers must be removed.

Both of these large house fly designs were tested to determine their optimal flapping frequency. Thirteen frequency values were collected for the regular large house fly design which produced a frequency of 59.23 Hz when averaged. The large house fly with extended current path had one more collected frequency value which produced an average frequency of 51.43 Hz.

Table 6.2 provides a summary of each of the different types of house fly wings from runs 83 and 84. The table averages at least three and as many as nine data points for each individual house fly wing type tested. This averaging provided a single deflection and voltage value for each type of house fly wing. It is clear from the table that the larger wings get better initial deflection than their smaller counterparts and the same holds true for total deflection. The table also clearly shows that the run 84 house fly wings significantly out perform the same size wings from run 83. Anchoring the lines in the large house fly wing of run 84 reduced the initial deflection by about  $6\text{ }\mu\text{m}$  from the previous run, but the resulting total deflection was more than 3 times greater. Note also that the regular large house fly wing of run 84 had greater initial deflection than the extended path large house fly wing but each of the tested extended path wings deflected into the substrate yielding a greater total deflection than the regular wing. Once the substrate and nitride layers are removed, the total deflection could become even greater.



Table 6.2: This table provides the type of house fly wing, MUMPs® Run, average initial deflection, average total deflection and average maximum voltage for each type of house fly wing.

<b>Summary of Experimental Results for the House Fly Wings</b>				
<b>Wing Type</b>	<b>Run</b>	<b>Average Initial Deflection (<math>\mu\text{m}</math>)</b>	<b>Average Total Deflection (<math>\mu\text{m}</math>)</b>	<b>Average Maximum Voltage</b>
Small Wing	83	6.329	0.716	1.813
Large Wing	83	27.577	4.403	1.406
Extended Path Large Wing	84	13.341	16.091	1.867
Regular Large Wing	84	21.539	15.493	2.000

*6.4.3 Butterfly Experimental Results.* Different butterfly wing designs were the final type of bio-wings tested. Figure 6.7 illustrates how measurements were taking experimentally on the butterfly wings to obtain the maximum deflection. The first butterfly wing tested was the 163 by 159  $\mu\text{m}$  wing of run 83 which had a maximum simulated voltage and deflection range of 7.5-10 volts and 105-162  $\mu\text{m}$ , respectively. Three wings were tested resulting in an average total deflection of 1.548  $\mu\text{m}$  at an average maximum voltage of 1.25 volts. The experimental results seemed on track to come close to the simulated deflection value of 6.253  $\mu\text{m}$  at 2.5 volts. The frequency for the small butterfly wing was only 14 Hz which is less than all other previously tested bio-wings. However, butterflies in nature flap their wings less than both flies and dragonflies.

The 330 by 319  $\mu\text{m}$  butterfly wings of run 83 were the next set of tested butterfly wings. The simulated maximum voltage and deflection ranges for the large butterfly wing are 5-7.5 volts and 93-282  $\mu\text{m}$ , respectively. The average tested deflection and voltage of the these three large butterfly wings were 3.347  $\mu\text{m}$  and 1.458 volts, respectively. At 2.5 volts, the simulation predicted a 9.92  $\mu\text{m}$  deflection; therefore, the actual results seemed on target to meet that deflection if the ground lines had not failed. The average frequency for this wing was 35.24 Hz.

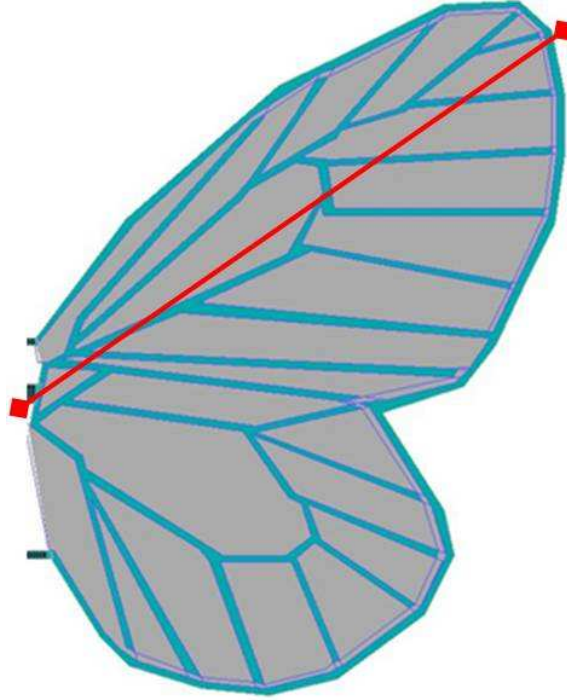


Figure 6.7: The maximum deflection in the butterfly wing occurs in the top half of the wing. The red line in the graphic shows the experimental location from base to tip in which the deflection measurements were obtained experimentally.

The butterfly wing designs were unique in their deflection because they did not just flap straight up and down like the other two wing designs. Figure 6.8 (a) shows an IFM profile plot of the top and bottom portions of the butterfly wing. Since the top half of the wing deflected more than the bottom half, a twisting motion occurred in the flapping of the butterfly wings. Figure 6.8 (b) shows deflection measurements taken on a large butterfly wing highlighting the difference in deflection across the wing. The initial deflection in the top half of the wing was  $16.178 \mu\text{m}$  while the bottom of the wing deflected only  $8.319 \mu\text{m}$ . As voltage was increased, the top of the wing deflected more than the bottom. Measuring the top and bottom of the wing just prior to device failure yielded a total deflection of  $2.638 \mu\text{m}$  and  $1.747 \mu\text{m}$ , respectively. If the voltage were able to continue increasing, than the twisting in the butterfly wing would also increase. This twisting phenomena in the butterfly wing was also seen in the simulation of the butterfly wing.

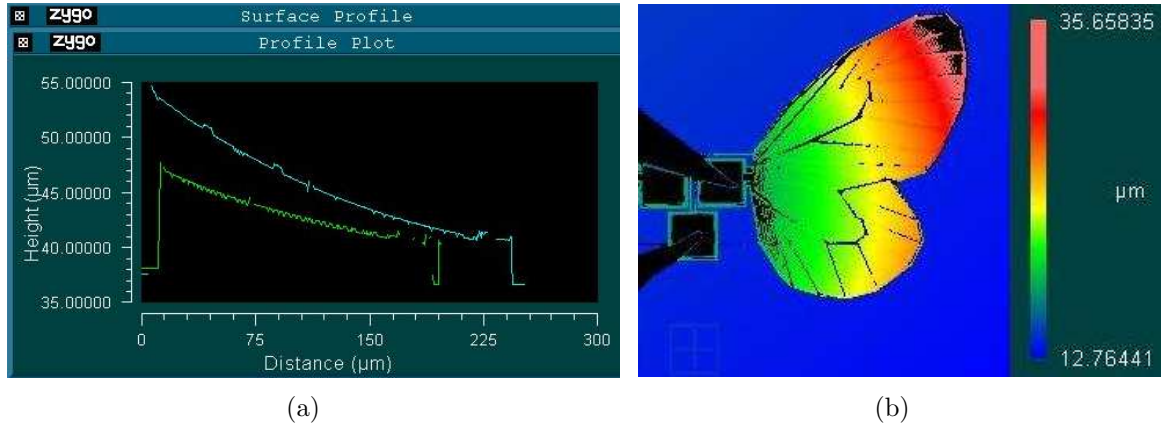


Figure 6.8: (a) IFM profile plot measuring the deflection in the top and bottom portions of the wing from the tip to the base. The blue line represents the top portion and the green line represents the bottom portion of the wing clearly showing a larger deflection in the top portion of the wing. (b) Graphical representation of deflection variation across the butterfly wing. As voltage was increased, the amount of deflection in the top half was greater than the bottom resulting in a twisting of the wing.

Two types of 330 by 319  $\mu\text{m}$  butterfly wing designs, one with anchored ground lines and the other with anchored ground lines and an extended current path, were also tested. Simulated data on the regular large butterfly wing indicated maximum deflection range of 93-282  $\mu\text{m}$  for a voltage range of 5-7.5 volts. Figure 6.9 shows experimental results of this wing type contacting the substrate. An average deflection of 16.881  $\mu\text{m}$  and maximum voltage of 2.067 volts resulted from the three tested regular large butterfly wings. At 2.5 volts the simulation predicted only 11.87  $\mu\text{m}$  deflection, so the experimental results produced about 5  $\mu\text{m}$  more deflection at a half volt less bias. This design also deflected over 13  $\mu\text{m}$  more than the run 83 large butterfly wing at only a half volt more bias. The large extended path butterfly simulation results yielded a small deflection range of 18-24  $\mu\text{m}$  at 5-6 volts of bias; however, the three tested large extended path butterfly wings average 15.665  $\mu\text{m}$  of deflection at an average maximum voltage of 1.867 volts. Each of these extended path butterfly wings deflected into the substrate. This extended path design deflected about 1  $\mu\text{m}$  less than the regular butterfly wing but the regular butterfly wing had better initial deflection. Note also the extended path wing's maximum voltage was

0.2 volts less than the regular wing. The experimental deflection values are only a few microns short of the simulated deflection range which suggests removing the substrate and nitride layers would allow the devices to meet or exceed the simulated maximum deflection range with increased bias.

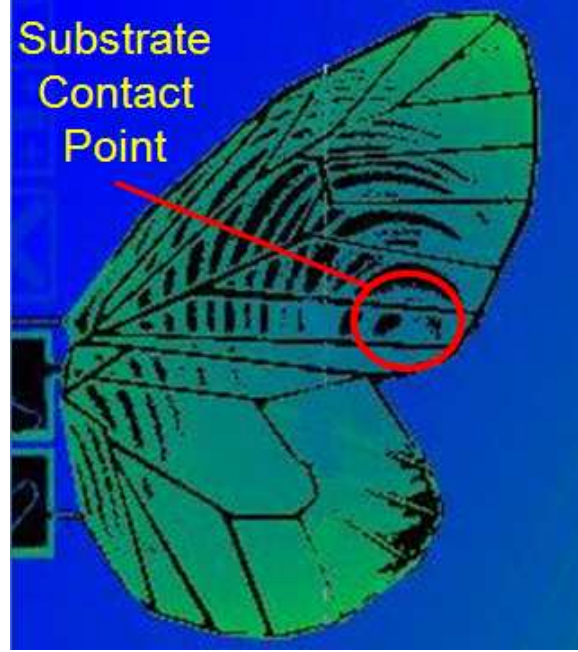


Figure 6.9: Large butterfly wing which has reached its deflection limit by coming into contact with the chip substrate.

Four 330 by 319  $\mu\text{m}$  butterfly wings were tested to determine their flapping frequency, two for the regular large wing and two for the extended path large wing. One of the regular large butterfly wings had to be heated until part of the device discolored before flapping began. In this same wing, the gold layer began to peel off of the wing under 1.75 volts of applied bias. A total of 12 experimental frequencies were collected on the regular large butterfly wing and 14 were collected for the extended path large butterfly wing. These values were averaged to yield flapping frequencies of 16.67 Hz and 10 Hz for the regular and extended path butterfly wings, respectively.

One area of concern from the large extended path butterfly wing simulation was the loss of twisting in the wing during deflection. Table 6.3 shows experimental results for measurements on the top and bottom halves of an extended path large

butterfly wing. These results indicate that both the initial deflection and incremental deflections are greater in the top portion of the wing. Therefore, the wing should continue to twist while flapping which is contrary to the simulated results.

Table 6.3: Deflection measurements for the top and bottom half of a large extended path butterfly wing; results indicate wing twisting until contacting the substrate.

<b>Deflection Measurements for Both Halves of Butterfly Wing</b>										
<b>Voltage</b>	0	0.5	0.7	0.9	1.2	1.4	1.6	1.7	1.8	1.9
<b>Top Half Deflection</b>	12.768	11.567	11.046	9.904	6.522	4.382	3.420	2.576	1.899	contact
<b>Bottom Half Deflection</b>	5.524	4.928	4.735	3.667	2.370	2.024	1.660	1.054	0.383	contact

Table 6.4 summarizes the experimental results for the butterfly wing tests. The table averages at least three and as many as six data points for each individual butterfly wing type tested. This averaging provided a single deflection and voltage value for each type of butterfly wing. It is clear from the table that the larger wings get better initial deflection than their smaller counter parts and the same holds true for total deflection. The run 84 butterfly wings significantly out perform the same size wings from run 83 in terms of total deflection. Anchoring the actuation lines again resulted in reduced initial deflection of the run 84 butterfly wings just as it did in the case of the house fly wings. However, the resulting total deflection was approximately 5 times greater than the same size wings of run 83. Note also that the regular large butterfly wing of run 84 had greater initial deflection than the extended path large butterfly wing but the extended path wings reached the substrate deflection limit at 0.2 volts less applied bias.

Figure 6.10 shows a test device wire bonded out to a chip carrier with a close-up of the ground pad bond. Wire bonding the actuation pads out to a chip package removed the dependency of probing them manually with the physical probe. This not only made testing easier, but was a step in the right direction for allowing the devices to undergo tethered flight. Although wire bonding was beneficial, the choice of chip

Table 6.4: This table provides the type of butterfly wing, MUMPs® Run, average initial deflection, average total deflection and average maximum voltage for each type of house fly wing.

Summary of Experimental Results for the Butterfly Wings				
Wing Type	Run	Average Initial Deflection ( $\mu\text{m}$ )	Average Total Deflection ( $\mu\text{m}$ )	Average Maximum Voltage
Small Wing	83	6.636	1.548	1.250
Large Wing	83	18.975	3.347	1.458
Extended Path Large Wing	84	12.915	15.665	1.867
Regular Large Wing	84	14.131	16.881	2.067

package and close proximity of the bonding pads made it difficult to successfully bond the majority of the devices.

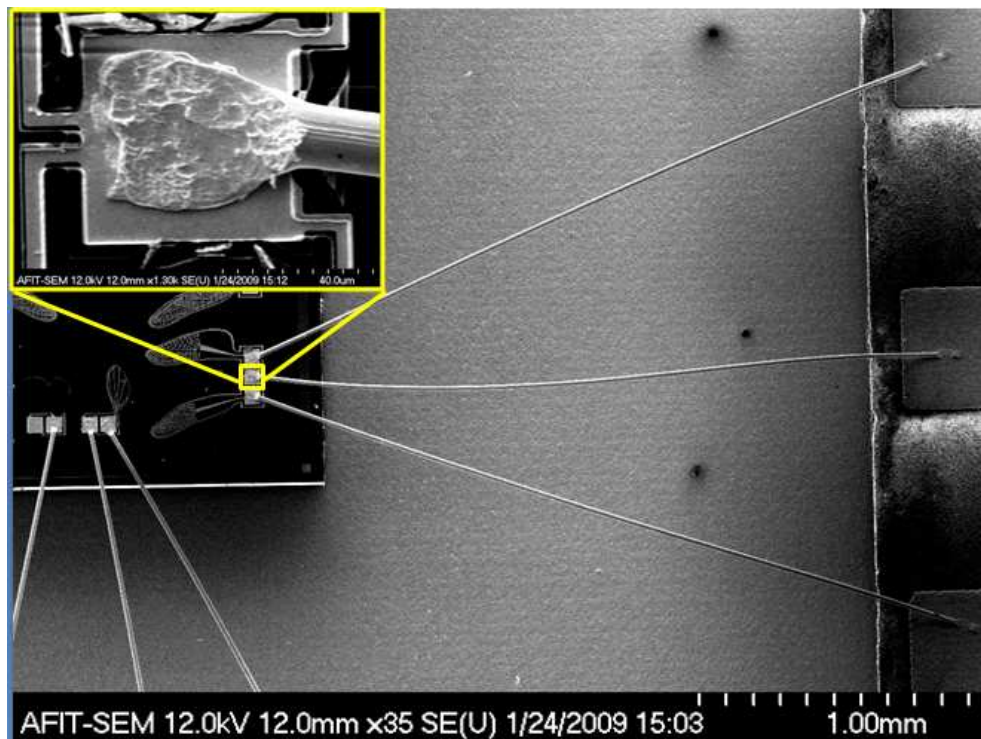


Figure 6.10: Extended path large dragonfly test wings wire bonded out to a chip carrier. The close-up of the ground pad shows a wedge type bond which was used on both the device and chip package side of the wire bond.

## 6.5 *Analytical Results*

This section provides basic analytical results on sub-millimeter flapping devices. Five aerodynamic properties for each wing type were calculated: aspect ratio, reduced frequency, Reynolds number, drag force, and gravitational force. The primary reason for calculating these properties was to establish a baseline of aerodynamic values for sub-millimeter flying devices because no current data was found for flying devices of this scale.

The aspect ratio of each wing design was calculated using Equation 3.5. Appendix C, Section C.1 shows calculations for the aspect ratio of each wing design. Two separate calculations were performed, one for run 83 devices and one for run 84 devices. The dragonfly wings had the greatest aspect ratio, followed by the fly, and then the butterfly for both run's devices. Notice also that the run 84 devices have matching aspect ratios for the small and large wings of the same design type. This was due to an L-edit scaling tool that allowed the small wings to be exactly doubled into the larger wing designs of run 84.

Equation 3.7 is used to calculate the reduced frequency of hovering flapping devices. The wing beat amplitude for each wing was calculated using geometry and the experimental deflection measurements for each wing. Each run 83 wing type had 3-5 experimental results, depending on how well they survived the release and experimental processes, which were averaged to provide one wing beat amplitude for each wing. Each run 84 wing type was averaged for 3 experimental results. Combining these calculated wing beat amplitudes with the previously calculated wing aspect ratios provided the necessary information to calculate the reduced frequency for the hovering devices. Appendix C, Section C.2 contains detailed calculations for the different wings. The reduced frequency was opposite of the aspect ratio in terms of which types of wings had the greatest reduced frequency.

Another analytical result dealing with aerodynamics is the Reynolds Number of a hovering device. Equation 3.4 was used to calculate the Reynolds Number for each

wing type. This equation uses the wing beat amplitude, wingspan, and aspect ratio already calculated in conjunction with the experimental results for flapping frequency. While testing the various wing structures, the flapping frequency at each data point was recorded. These recorded frequencies (from 10-27 data points depending on the wing type) were then averaged for each wing type to provide a single flapping frequency per wing type. Combining all this data into Equation 3.4 resulted in a Reynolds Number for each wing type. Appendix C, Section C.3 shows the calculations for Reynolds Numbers of hovering devices in more detail.

Table 6.5 lists these three analytical results of run 83 with their respective wing designs. Notice that each large wing has a greater Reynolds number than its corresponding small wing. This increase in Reynolds Number for larger structures follows the trend seen in Figure 3.5. The fly wing designs were the only wing designs of run 83 that had matching aspect ratios. This is a result of the larger wings in the dragonfly and butterfly wings not scaling to exactly twice the size of the smaller wings.

Table 6.5: Calculated reduced frequency, aspect ratio, and Reynolds number for run 83 devices; each value is unitless.

<b>Analytical Results of MUMPs® Run 83 Bio Wings</b>			
<b>Wing Type</b>	<b>Reduced Frequency (hovering)</b>	<b>Aspect Ratio</b>	<b>Reynolds Number (hovering)</b>
Small Forewing	35.06	5.189	0.001384
Large Forewing	38.53	4.488	0.005809
Small Back Wing	76.82	3.822	0.000846
Large Back Wing	85.25	4.454	0.002344
Small Fly Wing	299.11	2.914	0.000519
Large Fly Wing	97.82	2.914	0.004635
Small Butterfly Wing	289.19	1.146	0.000815
Large Butterfly Wing	267.05	1.153	0.008833

Table 6.6 shows the analytical results for each run 84 wing type. The property of larger wings having greater Reynolds numbers than the same type of smaller wing holds true for run 84 as well. The data in this run also shows aspect ratios to be



the same for each type of wing regardless of whether it is large or small. This is attributed to exact scaling of the large wings to twice the size of the smaller wings. Reduced frequency in the run 84 devices appeared to be grouped by wing type lowest to greatest: dragonfly wings, house fly wings, and butterfly wings. Since reduced frequency measures the unsteadiness of flow, it makes sense that the butterfly wings have the greatest reduced frequency due to their additional twisting during flapping.

Table 6.6: Calculated reduced frequency, aspect ratio, and Reynolds numbers for run 84 devices.

<b>Analytical Results of MUMPs® Run 84 Bio Wings</b>			
<b>Wing Type</b>	<b>Reduced Frequency (hovering)</b>	<b>Aspect Ratio</b>	<b>Reynolds Number (hovering)</b>
Entire Vein Small Forewing	14.27	4.488	0.004080
Entire Vein Large Forewing	9.03	4.488	0.033458
Entire Vein Small Back Wing	16.66	3.783	0.004314
Entire Vein Large Back Wing	16.04	3.783	0.026490
Extended Path Small Forewing	17.26	4.488	0.003883
Extended Path Large Forewing	13.14	4.488	0.021438
Extended Path Small Back Wing	21.52	3.783	0.004357
Extended Path Large Back Wing	18.11	3.783	0.024907
Extended Path Large Fly Wing	26.67	2.914	0.029910
Large Fly Wing	27.73	2.914	0.033134
Extended Path Large Butterfly Wing	56.40	1.174	0.011653
Large Butterfly Wing	52.35	1.174	0.020928

Another two analytic calculations performed for the bio-wing designs were the drag and gravitational force calculations. Using Equation 3.2, the experimental results, and an assumed coefficient of drag of 2, which is the drag coefficient for small insects [35], the drag force was calculated for each bio-wing system. The gravitational force, which is the mass of the device multiplied by acceleration due to gravity, is the force that must be overcome by the drag force in order for the device to lift off. Table 6.7 shows the calculated values for each of the wing systems. Detailed gravitational force calculations can be found in Appendix C, Section C.4 and detailed drag force calculations can be found in Appendix C, Section C.5.

Table 6.7: Calculated gravitational and drag forces for each type of bio-wing system designed and fabricated.

<b>Weight and Drag Force Calculated Values</b>			
<b>Wing System</b>	<b>Drag Force (N)</b>	<b>Gravitational Force (N)</b>	<b>Run</b>
Small Dragonfly System	4.232E-16	4.646E-08	83
Large Dragonfly System	5.894E-15	4.718E-08	83
Small Fly System	2.604E-17	2.787E-08	83
Large Fly System	2.103E-15	2.832E-08	83
Small Butterfly System	2.545E-17	2.796E-08	83
Large Butterfly System	3.015E-15	2.869E-08	83
Entire Vein Small Dragonfly System	4.848E-15	3.455E-08	84
Entire Vein Large Dragonfly System	2.577E-13	3.511E-08	84
Extended Path Small Dragonfly System	4.650E-15	3.449E-08	84
Extended Path Large Dragonfly System	1.474E-13	3.412E-08	84
Large Fly System	1.069E-13	1.946E-08	84
Extended Path Large Fly System	8.696E-14	1.844E-08	84
Large Butterfly System	1.760E-14	1.953E-08	84
Extended Path Large Butterfly System	5.318E-15	1.951E-08	84

Table 6.7 shows that further improvements must be made for the devices to fly, but the table also shows progress between the design runs. The progress was primarily attributed to the increased deflection range of the run 84 devices. The run 84 small dragonfly systems improved drag force by one order of magnitude while the weight of the system was slightly reduced from the run 83 dragonfly system. While the weight of the run 84 large dragonfly systems was reduced a small amount, the drag force was increased by two orders of magnitude over the run 83 large dragonfly system. The entire vein structure produced a little more drag force than the extended path systems, but it was also slightly heavier. Run 83 and 84 large fly system designs were exactly the same except for anchoring the ground lines in run 84. This improvement resulted in two orders of magnitude more drag force for run 84. The extended path large fly system showed one order of magnitude improvement over the run 83 system and had the lowest gravitational force of all three large fly systems. Run 83 and 84 large butterfly designs were also the same except for ground line anchoring. This lead

to one order of magnitude improved drag force in the run 84 system. The extended path large fly wing was only slightly greater in drag force than the run 83 large butterfly system, but it had the smallest gravitational force out of the three large butterfly wing systems.

Increasing the wing surface area, frequency, and deflection range all lead to greater drag force. However, increasing the surface area is a trade-off because it also increases the weight of the device. The increase in drag force among the run 84 systems was primarily due to the increase in wing deflection, which was a direct result of anchoring the ground lines. However, anchoring the ground lines to the substrate caused an increase in weight, but thinning the substrate by 300  $\mu\text{m}$  reduced the overall weight of the wing systems. Extending the current paths also reduced weight because most of the gold interconnections along the perimeter were removed. Note, even the devices with an entire vein structure (additional gold) are lighter than the corresponding wing systems of run 83 due to these upgrades.

Calculations were also performed to see how much faster the current wings need to flap in order to achieve lift off. Table 6.8 shows the frequency required for each wing system to lift off assuming the deflections and weights of the system are unchanged. These high frequencies suggests that the best way to improve the drag force is to continue improving the deflection of the wings.

Table 6.8: Flapping frequencies required in order for the current wing systems to lift off without changing weight or deflection range.

<b>Required System Frequency to Achieve Lift Off</b>	
<b>Wing System</b>	<b>Frequency</b>
Entire Vein Small Dragonfly System	96900
Entire Vein Large Dragonfly System	18925
Extended Path Small Dragonfly System	121700
Extended Path Large Dragonfly System	24275
Large Fly System	25250
Extended Path Large Fly System	23700
Large Butterfly System	17775
Extended Path Large Butterfly System	19150

## **6.6 Chapter Summary**

This chapter discussed several different kinds of assembly and connected wings. The continued pursuit of these types of wings was suspended due to the success of the bio-wings. Experimental results helped to discover design flaws such as the ground line failure in run 83 devices. The next design iteration, MUMPs® run 84, was used to correct these design flaws and make continuous advances in the flapping bio-wings. Experimental data confirmed the need to remove the substrate and nitride layers for many of the devices to reach their full flapping potential. This chapter also focused on establishing a baseline of analytical aerodynamic parameters for sub-millimeter flying devices. Weight and drag force calculations were also performed to measure the progress of the wing systems toward flight capability. The next chapter will focus on conclusions and potential future improvements for the advancement of flying MEMS.

## VII. Conclusions

### 7.1 Chapter Overview

This chapter presents the conclusions on flapping MEMS devices resolved from this research effort. The conclusions are broken down into three general categories: connected wings, assembly wings, and bio-wings. The bio-wings are further categorized into dragonfly, house fly, and butterfly wings. Novel contributions and recommendations for future work on micro flying devices will also be discussed.

### 7.2 Conclusions

Connected wings proved to be a poor design for flapping wing devices. The results of the thesis showed that forcing an out of plane deflection on a device with solid connections provides very little deflection. In order to correct this limitation, a second hinge point on the wing structure would need to be added. Ability to create a double hinge structure at different levels on the device was not possible using the PolyMUMPs<sup>TM</sup> process. Therefore, the connected wing was eliminated as a possible flapping wing design due to fabrication process limitations.

Assembly wings were a better design scheme than the connected wings. The initial problem with the assembly wings was connecting the actuation arm into the latch which would function as the second hinge point on the device. Assembly aids were added to the wing design to help make this connection. Though the assembly aids helped in making this connection, it was still a manual process of using a probe to interconnect the latch with the actuation arm. This design could continue to improve by making a completely self assembling device, but it would still have a large actuation scheme. Though this design was not completely ruled out as a flapping wing design, it was suspended as an option in favor of the bio-wings.

Bio-wings showed great potential as viable designs for flapping wing devices. Each of the three types of bio-wings were constructed of a thermal bimorph structure consisting of polysilicon and gold. Joule heating using a variable input bias voltage was used to actuate the bimorph designs. This heating was initially causing the

ground lines to fail which was resolved by anchoring them to the substrate. Many of the wing designs were then able to deflect as far as the substrate. The substrate deflection limit can be resolved with a back side DRIE to create holes beneath the wings. Having proved flapping capability of these wings, the main limiting factor becomes creating a way to power and control the device to free it from being linked to a set of biasing probes.

The large dragonfly fore and back wings with and without full vein structure showed the greatest initial deflection among the bio-wings. They also had the largest overall deflection range. This means that the dragonfly wings are able to displace more air and should therefore generate more lift than the other devices. However, it is also necessary for the dragonfly system to generate more lift because it consists of four wings and therefore has more mass. With proper control, this system also offers more maneuverability due to the four wing system.

The fly wings did not deflect as far as the dragonfly wings but experienced two advantages over the dragonfly wings and possibly a third. The first advantage was the ability to deflect into the substrate as seen in the extended path large fly wing experiments. This means that the wings will deflect further with the removal of the substrate and increased bias. The increasing of the bias means the maximum voltage handled by the device would be even greater than the already 0.2-0.4 volts advantage the fly wings experience over the dragonfly wings. Since the wings shed their vortices when changing direction during their wing stroke, the vortices of the extended path fly wing will be able to combine beneath the fly system similar to the actual insect. This should aid in the ability of the device to realize flight.

Both the regular and extended path butterfly wings experienced deflections resulting in contact with the substrate. Therefore, the butterfly wing should experience some of the same advantages of the fly wings. The major distinct advantage of the butterfly wings is their ability to twist while deflecting. Most insects rotate their wings while flapping so the twist that occurs in the butterfly wings during flapping

closely emulates this phenomena than the other two flapping wing designs. The next section lists novel contributions to the micro flying arena.

Wire bonding the devices to a chip package was possible but after a discussion with AFRL technicians many additional factors should be considering for any future wire bonding attempts. The current bond pads are about 30 percent smaller than the footprint of the bonding tool but it was able to make good bonds on the pads. The spacing of the bond pads was a bigger problem than their size but increasing the spacing of the pads would increase the weight of the wing system. Choosing a chip package with more pins would help alleviate some spacing issues on the packaging side as well as allow for more devices to be bonded out. Having the package and the chip pads on the same plane also makes wire bonding easier especially when the length of the wires is increased. The longer the wires, the harder it becomes to prevent them from laying on the surface near the pad. It is recommended that any future students that may require wire bonding discuss their designs with technicians before fabrication to establish a plan of attack.

### **7.3 *Novel Contributions***

Since micro flying devices is a little explored technology, any novel contributions to the field are worthy of mentioning. The following is a list of novel advancements from this thesis.

1. Designed a micro-scale flapping wing with an initial deflection greater than any previously designed ( $36.928\text{ }\mu\text{m}$ ), best previously recorded by Daniel Denninghoff at  $30.9\text{ }\mu\text{m}$  [35]. Since the wing designs were nearly the same size in terms of wingspan, a  $6\text{ }\mu\text{m}$  improvement in initial deflection is significant.
2. Deflected multiple wings into the substrate surface beneath the wings indicating a progressively larger flapping range
3. Designed a wing capable of deflecting and twisting simultaneously

4. Successfully combined multiple wings to form three bio-wing flapping systems each less than one cubic millimeter in size
5. Calculated three aerodynamic properties (reduced frequency, aspect ratio, and Reynolds number) for hovering micro scale devices to establish a baseline for MEMS flying devices

This research has resulted in an invitation to present at the Dayton-Cincinnati Aerospace Sciences Symposium (DCASS). DCASS is the 34th annual symposium scheduled for 3 March 2009 in Dayton, Ohio. The required abstracts for acceptance to present at the symposium will be published through the Dayton-Cincinnati Section of the American Institute of Aeronautics and Astronautics (AIAA).

A portion of this research was also accepted as a paper and presentation topic for the Society for Experimental Mechanics Annual Conference and Exposition on Experimental and Applied Mechanics. This conference takes place in Albuquerque, New Mexico from 1-4 June 2009. The accepted presentation and paper title which will be published in the conference proceedings is "Residual Stress for Assembling, Partially Assembling and Actuating MEMS Devices."

#### ***7.4 Recommendations for Future Work***

One recommendation for future improvements has been mentioned already and that is the removal of the nitride and substrate layers. This would allow the wing structures to continue deflecting beyond the substrate ultimately improving the performance of the device. The masks for back side etching have already been developed for both a 700  $\mu\text{m}$  thick substrate and a 400  $\mu\text{m}$  thick substrate. Multiple chips have also been patterned with the appropriate back side mask and are ready for the DRIE process. Once a reliable DRIE machine is online, this upgrade could be implemented.

Another recommendation is to make the structure with a more flexible material that more closely represents an actual insect wing. This would most likely require using a different fabrication process such as a laser micromachining process. A good



material choice would be a laminate or polyimide material because of their flexibility and reduced weight. The wing should also have a gradual slope up into the middle forming an upside down U pattern to capitalize on aerodynamic forces.

Other future avenues to explore include additional testing. One test that may prove useful in understanding why some wings twist and others do not would be a thermal test on the wing surface. An infrared camera could be used to determine the uniformity of joule heating across the wing structure. By understanding how the wing heats, design iterations could focus on controlling and manipulating the wing to flap and twist as desired. Another test would include extracting aerodynamic data from high speed video taken on the flapping wings. By capturing the flapping results with this high speed video, answers on maximum flapping frequency and total deflection range could be fully verified. Adding smoke or dry ice to the experiment could also answer questions on how LEV effect the micro scale wings.

## ***7.5 Chapter Summary***

Several wing types were explored in this thesis. While some did not prove to be effective flapping wing designs, the bio-wing designs showed great promise for the advancement of a micro scale flying device. Several of these novel contributions to the micro flying arena were listed. Additionally, a few presentations that will showcase these advancements were also highlighted. Multiple recommendations were also made for the continued advancement of flapping wing technology.

## Appendix A. L-edit Design Layouts

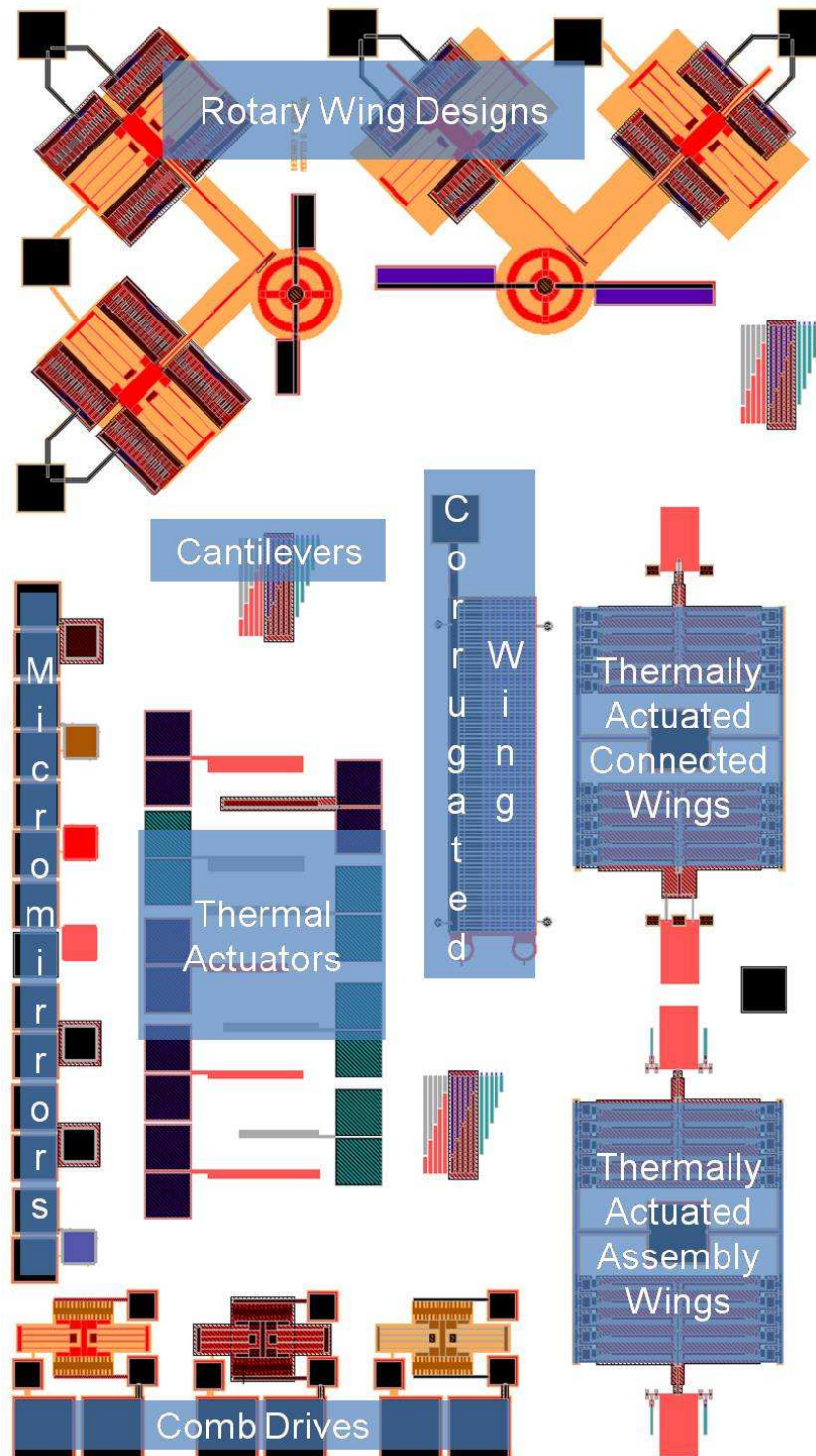


Figure A.1: L-edit layout of MUMPs® run 82.

Table A.1: This table briefly describes the L-edit layout of Figure A.1.

MUMPS Run 82	
Micromirrors	Mirrors fabricated to EENG 636 specifications
Thermal Actuators	Thermal Actuators that served as the basic understanding for more complicated thermal actuator designs
Comb Drives	Comb Drives fabricated to EENG 636 specifications
Cantilevers	Basic cantilevers structures for understanding residual stress
Rotary Wing Designs	Rotary designs that combined comb drive technology with various wing designs
Corrugated Wing	Wing design from prior AFIT student
Thermally Actuated Connected Wings	Single and double connection points connected to a group of 10 double hot arm thermal actuators
Thermally Actuated Assembly Wings	A group of 10 double hot arm actuators that must be latched to the wing structure for operation

Table A.2: A brief description of the L-edit layout shown in Figure A.2.

MUMPS® Run 83	
Test Wing Structures	Various test wings for the fly, dragonfly, and butterfly wings with actuation occurring at different points on the wings
Fly Wings	Large and small scale fly wing systems with center activation
Dragonfly Wings	Large and small scale dragonfly wing systems with activation at center, leading and trailing edges
Butterfly Wings	Large and small scale butterfly wings with center activation
Flip Chip Design	Comb drive assembly to be flip chip bonding to a wing at 90 degree angle
X-Wings	Wings designed to be activated in opposition from each other to create flapping motion in an X pattern
Wing Frame	Basic frame of dragonfly wing constructed of poly2 layer

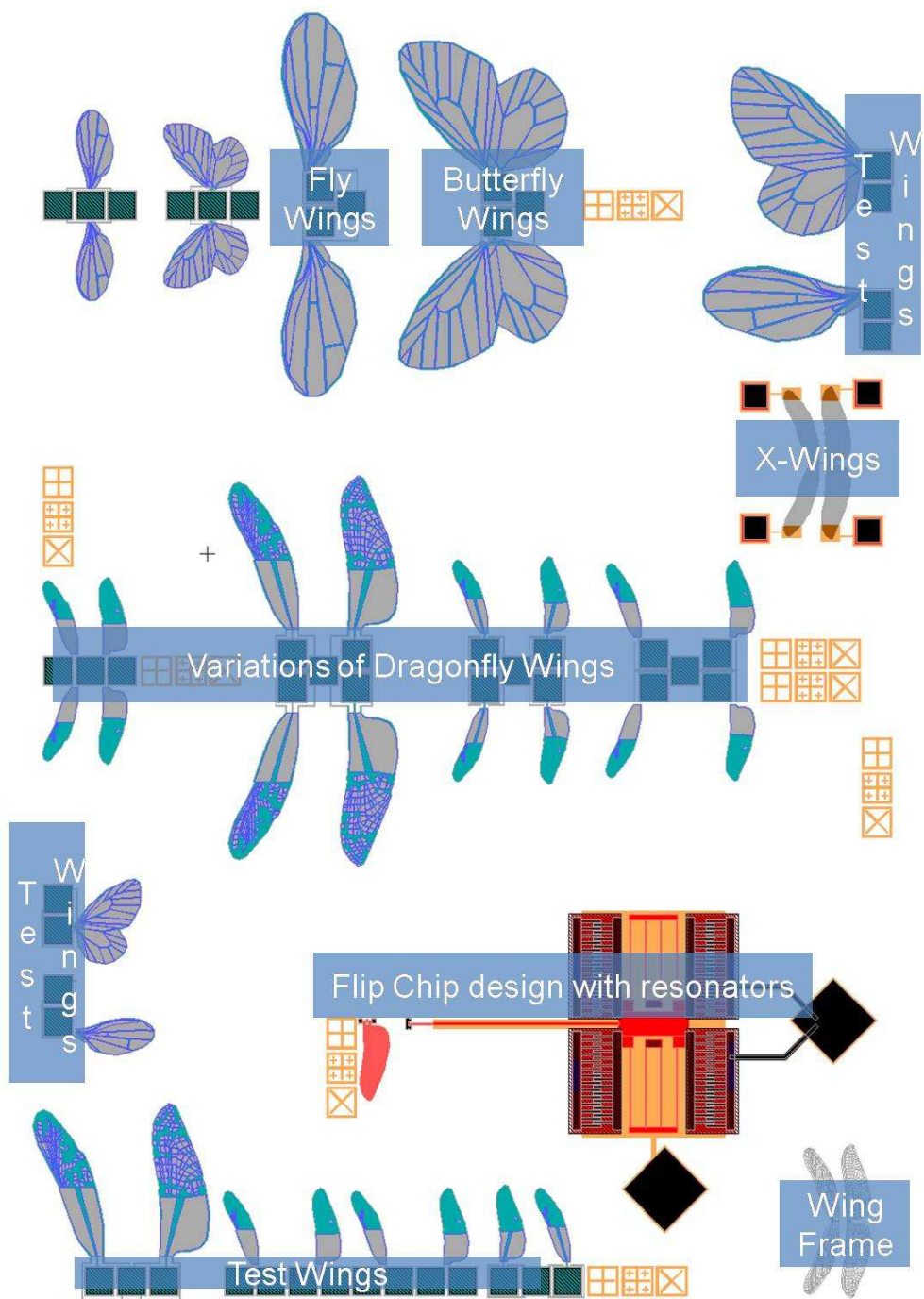


Figure A.2: L-edit layout of MUMPs® run 83.

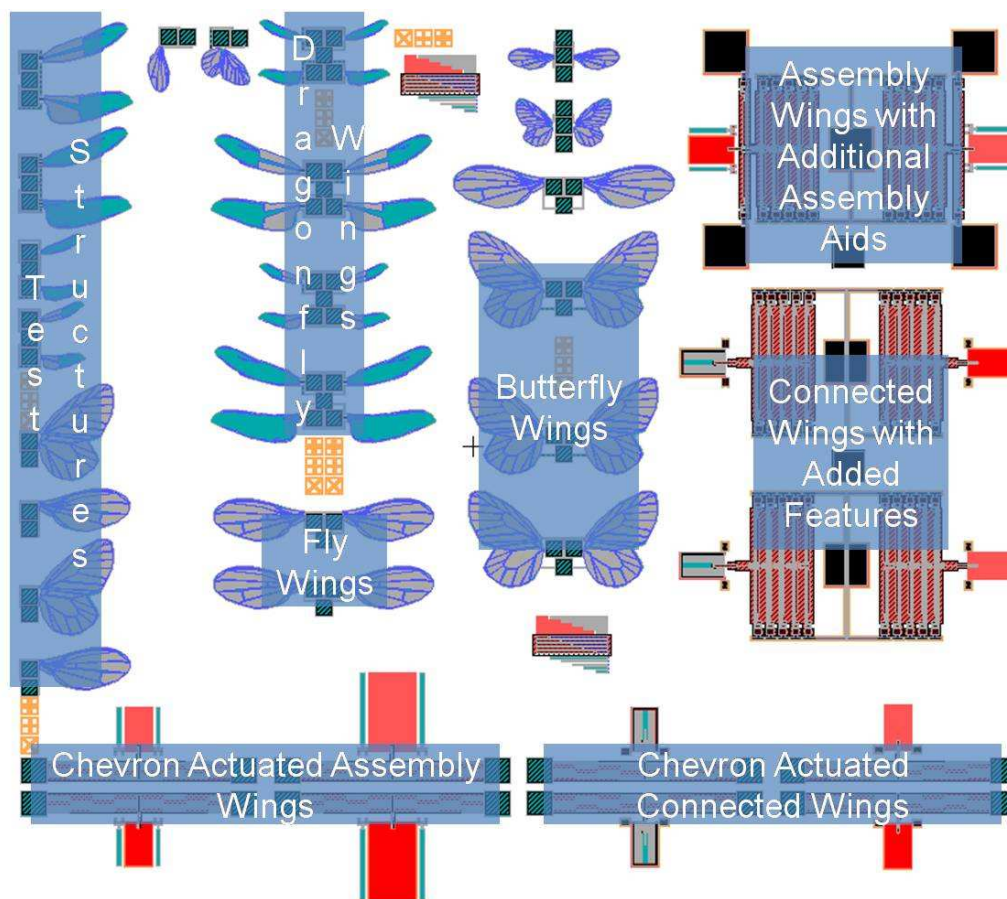


Figure A.3: L-edit layout of MUMPs® run 84.

Table A.3: Information on L-edit layout of run 84 shown in Figure A.3.

MUMPs Run 84	
Assembly Wings with Additional Assembly Aids	Assembly wings with increased cantilever deflection and additional actuators to aid in assembly
Connected Wings with Added Features	Pushed connections further into the wing structure, added gold for initial deflection, poly2 wing structure for decreased weight
Butterfly Wings	Large and Small butterfly wings with increased current path to force current out to the tip of the wing
Dragonfly Wings	Dragonfly wings with multiple actuation points and longer current path
Test Structures	Test wings for each type of bio-wing and activation scheme
Fly Wings	Large and Small fly wings with increased current path to force current out to the tip of the wing
Chevron Actuated Connected Wings	Same wings as connected wings with chevron activation
Chevron Actuated Assembly Wings	Small and large scale wings with chevron activation

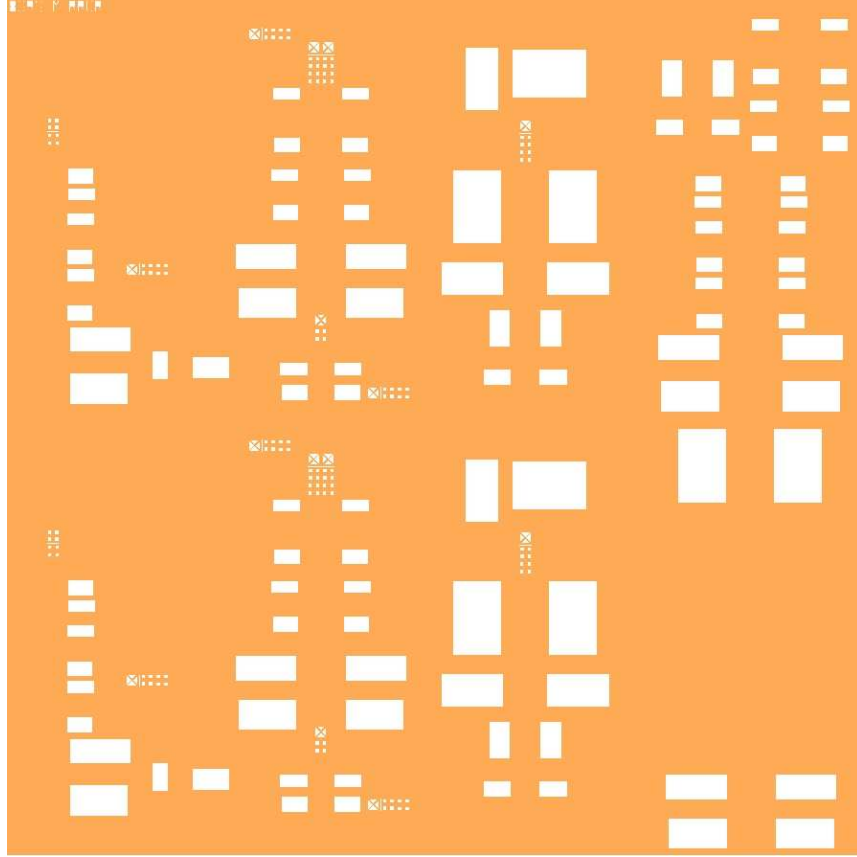


Figure A.4: Back side mirrored mask layout for MUMPs® run 83 to align etch pattern with designs on the front side of the chip. This mask was designed for a 20:1 (20 deep, 1 wide) DRIE where the substrate was  $700\text{ }\mu\text{m}$  thick. A nearly identical mask, with the same patterns but slightly different dimensions, was created for devices with a  $400\text{ }\mu\text{m}$  substrate.



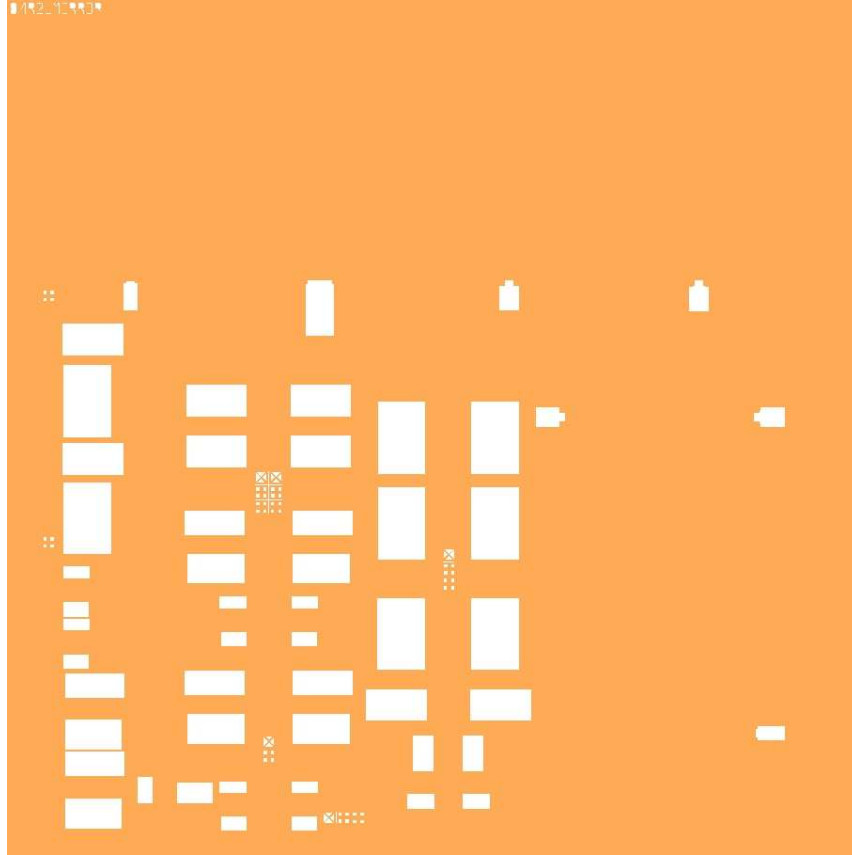


Figure A.5: Back side mirrored mask layout for MUMPs® run 84 used to align etch pattern with wing designs on the front of the chip. This mask was designed for a 20:1 (20 deep, 1 wide) DRIE where the substrate was 700  $\mu\text{m}$  thick. A nearly identical mask was created for devices with a substrate thinned to 400  $\mu\text{m}$ .



## Appendix B. Process Followers

### B.1 Release

Table B.1: Step by step instructions for release with CO<sub>2</sub> Dryer

Release Process using the CO <sub>2</sub> Dryer	
Process Step	Notes
<b>Remove photoresist</b> - Submerge in acetone for 20 min	Layer applied by manufacturer to protect MEMS devices in transit Occasionally agitate
<b>Release</b> - Submerge in HF for 2-10 min, Agitate occasionally - Remove chip from HF and place in methanol bath for 4 min - Move chip to another methanol bath for 10 min	Amount of time depends on design features Stops the etching Prepares chip for critical drying
<b>Critical Drying</b> - Fill Tousimus® CO <sub>2</sub> dryer with methanol - Move chip directly from methanol bath to dryer - Seal the dryer and start the process	Should cover the chip completely  The dryer will cycle through the entire process automatically once started
<b>Verify Devices Released</b>	

Table B.2: Step by step instructions for release with hot plate

<b>Release Process using the Hot Plate</b>	
<b>Process Step</b>	<b>Notes</b>
<b>Remove photoresist</b> - Submerge in acetone for 20 min	Layer applied by manufacturer to protect MEMS devices in transit Agitate occasionally
<b>Release</b> - Submerge in HF for 2-10 min  - Remove chip from HF and place in isopropyl bath for 4 min - Move chip to another isopropyl bath for 10 min	Amount of time depends on design features Stops the etching  Prepares chip for critical drying on hot plate
<b>Critical Drying</b> - Place chip on 110° C hot plate for 5 min	
<b>Verify Devices Released</b>	

## ***B.2 Backside Etching***

Table B.3: Step by step instructions for backside etching

<b>SI Wafer Backside Etching</b>	
<b>Process Step</b>	<b>Notes</b>
<b>Thin Wafer Substrate</b>	AFRL, RIE substrate to approximately 400 $\mu\text{m}$
<b>Apply backside oxide</b> <b>Note:</b> if a thick black residue is left on chip	PECVD, 2-3 $\mu\text{m}$ place in 400K developer for 24 hours then wipe clean with an isopropyl soaked cotton swab to remove the residue
<b>Clean Wafer Backside:</b> -Apply acetone to cotton swab and clean wafer backside -Dry with nitrogen	
<b>Apply Photoresist:</b> -Flood the wafer with Shipley's <sup>TM</sup> 1818 photoresist -Spin ramp of 500 rpm for 5 sec -Continue spinning at 5000 rpm for 30 sec -Bake on hot plate for 75 sec at 110 C	Reduces edge bead
<b>Backside Alignment and Exposure:</b> -Backside align the desired Photosciences <sup>©</sup> mask with desired pattern on the wafer  -Expose for 3 sec	Recipe: Mask thickness: 1.5 mm Substrate thickness: 1.55 mm Photoresist thickness: 1.8 mm Separation: 60 $\mu\text{m}$ - An additional blank slide may need placed on top of other slide to prevent mask from contacting the chip
<b>Develop Wafer:</b> -Develop with 351 developer for 30 sec at 500 rpm -Rinse with DI water 30 sec at 500 rpm -Dry with nitrogen at 500 rpm	1:5; 351:DI water
<b>Inspect Lithography:</b> -Place wafer under microscope and inspect for desired pattern and sharp definition	
<b>Etch patterned mask into oxide</b>	AFRL
<b>DRIE the wafer</b>	AFRL

## *Appendix C. Analytical Calculations*

### *C.1 Aspect Ratio*

To calculate the aspect ratio of each run 83 and 84 wing simultaneously, a matrix for each wing's span and area were setup in Mathcad®. The wingspan and area measurements taken directly from L-edit, both measured in microns, were then plugged into Equation 3.5.

$$wingspan = \begin{bmatrix} 200 \\ 372 \\ 195 \\ 388 \\ 199 \\ 398 \\ 163 \\ 327 \end{bmatrix}, area = \begin{bmatrix} 7709 \\ 30836 \\ 9950 \\ 33799 \\ 13589 \\ 54356 \\ 23193 \\ 92772 \end{bmatrix}, \Lambda = \frac{(wingspan)^2}{area}, \Lambda = \begin{bmatrix} 5.189 \\ 4.488 \\ 3.822 \\ 4.454 \\ 2.914 \\ 2.914 \\ 1.146 \\ 1.153 \end{bmatrix}$$

The resulting matrix,  $\Lambda$  for run 83, was the aspect ratio of the eight wing designs: small forewing, large forewing, small back wing, large back wing, small fly wing, large fly wing, small butterfly wing, and large butterfly wing respectively.

$$\begin{array}{c}
wingspan = \begin{bmatrix} 186 \\ 372 \\ 194 \\ 388 \\ 186 \\ 372 \\ 194 \\ 388 \\ 398 \\ 398 \\ 330 \\ 330 \end{bmatrix}, area = \begin{bmatrix} 7709 \\ 30836 \\ 9949.82 \\ 39799.28 \\ 7709 \\ 30836 \\ 9949.82 \\ 39799.28 \\ 54356 \\ 54356 \\ 92772 \\ 92772 \end{bmatrix}, \Lambda = \begin{bmatrix} 4.488 \\ 4.488 \\ 3.783 \\ 3.783 \\ 4.488 \\ 4.488 \\ 3.783 \\ 3.783 \\ 2.914 \\ 2.914 \\ 1.174 \\ 1.174 \end{bmatrix}
\end{array}$$

The resulting matrix,  $\Lambda$  for run 84, was the aspect ratio of the 12 wing designs: entire small vein forewing, entire large vein forewing, entire small vein back wing, entire large vein back wing, extended path small forewing, extended path large forewing, extended path small back wing, extended path large back wing, extended path large fly wing, large fly wing, extended path large butterfly wing and large butterfly wing, respectively.

### ***C.2 Reduced Frequency (Hovering)***

The wing beat amplitude of each wing was calculated from experimental deflection measurements. In order to find this value in radians, the arc tangent of the maximum deflection over the span of the wing was calculated. Then the deflection just prior to device failure was also calculated in the same manner. If the device failure value was below the point where the wing was level then the two values were added but if the value was above the level point then the two values were subtracted to give the wing beat amplitude. For the same types of wings with multiple experimental results, the calculated values were averaged to

provide one wing beat amplitude for each type of wing. These wing beat amplitude calculations in radians were performed in Excel® with the following formula: *wing beat amplitude* = (*ATAN(maximum deflection/wingspan)* + or - *ATAN(final deflection/wingspan)*, *ATAN(maximum deflection/wingspan)* + or - *ATAN(final deflection/wingspan)*, ...). These numbers were then made into a matrix in Mathcad®. Plugging the wing beat amplitude ( $\Phi$ ) and the aspect ratio ( $\Lambda$ ) into Equation 3.7 allowed for each wing's reduced frequency to be solved simultaneously.

$$\Lambda = \begin{bmatrix} 5.189 \\ 4.488 \\ 3.822 \\ 4.454 \\ 2.914 \\ 2.914 \\ 1.146 \\ 1.153 \end{bmatrix}, \Phi = \begin{bmatrix} 0.017270 \\ 0.011307 \\ 0.010701 \\ 0.006749 \\ 0.003604 \\ 0.008375 \\ 0.011073 \\ 0.008572 \end{bmatrix}, k = \frac{\pi}{\Phi * \Lambda}, k = \begin{bmatrix} 35.06 \\ 61.91 \\ 76.82 \\ 104.52 \\ 299.11 \\ 128.72 \\ 247.67 \\ 317.98 \end{bmatrix}$$

The reduced frequency ( $k$ ) values appear in matrix form corresponding to the same eight wing designs for the aspect ratio of the run 83 devices.

$$\Lambda = \begin{bmatrix} 4.488 \\ 4.488 \\ 3.783 \\ 3.783 \\ 4.488 \\ 4.488 \\ 3.783 \\ 3.783 \\ 2.914 \\ 2.914 \\ 1.174 \\ 1.174 \end{bmatrix}, \Phi = \begin{bmatrix} 0.049042 \\ 0.077543 \\ 0.049851 \\ 0.051764 \\ 0.040547 \\ 0.053286 \\ 0.038599 \\ 0.045869 \\ 0.040417 \\ 0.038876 \\ 0.047451 \\ 0.051128 \end{bmatrix}, k = \begin{bmatrix} 14.27 \\ 9.03 \\ 16.66 \\ 16.04 \\ 17.26 \\ 13.14 \\ 21.52 \\ 18.11 \\ 26.67 \\ 27.73 \\ 56.40 \\ 52.35 \end{bmatrix}$$

The reduced frequency (k) values appear in matrix form corresponding to the same 12 wing designs for the aspect ratio of the run 84 devices.

### ***C.3 Reynolds Number (Hovering)***

Flapping frequency was collected at each 0.25 volt interval from each wing type experimentally tested. This data for each wing was then averaged (10-27 data points depending on the wings performance and survivability) to provide one flapping frequency for each type of wing. With the flapping frequency, wing beat amplitude, wingspan, aspect ratio, and kinematic viscosity of air ( $\nu$ ) being  $15.11 \times 10^{-6} \frac{m^2}{s}$  at room temperature, the Reynolds Number for each device was computed simultaneously using Excel<sup>®</sup> and Equation 3.4.

$$f = \begin{bmatrix} 39.26 \\ 40.00 \\ 30.00 \\ 10.00 \\ 40.00 \\ 40.00 \\ 10.00 \\ 35.24 \end{bmatrix}, \Lambda = \begin{bmatrix} 5.189 \\ 4.488 \\ 3.822 \\ 4.454 \\ 2.914 \\ 2.914 \\ 1.146 \\ 1.153 \end{bmatrix}, \Phi = \begin{bmatrix} 0.017270 \\ 0.011307 \\ 0.010701 \\ 0.006749 \\ 0.003604 \\ 0.008375 \\ 0.011073 \\ 0.008572 \end{bmatrix}, R = \begin{bmatrix} 200 \\ 372 \\ 195 \\ 388 \\ 199 \\ 398 \\ 163 \\ 327 \end{bmatrix}$$

The resultant Reynolds Number matrix follows the same pattern as both the reduced frequency and the aspect ratio in terms of matching the run 83 wings to their eight values.

$$Re = \frac{\Phi * f R^2}{v} \frac{4}{\Lambda}, ReynoldsNumber = \begin{bmatrix} 0.001384 \\ 0.003692 \\ 0.000846 \\ 0.000604 \\ 0.000519 \\ 0.004820 \\ 0.000680 \\ 0.007418 \end{bmatrix}$$

The same procedure was followed for the different wing designs of run 84.



$$f = \begin{bmatrix} 40.77 \\ 52.86 \\ 32.86 \\ 48.57 \\ 46.92 \\ 49.29 \\ 42.86 \\ 51.54 \\ 51.43 \\ 59.23 \\ 10.00 \\ 16.67 \end{bmatrix}, \Lambda = \begin{bmatrix} 4.488 \\ 4.488 \\ 3.783 \\ 3.783 \\ 4.488 \\ 4.488 \\ 3.783 \\ 3.783 \\ 2.914 \\ 2.914 \\ 1.174 \\ 1.174 \end{bmatrix}, \Phi = \begin{bmatrix} 0.049042 \\ 0.077543 \\ 0.049851 \\ 0.051764 \\ 0.040547 \\ 0.053286 \\ 0.038599 \\ 0.045869 \\ 0.040417 \\ 0.038876 \\ 0.047451 \\ 0.051128 \end{bmatrix}, R = \begin{bmatrix} 186 \\ 372 \\ 194 \\ 388 \\ 186 \\ 372 \\ 194 \\ 388 \\ 398 \\ 398 \\ 330 \\ 330 \end{bmatrix}$$

The order of the twelve Reynolds Number values correspond to the reduced frequency and aspect ratio in terms of matching the values with their respective wing types.

$$ReynoldsNumber = \begin{bmatrix} 0.004080 \\ 0.033458 \\ 0.004314 \\ 0.026490 \\ 0.003883 \\ 0.021438 \\ 0.004357 \\ 0.024907 \\ 0.029910 \\ 0.033134 \\ 0.011653 \\ 0.020928 \end{bmatrix}$$

#### C.4 Gravitational Force

The gravitational force is simply the weight of the system multiplied by the acceleration due to gravity. In order to calculate this force for the devices, the weight of each component of the wing system had to be calculated. The first component weight calculations were performed on the run 83 wings. This was calculated by figuring out the volume of each material layer of the wing and multiplying it by the density of the material. For example, the formula for the small dragonfly wing was  $wing\ weight = (((7709 * 10^{-12}) * (1.5 * 10^{-6})) * 2330) + (((2967 * 10^{-12}) * (0.5 * 10^{-6})) * 19300))$  where the terms before the + sign are for the poly2 layer and the terms after the + sign are for the gold layer. Breaking down the formula further before the + sign, the first term is the surface area, the second term is the thickness, and the final term is material density. This same formula was used for both the run 83 and 84 wings only changing the layer surface areas according to the wing being tested.

The second component calculation was performed for the actuator lines where the formula for the run 83 actuator lines was the same as the wing weight formula with different surface area values plugged in ( $actuator\ line\ weight = (((658 * 10^{-12}) * (1.5 * 10^{-6})) * 2330) + (((688 * 10^{-12}) * (0.5 * 10^{-6})) * 19300))$ ). This same basic formula was used for the run 84 actuation lines but the polysilicon thickness term (indicated in bold) was increased as a result of anchoring the lines to the substrate ( $actuator\ line\ weight = (((2127.5 * 10^{-12}) * (\mathbf{401.5 * 10^{-6}})) * 2330) + (((1595.5 * 10^{-12}) * (0.5 * 10^{-6})) * 19300))$ ). Table C.1 shows the results for the wing and actuator line weight calculations.

The final calculated component of the wing system was the actuator pads. The formulas used in Excel<sup>®</sup> for the run 83 and 84 pads were:  $actuator\ pad\ weight = (((5625 * 10^{-12}) * (701.5 * 10^{-6})) * 2330) + (((4489 * 10^{-12}) * (0.5 * 10^{-6})) * 19300))$  and  $= (((5625 * 10^{-12}) * (401.5 * 10^{-6})) * 2330) + (((4489 * 10^{-12}) * (0.5 * 10^{-6})) * 19300))$ , respectively. The resultant weights, measured in kilograms, were 9.237E-9 and 5.305E-9 respectively. Notice the only difference in the formulas was the thickness term of

Table C.1: Calculated wing and actuator line weights for each type of bio-wing designed and fabricated.

<b>Weight Calculations for the Wings and Actuation Lines (kg)</b>			
<b>Wing Type</b>	<b>Run</b>	<b>Wing</b>	<b>Actuator Line</b>
Small Forewing	83	5.557E-11	8.939E-12
Large Forewing	83	2.191E-10	1.090E-11
Small Back Wing	83	6.428E-11	8.978E-12
Large Back Wing	83	2.542E-10	1.109E-11
Small Fly Wing	83	7.458E-11	3.227E-12
Large Fly Wing	83	2.969E-10	9.070E-12
Small Butterfly Wing	83	1.202E-10	2.896E-12
Large Butterfly Wing	83	4.794E-10	8.557E-12
Entire Vein Small Forewing	84	7.401E-11	2.006E-09
Entire Vein Large Forewing	84	2.682E-10	1.949E-09
Entire Vein Small Back Wing	84	9.297E-11	1.840E-09
Entire Vein Large Back Wing	84	3.140E-10	1.759E-09
Extended Path Small Forewing	84	6.124E-11	2.006E-09
Extended Path Large Forewing	84	2.193E-10	1.642E-09
Extended Path Small Back Wing	84	7.484E-11	1.840E-09
Extended Path Large Back Wing	84	2.627E-10	1.670E-09
Extended Path Large Fly Wing	84	2.958E-10	9.674E-10
Large Fly Wing	84	2.974E-10	1.473E-09
Extended Path Large Butterfly Wing	84	5.072E-10	1.290E-09
Large Butterfly Wing	84	5.109E-10	1.296E-09

the polysilicon layer. Run 84 was 300 microns less than that of the run 83 formula. This was a result of thinning the substrate to make the devices lighter. Since the same actuator pads were used for each wing system, there are not separate actuator pad calculations for each wing.

Now that a weight for each system component has been calculated, the total system weight was calculated by summing up the component weights. The dragonfly systems consisted of five actuation pads, two forewing actuation lines, two back wing actuation lines, two forewings, and two back wings. The fly and butterfly systems consisted of three actuation pads, two actuation lines, and two wings each. The weight of each system was then multiplied by the acceleration due to gravity to produce the gravitational force of the system. The gravitational forces for each of the systems

were presented in Table 6.7. This gravitational force of each wing system represents the force that the each device must overcome in order to achieve lift off.

### ***C.5 Drag Force***

Drag force is the total amount of force generated by each of wings flapping in a system. The amount of drag force was calculated for each wing using Equation 3.2. Wing tip velocity ( $U_F$ ) was calculated by multiplying the average total deflection by the average flapping frequency for each wing type, surface area for each wing was looked up from the wing designs, and all other values of the equation were constants. Results for individual wing drag forces were as follows:

$$run\ 83 = \begin{bmatrix} 1.659E - 16 \\ 2.531E - 15 \\ 4.573E - 17 \\ 4.160E - 16 \\ 1.302E - 17 \\ 1.052E - 15 \\ 1.272E - 17 \\ 1.507E - 15 \end{bmatrix}, run\ 84 = \begin{bmatrix} 1.248E - 15 \\ 8.437E - 14 \\ 1.176E - 15 \\ 4.448E - 14 \\ 1.128E - 15 \\ 3.451E - 14 \\ 1.197E - 15 \\ 3.921E - 14 \\ 4.348E - 14 \\ 5.346E - 14 \\ 2.659E - 15 \\ 8.799E - 15 \end{bmatrix}$$

The run 83 order is small forewing, large forewing, small back wing, large back wing, small fly wing, large fly wing, small butterfly wing, and large butterfly wing. The order of the run 84 devices is entire small vein forewing, entire large vein forewing, entire small vein back wing, entire large vein back wing, extended path small forewing, extended path large forewing, extended path small back wing, extended path large back wing, extended path large fly wing, large fly wing, extended path large butterfly

wing, and large butterfly wing. The drag force of the system was then calculated by adding together the drag force of each individual wing that comprised the system. For example, the small dragonfly system would add the drag force of two small forewings and two small back wings to yield a single drag force for the small dragonfly system. Table 6.7 showed the total drag force for each wing system designed. For the system to achieve lift off, this value must exceed the corresponding gravitational force of the system.

## Bibliography

1. L.-J. Yang, "The micro aerial vehicle (mav) with flapping wings," *2005 IEEE International Conference on Mechatronics (IEEE Cat.No.05EX1025)*, pp. 811–815, 2005.
2. D. RESEARCH, D. C. V. (QUEBEC), F. Lesage, N. Hamel, X. Huang, W. Yuan, M. Khalid, and P. Zdunich, "Initial investigation on the aerodynamic performance of flapping wings for nano air vehicles," tech. rep., FEB 2008.
3. R. P. Feynman, "There's plenty of room at the bottom," *Journal of Microelectromechanical Systems*, vol. 1, no. 1, 1992.
4. K. E. Peterson, "Silicon as a mechanical material," in *Proceedings of the IEEE*, pp. 420–457, 1982.
5. S. Middelhoek, A. Bellekom, U. Dauderstadt, P. J. French, S. R. Hout, W. Kindt, F. Riedijk, and M. J. Vellekoop, "Silicon sensors," *Meas. Sci. Technol.*, vol. 6, pp. 1641–1658, 1995.
6. J. Fluitman, "Microsystems technology: objectives," *Sensors and Actuators A: Physical*, vol. 56, pp. 151–166, August 1996.
7. K. Suzuki, "Creation of an insect-based microrobot with an external skeleton and elastic joints," in *[1992] Proceedings IEEE Micro Electro Mechanical Systems*, pp. 190–195, 1992.
8. T. Fukuda, "Mechanism and swimming experiment of micro mobile robot in water," *Proceedings of the IEEE Micro Electro Mechanical Systems*, pp. 273–278, 1994.
9. I. U. o. T. Shimoyama, Y. Kubo, T. Kaneda, and H. Miura, "Simple microflight mechanism on silicon wafer," *Proceedings of the IEEE Micro Electro Mechanical Systems, An Investigations of Micro Structures, Sensors, Actuators, Machines and Robotic Systems*, pp. 148–152, 1994.
10. J. M. Grasmeyer and M. T. Keennon, *Development of the Black Widow micro air vehicle*. UNITED STATES, VA: American Institute of Aeronautics and Astronautics, Inc.: Reston, 2001.
11. J. G. M. and M. T. Keennon, "Development of the black widow micro air vehicle," vol. AIAA Paper 2001-0127, AIAA, Aerospace Sciences Meeting and Exhibit, 39th, Reno, NV; UNITED STATES; 8-11 Jan. 2001. 2001.
12. P. G. Ifju, D. A. Jenkins, S. Ettinger, Y. Lian, and W. Shyy, "Flexible wing based micro air vehicles," in *40th AIAA Aerospace Sciences Meeting and Exhibit*, 2002.
13. W. Shyy, "Membrane wing-based micro air vehicles," *Applied Mechanics Reviews*, vol. 58, no. 1, pp. 283–301, 2005.

14. R. Wood, "An autonomous palm-sized gliding micro air vehicle," *IEEE robotics and automation magazine*, vol. 14, no. 2, pp. 82–91, 2007.
15. K. D. Jones and M. F. Platzer, "Bio-inspired design of flapping wing micro air vehicles - an engineer's perspective," in *44th AIAA Aerospace Sciences Meeting 2006*, vol. 1, pp. 463–476, American Institute of Aeronautics and Astronautics Inc., Reston, VA 20191-4344, United States, Jan 9-12 2006 2006.
16. P. Muren, "<http://www.proxflyer.com>."
17. I. Kroo and F. B. Prinz, "The mesicopter: A meso-scale flight vehicle," 31 May 1999 1999.
18. N. Miki and I. Shimoyama, "Soft-magnetic rotational microwings in an alternating magnetic field applicable to microflight mechanisms," *Journal of Microelectromechanical Systems*, vol. 12, no. 2, pp. 221–227, 2003.
19. N. Miki, "Dynamics of a microflight mechanism with magnetic rotational wings in an alternating magnetic field," 2002.
20. U. o. T. Miki, N. (Mechano-Informatics and I. Shimoyama, "An attitude control of a micro-flight mechanism with rotational wings," *Proceedings of the IEEE Micro Electro Mechanical Systems (MEMS)*, pp. 602–605, 2001.
21. N. U. o. T. Miki and I. Shimoyama, "Micro-flight mechanism with rotational wings," *Proceedings of the IEEE Micro Electro Mechanical Systems (MEMS)*, pp. 158–163, 2000.
22. N. Miki, "Magnetic rotational micro-wings applicable to microrobots," 1999.
23. N. U. o. T. Miki and I. Shimoyama, "Analysis of the flight performance of small magnetic rotating wings for use in microrobots," *Proceedings - IEEE International Conference on Robotics and Automation*, vol. 4, pp. 3065–3070, 1998.
24. N. E. Glauvitz, "Toward a flying mems robot," *Technical Reports*, p. 152, 2007.
25. K. Chabak, "Feasability study on mems flying robots," 2008.
26. R. C. Michelson, "Novel approaches to miniature flight platforms," *Proceedings of the Institution of Mechanical Engineers – Part G – Journal of Aerospace Engineering*, vol. 218, no. 6, p. 363(11), 2004.
27. R. C. Michelson and M. A. Naqvi, "Extraterrestrial flight (entomopter-based mars surveyor)," Nov 24-28, 2003 2003.
28. R. C. M. Reece, "Update on flapping wing micro air vehicle research-ongoing work to develop a flapping wing, crawling "entomopter"," *RPVs Thirteenth International Conference.RPVs/UAVs.Remotely Piloted Vehicles*, pp. 30/1–11, 1998.
29. N. Pornsin-sirirak, Y. C. Tai, H. Nassef, and C. M. Ho, "Titanium-alloy mems wing technology for a micro aerial vehicle application," *Sensors and Actuators, A: Physical*, vol. 89, no. 1-2, pp. 95–103, 2001.

30. N. Pornsin-sirirak, S. W. Lee, H. Nassef, J. Grasmeyer, Y. C. Tai, C. M. Ho, and M. Keennon, "Mems wing technology for a battery-powered ornithopter," *Proceedings of the IEEE Micro Electro Mechanical Systems (MEMS)*, pp. 799–804, 2000.
31. R. Wood, "Fly, robot fly," *IEEE Spectrum*, vol. 45, pp. 25–29, 03 2008.
32. R. J. Wood, S. Avadhanula, M. Menon, and R. S. Fearing, "Microrobotics using composite materials: The micromechanical flying insect thorax," in *2003 IEEE International Conference on Robotics and Automation*, vol. 2, (Taipei, Taiwan), pp. 1842–1849, Department of EECS, University of California, Berkeley, CA 94720, United States, Institute of Electrical and Electronics Engineers Inc, Sep 14-19 2003 2003.
33. T. Mueller, "Biomimetics," 2008.
34. H.-Y. Chan, "A biomimetic flying silicon microchip: Feasibility study," *Proceedings - 2004 IEEE International Conference on Robotics and Biomimetics, IEEE ROBIO 2004*, pp. 447–451, 2004.
35. D. J. Denninghoff, "Power-scavenging mems robots," 2006.
36. M. Dickinson, "Insect flight," *Current Biology*, vol. 16, pp. R309–R314, 05 2006.
37. A. L. R. Thomas, G. K. Taylor, R. B. Srygley, R. L. Nudds, and R. J. Bomphrey, "Dragonfly flight: free-flight and tethered flow visualizations reveal a diverse array of unsteady lift-generating mechanisms, controlled primarily via angle of attack," *Journal of Experimental Biology*, vol. 207, no. 24, p. 4299(25), 2004.
38. S. P. Sane and M. H. Dickinson, "The aerodynamic effects of wing rotation and a revised quasi-steady model of flapping flight," *Journal of Experimental Biology*, vol. 205, p. 1087(10), 15 2002.
39. S. N. Fry, R. Sayaman, and M. H. Dickinson, "The aerodynamics of hovering flight in drosophila," *Journal of Experimental Biology*, vol. 208, no. 12, p. 2303(16), 2005.
40. M. H. Dickinson, F.-O. Lehmann, and S. P. Sane, "Wing rotation and the aerodynamic basis of insect flight," *Science*, vol. 284, p. 1954(7), 06/18/99.
41. S. A. Combes and T. L. Daniel, "Into thin air: contributions of aerodynamic and inertial-elastic forces to wing bending in the hawkmoth *manduca sexta*," *Journal of Experimental Biology*, vol. 206, pp. 2999–3006, September 1 2003.
42. T. L. Daniel and S. A. Combes, "Flexible wings and fins: Bending by inertial or fluid-dynamic forces?," *Integrative and Comparative Biology*, vol. 42, no. 5, pp. 1044–5, 2002.
43. S. P. Sane, "The aerodynamics of insect flight," *Journal of Experimental Biology*, vol. 206, no. 23, p. 4191(18), 2003.



44. S. A. Jacobson and A. H. Epstein, "An informal survey of power mems," *The International Symposium on Micro-Mechanical Engineering*, 2003.
45. J. H. Joo and G. M. Choi, "Simple fabrication of micro-solid oxide fuel cell supported on metal substrate," *Journal of Power Sources*, vol. 182, pp. 589–593, 8/1 2008.
46. "History of the solar cell," 2008 Jan 11 2008.
47. D. Macaulay, *Electricity and Automation*, pp. 270–357. The Way Things Work, Boston: Houghton Mifflin Company, 1988.
48. T. L. Fifer, "Radiation effects on multi-junction solar cells," *Technical Reports*, p. 90, 2001.
49. A. F. Hepp, "Multi-junction thin-film solar cells on flexible substrates for space power [microform] /," 2002.
50. R. D. McConnell and M. Symko-Davies, "Multijunction photovoltaic technologies for high performance concentrators (presentation)," 2006 May 01.
51. S. M. Sze and K. K. Ng, *Physics of Semiconductor Devices*. New Jersey: Wiley, 2007.
52. H. J. Moller, *Semiconductors for Solar Cells*. Boston: Artech House, 1993.
53. A. L. Fahrenbruch and R. H. Bube, *Fundamentals of Solar Cells*. New York: Academic Press, 1983.
54. C. Hu and R. M. White, *Solar Cells From Basics to Advanced Systems*. New York: McGraw-Hill Book Company, 1983.
55. C. Waldauf, M. C. Scharber, P. Schilinsky, J. A. Hauch, and C. J. Brabec, "Physics of organic bulk heterojunction devices for photovoltaic applications," *Journal of Applied Physics*, vol. 99, no. 10, p. 104503, 2006.
56. S. Hollar, A. Flynn, C. Bellew, and K. Pister, "Solar powered 10 mg silicon robot," *Micro Electro Mechanical Systems, 2003. MEMS-03 Kyoto. IEEE The Sixteenth Annual International Conference*, pp. 706–711, Jan. 2003.
57. D. Macaulay, *The Way Things Work*. Boston: Houghton Mifflin Company, 1988.
58. W. Shyy, Y. Lian, J. Tang, D. Viieru, and H. Liu, *Aerodynamics of Low Reynolds Number Flyers*. 32 Avenue of the Americas, New York, NY 10013-2473: Cambridge University Press, 2008.
59. S. A. Combes and T. L. Daniel, "Shape, flapping and flexion: Wing and fin design for forward flight," *Journal of Experimental Biology*, vol. 204, p. 2073(13), 15 2001.
60. D. J. Bell, T. J. Lu, N. A. Fleck, and S. M. Spearing, "Mems actuators and sensors: observations on their performance and selection for purpose," *Journal of Micromechanics and Microengineering*, vol. 15, no. 7, pp. S153–S164, 2005.

61. R. Platteborze, “Mems safe-and-arm barrier for low-energy exploding foil initiators,” 2008.
62. D. Koester, A. Cowen, R. Mahadevan, M. Stonefield, and B. Hardy, *PolyMUMPs Design Handbook*. MEMSCAP, 10 ed., 2003.
63. L. Wu and H. Xie, “A large vertical displacement electrothermal bimorph microactuator with very small lateral shift,” *Sensors and Actuators A: Physical*, vol. 145-146, pp. 371–379, 0 2008.
64. Coventor, Inc, *CoventorWare<sup>®</sup> Manual*, rev a ed., March 2008.

REPORT DOCUMENTATION PAGE					Form Approved OMB No. 0704-0188	
<p>The public reporting burden for this collection of information is estimated to average 1 hour per response, including the time for reviewing instructions, searching existing data sources, gathering and maintaining the data needed, and completing and reviewing the collection of information. Send comments regarding this burden estimate or any other aspect of this collection of information, including suggestions for reducing this burden to Department of Defense, Washington Headquarters Services, Directorate for Information Operations and Reports (0704-0188), 1215 Jefferson Davis Highway, Suite 1204, Arlington, VA 22202-4302. Respondents should be aware that notwithstanding any other provision of law, no person shall be subject to any penalty for failing to comply with a collection of information if it does not display a currently valid OMB control number. PLEASE DO NOT RETURN YOUR FORM TO THE ABOVE ADDRESS.</p>						
1. REPORT DATE (DD-MM-YYYY)		2. REPORT TYPE		3. DATES COVERED (From — To)		
21-03-2009		Master's Thesis		Sept 2008 — Mar 2009		
4. TITLE AND SUBTITLE  Micro-Scale Flapping Wings for the Advancement of Flying MEMS				5a. CONTRACT NUMBER		
				DACA99-99-C-9999		
				5b. GRANT NUMBER		
				5c. PROGRAM ELEMENT NUMBER		
6. AUTHOR(S)  Nicholas R. Coleman, Capt, USAF				5d. PROJECT NUMBER		
				07-141		
				5e. TASK NUMBER		
				5f. WORK UNIT NUMBER		
7. PERFORMING ORGANIZATION NAME(S) AND ADDRESS(ES)				8. PERFORMING ORGANIZATION REPORT NUMBER		
Air Force Institute of Technology Graduate School of Engineering and Management (AFIT/EN) 2950 Hobson Way WPAFB OH 45433-7765				AFIT/GE/ENG/09-09		
9. SPONSORING / MONITORING AGENCY NAME(S) AND ADDRESS(ES)				10. SPONSOR/MONITOR'S ACRONYM(S)		
Air Force Research Laboratory (Roger Smith) 101 W. Eglin Blvd, Bldg 13 Eglin Air Force Base, FL 32542 (850-882-4651, roger.smith2@eglin.af.mil)				AFRL/RWAV		
				11. SPONSOR/MONITOR'S REPORT NUMBER(S)		
12. DISTRIBUTION / AVAILABILITY STATEMENT						
Approval for public release; distribution is unlimited.						
13. SUPPLEMENTARY NOTES						
14. ABSTRACT This research presents conceptual micro air vehicles (MAV) with total dimensions less than one millimeter. The effort sought to advance understanding of MAV at sub-millimeter dimensions by fabricating and testing micro scale flapping wings. The biomimetic wings derived from three different insects; the dragonfly, house fly, and butterfly, were selected based off of their natural attributes. The fabricated wings utilize a thermal bimorph structure consisting of polysilicon and gold which allows device actuation through joule heating. The released micro wing initially deflections upward due to residual stress between the gold and polysilicon material layers. Joule heating, from an applied bias, forces the wing to deflect toward the substrate due to the coefficient of thermal expansion mismatch between the material layers. Each fabricated bio-wing structure was tested for deflection range as well as operating frequency. From the experimental testing of the micro scale flapping bio-wings, aerodynamic values were calculated to include; aspect ratio, reduced frequency in a hover, Reynolds number of a hovering device, drag force, and gravitational force. The research verified insect based wings on the micro scale are capable of producing the desired flapping motion.						
15. SUBJECT TERMS						
MEMS, biomimetics, micro aerial vehicle, MAV, residual stress						
16. SECURITY CLASSIFICATION OF:			17. LIMITATION OF ABSTRACT	18. NUMBER OF PAGES	19a. NAME OF RESPONSIBLE PERSON	
a. REPORT	b. ABSTRACT	c. THIS PAGE			LaVern A. Starman	
U	U	U	UU	139	19b. TELEPHONE NUMBER (include area code)	
					(937) 255-3636, x4618; lavern.starman@afit.edu	